# RATIONAL FUNCTION INTERPOLATION OF ELECTROMAGNETIC TRANSFER FUNCTIONS OF HIGH-SPEED INTERCONNECT SYSTEMS FROM DISCRETE TIME-DOMAIN AND FREQUENCY-DOMAIN DATA

BY

SE-JUNG MOON

B.S., Seoul National University, 1999
M.S., Seoul National University, 2001

DISSERTATION

Submitted in partial fulfillment of the requirements
for the degree of Doctor of Philosophy in Electrical and Computer Engineering
in the Graduate College of the
University of Illinois at Urbana-Champaign, 2009

Urbana, Illinois

Doctoral Committee:

Professor Andreas C. Cangellaris, Chair
Professor Jianming Jin
Professor José E. Schutt-Ainé
Professor Steven J. Franke

# ABSTRACT

We present new methodologies to generate rational function approximations of broadband electromagnetic responses of linear and passive networks of high-speed interconnects, and to construct SPICE-compatible, equivalent circuit representations of the generated rational functions. These new methodologies are driven by the desire to improve the computational efficiency of the rational function fitting process, and to ensure enhanced accuracy of the generated rational function interpolation and its equivalent circuit representation.

Toward this goal, we propose two new methodologies for rational function approximation of high-speed interconnect network responses. The first one relies on the use of both time-domain and frequency-domain data, obtained either through measurement or numerical simulation, to generate a rational function representation that extrapolates the input, early-time transient response data to late-time response while at the same time providing a means to both interpolate and extrapolate the used frequency-domain data.

The aforementioned hybrid methodology can be considered as a generalization of the frequency-domain rational function fitting utilizing frequency-domain response data only, and the time-domain rational function fitting utilizing transient response data only. In this context, a guideline is proposed for estimating the order of the rational function approximation from transient data. The availability of such an estimate expedites the time-domain rational function fitting process.

The second approach relies on the extraction of the delay associated with causal electromagnetic responses of interconnect systems to provide for a more stable rational function process utilizing a lower-order rational function interpolation. A distinctive feature of the proposed methodology is its utilization of scattering parameters.

For both methodologies, the approach of fitting the electromagnetic network matrix one element at a time is applied. It is shown that, with regard to the computational cost of the rational function fitting process, such an element-by-element rational function fitting is more advantageous than full matrix fitting for systems with a large number of ports. Despite the disadvantage that different sets of poles are used in the rational function of different elements in the network matrix, such an approach provides for improved accuracy in the fitting of network matrices of systems characterized by both strongly coupled and weakly coupled ports.

Finally, in order to provide a means for enforcing passivity in the adopted element-by-element rational function fitting approach, the methodology for passivity enforcement via quadratic programming is modified appropriately for this purpose and demonstrated in the context of element-by-element rational function fitting of the admittance matrix of an electromagnetic multiport.

To Hee Jeoung, Seungche, and my father in Korea

# ACKNOWLEDGMENTS

First of all, I would like to thank my adviser, Professor Andreas C. Cangellaris, for his guidance and support throughout the years. It is my great honor and also a big blessing for me to be his student. Not only have I admired his intelligence and wisdom, but also his perseverance, modesty, and warmth as a person. Also I deeply appreciate the instruction from my Ph.D. committee members: Professors Jianming Jin, José E. Schutt-Ainé, and Steven J. Franke. This dissertation has benefited greatly from the committee's advice. I also wish to thank Professor Kevin Kim for giving me the opportunity to come to the University of Illinois.

I acknowledge all the friends and staff members at the University of Illinois for their friendship and support. Especially, I would like to thank Jeayong Ihm, Joon Chung, Myoung Joon Choi, Hong Wu, In Jea Chung, George Manetas, Roula Kollia, Rui Wang, Korean ECE members, Janet Lea Peters, Sherry Lynn Beck, Laurie Fisher, and James Andrew Hutchinson. I will miss you a lot.

Special thanks go to the members of the Korean Church of Champaign-Urbana for their support and friendship. Through this great communion I have renewed my way of living and the ways to love. This is the domain of blessing where, among others, I met my husband, and gave birth to our child. Many challenges that I faced through the pursuit of the Ph.D. degree, both as a mother and as a student, were more dear because of the resources of love and grace that I have enjoyed from Reverend Jong Heon Ham and his wife, Myung Sook Jin; Eun Hyun Kim and the sisters of the Esther's Quiet Time Keepers; the family of Hye Kyung Lee; Ms. Su Bin Choi; the Communion of

Isaiah; the family of Lae-Hoon Kim; Jae Hyung Han; Eun Young Jung; the teachers of the Sunday school; the church choir; and the numerous wonderful people that I have met through the years.

Finally, I would like to thank the most wonderful person in my heart, my beloved husband Hee Jeoung Yu, for his love, understanding and everything else. I thank my parents and brothers whom I left in Korea for their love, their celebration of life, and support. Thank you Dad, Mom, and Yoo Shin. You are always in my mind.

# TABLE OF CONTENTS


CHAPTER 1 INTRODUCTION ..... 1
1.1 High-Speed Interconnect Modeling ..... 1
1.2 Research Objectives ..... 5
1.3 Thesis Organization ..... 7

CHAPTER 2 BACKGROUND ..... 9
2.1 Physical Requirements of Linear, Time-Invariant, Passive Networks ..... 10
2.1.1 Realness ..... 12
2.1.2 Causality ..... 12
2.1.3 Stability ..... 14
2.1.4 Passivity ..... 15
2.2 Vector Fitting ..... 17
2.3 Time-Domain Vector Fitting of Network Transfer Functions ..... 20
2.3.1 Data preparation ..... 22
2.4 Element-by-Element Matrix Rational Function Approximation ..... 23
2.4.1 Comparison between the VF and the element-by-element VF ..... 25
2.5 State Equation Representation of Synthesized Linear Networks ..... 30

CHAPTER 3 ORDER ESTIMATION OF RATIONAL FUNCTION APPROXIMATION OF NETWORK TRANSFER FUNCTION ..... 34
3.1 *WT* Rule, Order Estimation for TDVF ..... 35
3.2 Validation Studies ..... 38
3.2.1 A four-port interconnect system ..... 39
3.2.2 A SISO interconnect system ..... 45
3.3 Summary ..... 48

CHAPTER 4 COMBINED RATIONAL APPROXIMATION FROM FREQUENCY-DOMAIN AND TIME-DOMAIN DATA (CRAFT)…… ..... 49
4.1 Formulation of CRAFT ..... 51
4.2 Comparison with Sarkar's Hybrid Extrapolation Methods ..... 52
4.3 The Modified CRAFT ..... 54
4.4 Data Preparation ..... 55
4.5 Validation Studies ..... 56
4.5.1 A four-port interconnect system ..... 56
4.5.2 A terminated coaxial cable ..... 66
4.6 Summary ..... 67

CHAPTER 5 DELAYED RATIONAL FUNCTION APPROXIMATION…… ..... 70
5.1 Causality and Delay Extraction ..... 72
5.2 Rational Function Approximation with Delay Extraction ..... 73

5.3 Rational Function Order Reduction Due to Delay Extraction ..... 74
5.4 Computation of Transport Delay and Optimized Delayed Rational Fit ..... 77
5.5 Limitation of Delayed Rational Function Approximation ..... 83
5.6 Validation Studies ..... 88
5.6.1 Coupled transmission lines ..... 88
5.6.2 Lossy transmission line ..... 94
5.7 Summary ..... 94

CHAPTER 6 PASSIVITY ENFORCEMENT METHODS ..... 97
6.1 Background ..... 98
6.2 Passivity Enforcement via Quadratic Programming for Element-by-Element Rational Function Approximations ..... 101
6.3 Validation Study ..... 104
6.4 Summary ..... 106

CHAPTER 7 SPICE-COMPATIBLE EQUIVALENT CIRCUIT SYNTHESIS ..... 107
7.1 Recursive Convolution ..... 107
7.2 Equivalent Circuit Synthesis of Rational Function Fit of Y Parameter ..... 109
7.2.1 Lumped circuit realization ..... 109
7.2.2 LAPLACE element realization ..... 115
7.3 Equivalent Circuit Synthesis of Delayed Rational Function Fit of S Parameter ..... 116
7.3.1 Circuit synthesis ..... 117
7.3.1.1 Synthesis of directional coupler ..... 119
7.3.1.2 Synthesis of the load ..... 120
7.4 Validation Studies ..... 124
7.4.1 Four-conductor stripline ..... 124
7.4.2 Coupled transmission lines ..... 127
7.5 Summary ..... 132

CHAPTER 8 SUMMARY AND FUTURE WORK ..... 133
8.1 Summary ..... 133
8.2 Future Work ..... 135

REFERENCES ..... 137

APPENDIX A INVERSE FAST FOURIER TRANSFORM ..... 143

AUTHOR'S BIOGRAPHY ..... 145

# CHAPTER 1
# INTRODUCTION

## 1.1 High-Speed Interconnect Modeling

The term "high speed" or "high frequency" is used to describe electronic systems in which clock frequencies exceed 100 MHz or signal switching times are less than about 1 ns. As the effective frequency bandwidth of operation of very large-scale integration (VLSI) extends to the microwave (high-frequency) realm, as switching times dip down to a few tens of picoseconds, and as interconnect packaging density increases, the wire interconnects at both the chip and the package level are no longer "electrically transparent" to signals. When signals go through interconnects, their integrity is affected by distributed electromagnetic (EM) effects such as attenuation, reflection, interference, radiation, and delay. Consequently, accurate modeling methods and efficient simulation techniques are needed to predict the distortion of signals in order to enable noise-aware design of interconnects in the high-speed regime.

Modeling refers to an electrical representation that a simulator can interpret and use to predict voltage and current waveforms; hence, the development of modeling is closely tied to that of the simulator. There are two types of electrical simulators: EM simulators, which solve Maxwell's equations and evaluate the electric and magnetic fields at any location in the time or frequency domain, and circuit simulators, which solve for voltage and currents governed by Kirchhoff's circuit laws. In the serial procedure of modeling and simulation of high-speed interconnects, two major issues

are involved [1]. One is that, while the linear electromagnetic behavior of interconnects can be represented in terms of frequency-domain models, nonlinear devices of the driver and receiver electronics can only be described in the time domain. Hence, numerical analysis of the overall interconnect network requires solving the mixed frequency/time problem, which a traditional circuit simulator like SPICE (Simulation Program with Integrated Circuit Emphasis) cannot handle efficiently. The other issue is the high CPU (central processing unit) cost associated with the simulation of large interconnect networks for the time-domain analysis. Modeling methods and simulation techniques for such networks have been driven by the desire to overcome these problems, thereby enhancing the computational efficiency and accuracy of computer-aided analysis and design [2].

Circuit simulators governed by Kirchhoff's circuit laws, the approximated form of Maxwell's equations in the absence of electromagnetic retardation, are much faster and less complicated than EM simulators; thus, they are the most extensively used simulators when the wavelengths of operating signals are sufficiently larger than the circuit elements. However, these circuit simulators lack the accuracy needed for predicting the parasitic EM effects associated with signal distortion in high-speed interconnects. Hence, EM simulators solving Maxwell's equations are inevitable for such analysis. Over the past 20 years, significant effort has been devoted to the advancement of methodologies for modeling and simulation of a interconnect system with nonlinear elements with electromagnetic accuracy. Despite significant advances, the current state of the art lacks the robustness, ease of modeling, and computational

efficiency necessary for routine use [3]. For these reasons, hybrid approaches that rely on the representation of the linear interconnect network in terms of models compatible with transient, nonlinear circuit simulators such as SPICE have been advanced and are currently favored for noise-aware CAD.

The methods of incorporating models of linear interconnect structures into circuit simulators can be broadly classified into three approaches. One approach relies on transmission-line modeling of interconnects [4-8]. Another is to interpret the interconnect structure electromagnetic model in terms of a circuit, utilizing an integral equation formalism of Maxwell's equations and solving it using the partial element equivalent circuit (PEEC) method [9-12]. The third approach has been motivated by the need to tackle the complexity associated with the circuit models resulting from using either transmission line or PEEC models for interconnect structures of high complexity. The large dimensions of these models make the SPICE-based nonlinear system numerical solution computationally demanding if not prohibitive. To tackle this complexity, model order reduction (or macromodeling) techniques have been pursued [13-32]. Interconnect macromodels are usually obtained in two ways. One way is through model-order reduction (MOR) [13-21] of the generated model. The second approach relies on utilizing the responses of the interconnect structure under known excitations to deduce from them equivalent circuit representations that reproduce the electromagnetic response of the structure with acceptable accuracy over the bandwidth of interest. We will refer to this class of methods as black-box modeling [22-32].

In this dissertation, we focus on black-box modeling. From now on, we will refer to black-box modeling simply as macromodeling. Macromodeling methods rely on the fact that the interconnect system is passive and linear. Thus, its frequency-dependent EM behavior is completely captured in terms of the frequency-domain response of the multiport device under test (DUT), represented in terms of a network matrix (impedance, admittance, or scattering matrix). A common representation of the frequency dependence of the elements of the network matrices is in terms of rational functions. Rational function approximation methods are most attractive in that they capture the behavior of the system especially around response resonances and provide for their convenient and expedient incorporation into commonly used nonlinear circuit simulators, either in terms of direct synthesis of equivalent circuits or through easily deduced state-space representations. Numerous methodologies have been proposed for the development of such rational function approximations of EM transfer functions. Most of the proposed methods to date utilize either frequency-domain data or time-domain data, obtained through numerical simulation or measurement, as input to the rational function fitting algorithm. From these two classes of methods, we focus on the frequency-domain vector fitting (VF) process [22], [23] and its time-domain counterpart, time-domain vector fitting (TDVF) [24], and propose ways in which they can be advanced or combined to improve their accuracy, efficiency and ease of use. Our research objectives are discussed in more detail next.

## 1.2 Research Objectives

The focus of this dissertation is the advancement of new methodologies for the construction of rational function models of broadband electromagnetic responses of linear networks, and their subsequent description in terms of SPICE-compatible equivalent circuits with the goal of improved accuracy of the generated macromodel and enhanced computational efficiency both in the numerical process of its generation and in its subsequent use in a circuit simulation environment. The first objective toward meeting this goal concerns the rational function approximation, utilizing electromagnetic response data from both time and frequency domains, combining the VF and its time-domain counterpart, TDVF, toward the synthesis of mathematical models for broadband electromagnetic responses. The resulting rational fitting algorithm will be referred to as CRAFT (Combined Rational Approximation from Frequency-Domain and Time-Domain Data) in the following [30-31]. Its development was prompted by the principle that early-time transient response data and low-frequency frequency-domain response data hold most of the necessary information to describe the broadband response of a linear system [32]. Since numerical frequency-domain analysis tends to be most computationally efficient at lower and moderate frequencies (for which the electrical length of the characteristic dimensions of the DUT is roughly of the same order as the wavelength), while time-domain numerical analysis through marching-on-in-time algorithms quickly generates an early-time response of the DUT that is rich in high-frequency content, combining results from

such analyses promises to yield more robust and accurate fitting of the DUT response over a broad frequency bandwidth.

Our second objective concerns the estimation of the order of the rational function needed for the accurate fitting of the DUT response using TDVF. The proper choice of the order for the fit is important both in terms of achieving accuracy and in ensuring robustness of the fitting algorithm. While several techniques are available for predicting the rational function order in the context of frequency-domain vector fitting, the topic has not been explored in the case of TDVF. We address this void in this thesis.

Our third objective concerns the advancement of methods for extracting the transport lag (interconnect-induced delay) prior to generating the rational function approximation of system transfer function response. Transport delay extraction provides significant reduction in the order of the rational function fit and facilitates the task of generating causal and more accurate modeling representations [7, 8, 28, 29]. Our approach relies on the use of scattering parameter transport delay extraction. Scattering parameters, or S parameters, are natural candidates for being fitted as the product of a rational function with a transport delay function $\exp(-Ts)$, where $T$ is the interconnect-induced delay, because they are ratios of transmitted (or reflected) and incident waves at the ports of the DUT, with the ports terminated at properly selected reference impedances. In the following, we will refer to such rational function fits with transport delay as "delayed rational fits."

The fourth objective of our research concerns the passivity enforcement of the generated rational function approximation. This is motivated by the fact that, even though we restrict our attention to rational function fitting of passive systems, the passivity of rational function approximations generated via VF and TDVF cannot be guaranteed in the fitting process unless a passivity enforcement method is used in conjunction with the rational function fitting algorithm. In this work the emphasis is on passivity enforcement algorithms for element-by-element rational function fitting of multiport networks matrices.

The fifth objective concerns the synthesis of SPICE-compatible equivalent circuits to represent the delayed rational fits for the S parameters [33]. Special attention is paid to the development of the synthesis approach in a manner such that the resulting equivalent circuit representation is readily compatible with the port voltage/current variable framework used in SPICE and other, related, general-purpose, nonlinear, transient circuit simulation tools.

## 1.3 Thesis Organization

The thesis is organized as follows. In Chapter 2, we discuss the requirements that a linear, time-invariant macromodel should satisfy, to ensure its stability, causality and passivity. Also we review frequency- and time-domain vector fitting and present a variation where these methods are applied to an element-by-element rational function fitting of the network matrix of a multiport linear system.

The *WT* rule for the estimation of the order of the rational function fit using time-domain data via the TDVF algorithm is presented in Chapter 3. In Chapter 4, the

hybrid, frequency-domain and time-domain data based rational function fitting algorithm CRAFT is described in detail and the *WT* rule of Chapter 3 is reinterpreted for use in the context of CRAFT.

In Chapter 5, the methodology for delayed rational function approximation including a means for delay estimation is presented, and its effectiveness in reducing the order of the rational function fit is examined.

In Chapter 6, we briefly review the various passivity enforcement methods and demonstrate that the passivity enforcement method via quadratic programming can be applied to the element-by-element rational function fit method we have adapted.

In Chapter 7, we review various SPICE-equivalent circuit synthesis methods and then present our approach for the synthesis of SPICE-compatible delayed rational fits for S parameters.

The dissertation concludes with a summary of our contribution and ideas for future work in Chapter 8.

# CHAPTER 2
# BACKGROUND

A macromodel is a mathematical representation of a device under test (DUT), which is obtained by projecting the measured/simulated (tabulated) frequency-domain or time-domain data onto a functional space of suitable basis functions. Such a projection or approximation (interpolation) is called macromodeling. A rational function, which is defined as a quotient of polynomials, is most suitable for capturing the behavior of the system response in the vicinity of the peaks of its resonances, and it has been widely used for macromodeling [13-31].

We are interested in macromodeling methods of systems that are passive, linear and time-invariant; thus, their frequency-dependent responses are completely described in terms of frequency data of the admittance, impedance, and scattering matrix representations. The attributes of the system impose specific requirements for the generated macromodel. These requirements are real coefficients, stability, causality, and passivity [33-38].

It is known that rational function approximation methods have several main difficulties. First, they suffer from the problem of ill-conditioning in capturing the broadband frequency spectrum of the response; second, the rational function approximation cannot ensure the causality of the response, especially for systems with electromagnetic delay due to its using a finite order [28]; and third, passivity of the

resulting macromodel is not guaranteed but needs to be enforced though appropriate constraints during the synthesis process.

As has been demonstrated in the pertinent literature, one of the advantages of the vector fitting (VF) method is that it effectively tackles the ill-conditioning problem [39]. To facilitate the preservation of the causality of the numerically generated macromodel, one may choose to synthesize a function, obtained by extracting the transport delay from the response. With regard to the issue of passivity from a variety of approaches proposed for its enforcement, we adopted the passivity enforcement method via quadratic programming (PEQP) [40]. PEQP has mostly been used for matrix rational function fitting, where enforcement of passivity is applied to the entire system response through its transfer function matrix representation. For our purposes we exploit and demonstrate its usage for the element-by-element rational function fitting of the admittance matrix. This is presented in Chapter 6.

In this chapter, the physical concepts of realness, stability, causality, and passivity are reviewed first. Then we turn our attention to the review and discussion of the specific macromodeling methods of VF and time-domain vector fitting (TDVF).

## 2.1 Physical Requirements of Linear, Time-Invariant, Passive Networks

The system under consideration is a linear, time-invariant, electrical $N_p$ – port network, which can be characterized by an $N_p$ x $N_p$ impulse response matrix $\boldsymbol{h}(t)$. Thus, given an $N_p$ input vector, $\boldsymbol{x}(t)$, the response at port *i* due to the input at port *j* is given by

$$\{\boldsymbol{y}(t)\}_{ij}=\{\boldsymbol{h}(t)\}ij*\boldsymbol{x}_j(t)=\int_{-\infty}^{+\infty}\boldsymbol{h}_{ij}(t-\tau)\boldsymbol{x}_j(\tau)d\tau, \tag{2.1}$$

where $*$ denotes the convolution operator [41], and $i,j$=1,2,...,$N_p$.

In $s$ domain (Laplace domain), the system response can be represented in terms of a rational function approximation as

$$\{\boldsymbol{H}(s)\}_{ij}=\frac{Y_{ij}(s)}{X_j(s)}=\sum_{n=1}^{N_{ij}}\frac{R_{n,ij}}{s-q_n}+d_{ij}+se_{ij}, \tag{2.2}$$

where $\boldsymbol{H}(s)$ represents the matrix transfer function in Laplace domain, and $\{\boldsymbol{H}(s)\}_{ij}$ denotes the ($i$,$j$) element with input at port $j$, $X_j(s)$, and output at port $i$, $Y_{ij}(s)$. $\boldsymbol{H}(s)$ can be either the scattering matrix ($X_j(s)$ being an incident wave, and $Y_{ij}(s)$ being a reflected wave), the admittance matrix ($X_j(s)$ being a port voltage, and $Y_{ij}(s)$ being a port current), or the impedance matrix ($X_j(s)$ being a port current, and $Y_{ij}(s)$ being a port voltage).

The relation between $\boldsymbol{H}(s)$ and $\boldsymbol{h}(t)$ is defined through the (bilateral) Laplace transform as

$$\boldsymbol{H}(s)=\int_{-\infty}^{+\infty}\boldsymbol{h}(t)e^{-st}dt, \tag{2.3}$$

where $s=\sigma+j\omega \in$ ROC (region of convergence) [42]. Fourier transformation is the form of the Laplace transform defined on the imaginary axis in the $s$ domain; hence, the Fourier transformation is defined as

$$\boldsymbol{H}(j\omega)=\boldsymbol{H}(s)\big|_{s=j\omega\in ROC}=\int_{-\infty}^{+\infty}\boldsymbol{h}(t)e^{-j\omega t}dt. \tag{2.4}$$

### 2.1.1 Realness

Since $\boldsymbol{h}(t)$ is the impulse response of a physical system and $\boldsymbol{h}(t)$ is real, some constraints are imposed on the coefficients of the rational function fit of $\boldsymbol{H}(s)$. From the definition of the Fourier transformation, since $h_{ij}(t)$ is real, we obtain

$$\boldsymbol{h}(t)=\bar{\boldsymbol{h}}(t)=\int_{-\infty}^{+\infty}\bar{\boldsymbol{H}}(j\omega)e^{-j\omega t}d\omega=\int_{-\infty}^{+\infty}\bar{\boldsymbol{H}}(-j\omega)e^{j\omega t}d\omega. \tag{2.5}$$

Therefore, $\boldsymbol{H}(j\omega)=\bar{\boldsymbol{H}}(-j\omega)$ where '$\bar{}$' denotes complex conjugation. There are sufficient and necessary conditions for the matrix transfer function representation of (2.3) to satisfy $\boldsymbol{H}(j\omega)=\bar{\boldsymbol{H}}(-j\omega)$: the constant term and the linear term must be real, residues for real poles must be real, and the residues for complex conjugate pair poles need to be a complex conjugate pair. Hence, (2.2) can be rewritten as

$$\{\boldsymbol{H}(s)\}_{ij}=\sum_{r=1}^{N_{r,ij}}\frac{R_{r,ij}}{s-p_{r,ij}}+\sum_{c=1}^{N_{c,ij}}\left(\frac{R_{c,ij}}{s-p_{c,ij}}+\frac{\bar{R}_{c,ij}}{s-\bar{p}_{c,ij}}\right)+d_{ij}+se_{ij}, \tag{2.6}$$

where $p_{r,ij}$, $R_{r,ij}$, $r=1,2,...,N_r$ are real poles and residues, and $p_{c,ij}$, $R_{c,ij}$, $c=1,2,...,N_c$ are complex poles and residues. For the realness of $\boldsymbol{h}(t)$, the enforcement is also carried out in the VF formulation [22].

### 2.1.2 Causality

Causality means that the output value of a system at a specific point in time depends only on current and past values of the inputs. This implies that when $x_1(t)$

and $x_2(t)$ are inputs and $y_1(t)$ and $y_2(t)$ are the respective outputs of the system, if $x_1(t) = x_2(t)$ for $t \le t_0$, then $y_1(t) = y_2(t)$ for $t \le t_0$.

All physical systems are causal. Hence, causality is a necessary property of all models intended to be used in any simulator that has a concept of time. For a linear time-invariant (LTI) system to be causal, $h(t)$ is required to satisfy the constraint:

$$h(t) = 0 \ , \qquad \text{for } t < 0. \tag{2.7}$$

Hence, the impulse response is right-sided and the ROC associated with the system is half-plane open on the right, i.e., $\mathrm{Re}\{s\} > \sigma_0$ for some real value of $\sigma_0$.

When a discrete system is considered, causality of its impulse sequence $h[n]$ implies unique relationships between the real and imaginary parts of the Fourier transform providing real and imaginary part sufficiency of the Fourier transform [37]. Any discrete signal can be decomposed into an even part and an odd part as

$$h(n) = h_e(n) + h_o(n) \tag{2.8}$$

where

$$h_e[n] = \frac{h[n] + h[-n]}{2}, \text{ and } \quad h_o[n] = \frac{h[n] - h[-n]}{2}. \tag{2.9}$$

Because the system is causal, $h[n]=0$, $n<0$, then

$$\begin{aligned} h[n] &= 2h_e[n]u[n] - h_e[0]\delta[n] \\ h[n] &= 2h_o[n]u[n] + h_o[0]\delta[n] \end{aligned} \tag{2.10}$$

where $u[n]$ is a unit step sequence, and $\delta[n]$ is a discrete-time impulse. Equation (2.10) implies $h[n]$ can be recovered from $h_e[n]$ or $h_o[n]$. When the Fourier transform of $h[n]$ exists, which is denoted as

$$H(e^{i\omega}) = H_R(e^{i\omega}) + jH_I(e^{i\omega}) \tag{2.11}$$

and $h[n]$ is real, $H(e^{i\omega})$ is the discrete-time Fourier transform of $h[n]$, and $H_R(e^{i\omega})$ and $H_I(e^{i\omega})$ are respectively the discrete-time Fourier tansform of $h_e[n]$ and $h_o[n]$. Thus for a real stable and causal system, we obtain relationships between the real and imaginary parts of the transfer function as

$$\begin{aligned} H_R(e^{i\omega}) &= h[0] + \frac{1}{2\pi} P\int_{-\pi}^{\pi} H_I(e^{i\omega}) \cot\left(\frac{\omega-\theta}{2}\right) d\theta \\ H_I(e^{i\omega}) &= -\frac{1}{2\pi} P\int_{-\pi}^{\pi} H_R(e^{i\omega}) \cot\left(\frac{\omega-\theta}{2}\right) d\theta, \end{aligned} \tag{2.12}$$

where $P$ denotes the Cauchy principal value. The equations in (2.12) imply that the real and imaginary parts of the transfer function are related by Hilbert transform [37].

### 2.1.3 Stability

Stability implies that the system response stays bounded for all times. The well-known bounded-input bounded-output (BIBO) definition of stability is as follows [42]: A system is stable if the output $\boldsymbol{y}(t)$ is bounded for any bounded input $\boldsymbol{x}(t)$. This BIBO stability implies that LTI systems are stable if and only if $h(t)$ is absolutely integrable, i.e., if

$$\int_{-\infty}^{+\infty} |h(t)| dt < +\infty, \tag{2.13}$$

which gives the condition for the Fourier transform of $h(t)$ to converge and exist in (2.4). It also means that an LTI system is stable if and only if the ROC of $\boldsymbol{H}(s)$ includes the $j\omega$-axis in the $s$-plane.

When an LTI system is causal, its ROC is open toward the right half-plane. Hence, a causal system is stable if and only if all the poles of $\boldsymbol{H}(s)$ lie in the left half-plane in the $s$-plane so that its ROC includes the $j\omega$-axis. In the context of VF, the stability of a macromodel is ensured by flipping any right half-plane poles generated using the process onto the left half-plane [34].

### 2.1.4 Passivity

Passivity implies that the system cannot generate more energy than it absorbs. In this dissertation, our emphasis is on passive systems only. Therefore, generated models must be passive. However, the passivity of rational function approximations generated via VF and TDVF is not guaranteed, and a passivity enforcement method is required as a pre- or postprocess of the macromodeling exercise. Passivity is a very important property because even stable, but nonpassive macromodels are known to produce spurious, nonphysical oscillations in the time-domain analysis even when connected to passive terminations [43].

For these reasons, we need to review the definition of passivity for a circuit or macromodel. Passivity is defined as follows [44]: An $N_p$ -port network is said to be passive if

$$\int_{-\infty}^{t} \boldsymbol{v}^T(\tau)\boldsymbol{i}(\tau)d\tau \geq 0 \tag{2.14}$$

for all $t$ and all the port voltages $\boldsymbol{v}(t)$ and currents $\boldsymbol{i}(t)$, when the superscript $^T$ denotes vector/matrix transposition. For the case of scattering parameters, the passivity definition is

$$\int_{-\infty}^{t} [\boldsymbol{a}^T(\tau)\boldsymbol{a}(\tau) - \boldsymbol{b}^T(\tau)\boldsymbol{b}(\tau)]d\tau \geq 0, \tag{2.15}$$

where $\boldsymbol{a}(t)$ and $\boldsymbol{b}(t)$ are, respectively, the incident and reflected power wave vector at ports. Integrals in (2.14) and (2.15) imply that the net energy absorbed by the system is nonnegative. In view of the above requirements for passivity, the following statements can be made for the system matrix of a passive system.

For the case of admittance or impedance matrix, the system is passive [42] if and only if:

(1) Each element of $\boldsymbol{H}(s)$ is defined and analytic in $\mathrm{Re}(s) > 0$.

(2) $\boldsymbol{H}(\overline{s}) = \overline{\boldsymbol{H}}(s)$.

(3) $\boldsymbol{H}(s)$ is a positive real matrix, and $\boldsymbol{x}^H[\boldsymbol{H}^H(s) + \boldsymbol{H}(s)]\boldsymbol{x} \geq 0$ for all complex values of $s$ with $\mathrm{Re}(s) > 0$ and any arbitrary vector $\boldsymbol{x}$, where the superscript $^H$ denotes the transpose conjugate.

For the case of the scattering parameter matrix, the system is passive [42] if and only if:

(1) Each element of $\boldsymbol{H}(s)$ is analytic in $\mathrm{Re}(s) > 0$.

(2) $\boldsymbol{H}(\overline{s}) = \overline{\boldsymbol{H}}(s)$.

(3) $\boldsymbol{H}(s)$ is a unitary bounded matrix, and $\boldsymbol{x}^H[\boldsymbol{I} - \boldsymbol{H}^H(s)\boldsymbol{H}(s)]\boldsymbol{x} \geq 0$ for all complex values of $s$ with $\mathrm{Re}(s) > 0$ and any arbitrary vector $\boldsymbol{x}$. This is equivalent to the condition that the largest singular value of $\boldsymbol{H}(s)$ is not larger than 1 in the right half-plane.

## 2.2 Vector Fitting

It is assumed that the DUT is a passive $N_p$-port system represented by its matrix transfer function $\boldsymbol{H}(s)$. VF is one of the methods used to project the transfer function onto the rational function space in a manner of a least squares approximation. After projection, the (*i,j*) element of $\boldsymbol{H}_{fit}(s)$ is represented as

$$\{\boldsymbol{H}(s)\}_{ij}=\frac{Y_{ij}(s)}{X_j(s)}\approx\frac{B(s)}{A(s)}=\{\boldsymbol{H}_{fit}(s)\}_{ij}=\sum_{n=0}^{M}b_n s^n \Big/ \sum_{n=0}^{N}a_n s^n=\sum_{n=1}^{N}\frac{r_{n,ij}}{s-q_n}+d_{ij}+se_{ij}, \tag{2.16}$$

where $\{r_{n,ij}\}$ and $\{q_n\}$ denote, respectively, the residues and poles, both of which are complex, in general, while the terms $\{d_{ij}\}$ and $\{e_{ij}\}$ are real constants, $i, j = 1, 2, \ldots, N_p$. It is noted in (2.16) that the same set of poles is shared by all elements of the matrix transfer function. The VF process consists of two steps. The first step is to identify poles using a scalar weight function $\sigma(s)$ as

$$\sigma(s)=1+\sum_{n=1}^{N}\frac{\tilde{r}_n}{s-\tilde{q}_n}=\prod_{n=1}^{N}(s-\tilde{z}_n)\Big/\prod_{n=1}^{N}(s-\tilde{q}_n), \tag{2.17}$$

where $\{\tilde{q}_n\}$ are initial estimates for the poles and $\{\tilde{r}_n\}$ are unknown, but the zeros $\{\tilde{z}_n\}$ of $\sigma(s)$ are enforced to be poles $\{q_n\}$ of $\boldsymbol{H}_{fit}(s)$. Hence, the following approximation holds:

$$\sigma(s)\cdot\{\boldsymbol{H}_{fit}(s)\}_{ij}\approx\sum_{n=1}^{N}\frac{r'_{n,ij}}{s-\tilde{q}_n}+d'_{ij}+se'_{ij}. \tag{2.18}$$

Substituting (2.17) into (2.18) and reorganizing yields

$$\left(\sum_{n=1}^{N}\frac{r'_{n,ij}}{s-\tilde{q}_n}+d'_{ij}+se'_{ij}\right)-\left(\sum_{n=1}^{N}\frac{\tilde{r}_n}{s-\tilde{q}_n}\right)\cdot\{\boldsymbol{H}(s)\}_{ij}=\{\boldsymbol{H}(s)\}_{ij}. \tag{2.19}$$

The term $\{\tilde{q}_n\}$ makes (2.19) linear because of cancellation between zeros of $\sigma(s)$ and poles $\{q_n\}$ of $\boldsymbol{H}_{fit}(s)$. This method is called *pole relocation*, which opens the way to estimate and improve the poles $\{q_n\}$ by replacing the initial poles iteratively with the newly obtained zeros $\{\tilde{z}_n\}$.

First, the elements of $\boldsymbol{H}(s)$ for fitting are staked into a single column and they are represented by $H_k$ $(1\le k\le K)$. Then, the indices of *i* and *j* are replaced by *k* in (2.19). Equation (2.19) constitutes a linear equation for $M_f$ samples of $H_k(s)$ in compact form as

$$\boldsymbol{A}_f\cdot\boldsymbol{u}=\boldsymbol{b}_f, \tag{2.20}$$

where

$$\boldsymbol{A}_f=\begin{bmatrix}\boldsymbol{\Omega}_f & & & \boldsymbol{\Omega}_{f,1}\\ & \boldsymbol{\Omega}_f & & \boldsymbol{\Omega}_{f,2}\\ & & \ddots & \vdots\\ & & \boldsymbol{\Omega}_f & \boldsymbol{\Omega}_{f,K}\end{bmatrix},$$

$$\boldsymbol{\Omega}_f=\begin{bmatrix}\frac{1}{s_1-\tilde{q}_1} & \cdots & \frac{1}{s_1-\tilde{q}_N} & 1 & s_1\\ \vdots & \ddots & \vdots & \vdots & \vdots\\ \frac{1}{s_{M_f}-\tilde{q}_1} & \cdots & \frac{1}{s_{M_f}-\tilde{q}_N} & 1 & s_{M_f}\end{bmatrix},\quad \boldsymbol{\Omega}_{f,k}=\begin{bmatrix}\frac{-H_k(s_1)}{s_1-\tilde{q}_1} & \cdots & \frac{-H_k(s_1)}{s_1-\tilde{q}_N}\\ \vdots & \ddots & \vdots\\ \frac{-H_k(s_{M_f})}{s_{M_f}-\tilde{q}_1} & \cdots & \frac{-H_k(s_{M_f})}{s_{M_f}-\tilde{q}_N}\end{bmatrix},$$

$$\boldsymbol{u}=[\boldsymbol{u}_1{}^T\cdots\boldsymbol{u}_K{}^T\,\tilde{\boldsymbol{u}}^T]^T, \tag{2.21}$$

$$\boldsymbol{u}_k=\begin{bmatrix}r_{1,k}\cdots r_{N,k}\ d_k\ e_k\end{bmatrix}^T,\quad \tilde{\boldsymbol{u}}=\begin{bmatrix}\tilde{r}_1\cdots\tilde{r}_N\end{bmatrix}^T,$$

$$\boldsymbol{b}_f=[\boldsymbol{b}_{f,1}{}^T\cdots\boldsymbol{b}_{f,K}{}^T]^T,\quad \boldsymbol{b}_{f,k}=\begin{bmatrix}H_k(s_1)\cdots H_k(s_{M_f})\end{bmatrix}^T,\quad k=1,2,\ldots,K.$$

Equation (2.21) is formulated without consideration for the realness of the fit. The residues of a complex pole pair must also be a conjugate pair. Because only positive frequencies are used in the fitting process, the linear problem representation of the least squares problem was formulated to be real to preserve the conjugacy property [22]. Therefore, when (2.21) is modified as [22] considering the realness of the fit and the values in the least squares problem, the modification doubles the number columns when the number of complex poles is dominant [22].

Solving the least squares problem of (2.20), the coefficients of $\sigma(s)$ and $\sigma(s)\cdot\{\boldsymbol{H}_{fit}(s)\}_{ij}$ are obtained, and the zeros of $\sigma(s)$ are calculated from $\boldsymbol{u}$. From the equations of $\sigma(s)$ and $\sigma(s)\cdot\{\boldsymbol{H}_{fit}(s)\}_{ij}$, we obtain

$$\{\boldsymbol{H}_{fit}(s)\}_{ij}=\frac{(\sigma(s)\cdot H_{fit})_{ij}(s)}{\sigma(s)}=\frac{e'_{ij}\prod_{n=1}^{N+1}(s-z_{n,ij})/\prod_{n=1}^{N}(s-\tilde{q}_n)}{\prod_{n=1}^{N}(s-\tilde{z}_n)/\prod_{n=1}^{N}(s-\tilde{q}_n)}=e'_{ij}\frac{\prod_{n=1}^{N+1}(s-z_{n,ij})}{\prod_{n=1}^{N}(s-\tilde{z}_n)}. \quad (2.22)$$

As mentioned before, Equation (2.22) shows that poles of $\boldsymbol{H}_{fit}(s)$ are equal to the zeros of $\sigma(s)$, which are calculated as the eigenvalues of the matrix

$$\boldsymbol{K}=\boldsymbol{A}-\boldsymbol{b}\cdot\tilde{\boldsymbol{u}}^{T}, \quad (2.23)$$

where $\boldsymbol{A}$ is a diagonal matrix containing the starting poles, $\boldsymbol{b}$ is a column vector of ones and $\tilde{\boldsymbol{u}}^{T}$ is a row-vector containing the residues for $\sigma(s)$.

The second step is the calculation of the residues of $\boldsymbol{H}_{fit}(s)$. In principle, $\boldsymbol{H}_{fit}(s)$ can be directly obtained from (2.22); instead, (2.16) is solved with the obtained zeros

of $\sigma(s)$, which again constitutes a least squares problem to improve accuracy, and the residues of $\boldsymbol{H}_{fit}(s)$ are computed. An iterative process is used to enhance accuracy, and $\boldsymbol{H}_{fit}(s)$ converges to an optimized rational function fit.

## 2.3 Time-Domain Vector Fitting of Network Transfer Functions

The TDVF is a time-domain formulation of the VF. In time domain, (2.16) can be expressed as

$$y_{ij}(t)=L^{-1}[H_{ij}(s)]*x_j(t), \tag{2.24}$$

where $L^{-1}$ is the inverse Laplace transform operator and $*$ the convolution operator. Multiplication of (2.19) on the right by the Laplace transform of the input $X_j(s)$ followed by an inverse Laplace transform yields

$$y_{ij}(t) \approx \sum_{n=1}^{N} r'_{n,ij} \cdot x_{n,j}(t) + d'_{ij} \cdot x_j(t) - \sum_{n=1}^{N} \tilde{r}_n \cdot y_{n,ij}(t), \tag{2.25}$$

where, with $Y_{ij}(s)$ denoting the output quantity resulting from the operation of the right-hand side of (2.19) on $X_j(s)$, the following time-dependent quantities have been introduced:

$$x_{n,j}(t) = L^{-1}\left\{\frac{X_j(s)}{s-\tilde{q}_n}\right\} = \int_0^t e^{\tilde{q}_n(t-\tau)} x(\tau) d\tau \tag{2.26}$$

$$y_{n,ij}(t) = L^{-1}\left\{\frac{Y_{ij}(s)}{s-\tilde{q}_n}\right\} = \int_0^t e^{\tilde{q}_n(t-\tau)} y_{ij}(\tau) d\tau\,. \tag{2.27}$$

Because $x_j(t)$ and $y_{ij}(t)$ are not continuous but sampled with a time step $\Delta t$, a linear interpolation method is utilized to calculate the convolution integrals of (2.26) and (2.27), and this convolution method is called *recursive convolution* [45]. This leads to the following equations:

$$x_{n,j}(t_{m+1}) = \mu_n x_{n,j}(t_m) + \nu_{n,1} x_j(t_{m+1}) + \nu_{n,2} x_j(t_m) \tag{2.28}$$

$$y_{n,ij}(t_{m+1}) = \mu_n y_{n,ij}(t_m) + \nu_{n,1} y_{ij}(t_{m+1}) + \nu_{n,2} y_{ij}(t_m) \tag{2.29}$$

where

$$\begin{aligned} &\mu_n = e^{\tilde{q}_n \Delta t}, \quad \nu_{n,1} = \frac{-1 - \tilde{q}_n \Delta t + e^{\tilde{q}_n \Delta t}}{\tilde{q}_n^2 \Delta t} \ , \quad \text{and} \\ &\nu_{n,2} = \frac{1 + (\tilde{q}_n \Delta t - 1) e^{\tilde{q}_n \Delta t}}{\tilde{q}_n^2 \Delta t} \ . \end{aligned} \tag{2.30}$$

Hence, in matrix form we write

$$\boldsymbol{A}_t \cdot \boldsymbol{u} = \boldsymbol{b}_t \,, \tag{2.31}$$

$$\begin{aligned} &\boldsymbol{A}_t = \begin{bmatrix} \boldsymbol{\Omega}_t & & & \boldsymbol{\Omega}_{t,1} \\ & \boldsymbol{\Omega}_t & & \boldsymbol{\Omega}_{t,2} \\ & & \ddots & \vdots \\ & & \boldsymbol{\Omega}_t & \boldsymbol{\Omega}_{t,K} \end{bmatrix}, \\ &\boldsymbol{\Omega}_t = \begin{bmatrix} \boldsymbol{x}_1(t_1) & \cdots & \boldsymbol{x}_N(t_1) & 1 & 0 \\ \vdots & \ddots & \vdots & \vdots & \vdots \\ \boldsymbol{x}_1(t_{M_t}) & \cdots & \boldsymbol{x}_N(t_{M_t}) & 1 & 0 \end{bmatrix}, \quad \boldsymbol{\Omega}_{t,k} = \begin{bmatrix} -\boldsymbol{y}_{1,k}(t_1) & \cdots & -\boldsymbol{y}_{N,k}(t_1) \\ \vdots & \ddots & \vdots \\ -\boldsymbol{y}_{N,k}(t_{M_t}) & \cdots & -\boldsymbol{y}_{N,k}(t_{M_t}) \end{bmatrix}, \\ &\boldsymbol{u} = [\boldsymbol{u}_1{}^T \ \cdots \ \boldsymbol{u}_K{}^T \ \tilde{\boldsymbol{u}}^T]^T, \\ &\boldsymbol{u}_k = \begin{bmatrix} r'_{1,k} \ \cdots \ r'_{N,k} \ d'_k \ e'_k \end{bmatrix}^T, \quad \tilde{\boldsymbol{u}} = \begin{bmatrix} \tilde{r}_1 \ \cdots \ \tilde{r}_N \end{bmatrix}^T, \\ &\boldsymbol{b}_f = [\boldsymbol{b}_{t,1}{}^T \ \cdots \ \boldsymbol{b}_{t,K}{}^T]^T, \quad \boldsymbol{b}_{t,k} = \begin{bmatrix} \boldsymbol{y}_k(t_1) \ \cdots \ \boldsymbol{y}_k(t_{M_t}) \end{bmatrix}^T, \quad k = 1, 2, \ldots, K, \end{aligned} \tag{2.32}$$

where the port responses, $y_{ij}(t)$ $(1 \le i,\ j \le N_p)$, are staked into a single column to be represented by $y_k(t)$ $(1 \le k \le K)$ as we did for the formulation of VF. When only the upper triangular part of $\boldsymbol{H}(s)$ is considered, $K = N_p(N_p+1)/2$. For the generated rational fit to satisfy the realness in Section 2.1.1 and for the values in the linear problem of (2.32) to be real, (2.32) is modified as in the case of VF [22]. The modification almost doubles the number columns in the matrix statement of the problem when the number of complex poles is dominant.

From (2.31), the poles of the transfer function can be obtained. As in the case of VF, the residues are computed after the poles have been obtained. Also, through an iterative process of the algorithm, the values of the poles and residues are refined.

### 2.3.1 Data preparation

The TDVF constructs $\boldsymbol{H}_{fit}(s)$ using the system input $x_j(t)$ and the exited output response $y_{ij}(t)$. Because $\boldsymbol{H}_{fit}(s)$ is obtained as a ratio of $y_{ij}(t)$ and $x_j(t)$ in Laplace domain, $x_j(t)$ may be taken to be an arbitrary function, provided that it is broadband enough to cover the frequency range of interest. Hence, we use a Gaussian pulse with 60 dB bandwidth at the upper frequency limit of interest, *W*, as the excitation $x_j(t)$

$$x_j(t) = \frac{1}{\alpha\sqrt{\pi}} U_0 e^{-\left(\frac{t-t_0}{\alpha}\right)^2}, \tag{2.33}$$

where $\alpha$ is used to set the frequency bandwidth, while turn-on delay $t_0$ is chosen such that $x_j(t) \approx 0$ for $t < 0$. In the frequency domain, the spectrum is

$$X_j(f) = U_0 e^{-[(\pi f \alpha)^2 + j2\pi f t_0]}. \tag{2.34}$$

The transient responses, $y_{ij}(t)$, are recorded at the output ports until the waveform is time-limited to $(T + t_0)$ in a sense that

$$y_{ij}(t) = \frac{|\, y_{ij}(t)\,|}{\max(|\, y_{ij}(t)\,|)} < \varepsilon \quad \text{for } t > (T + t_0), \tag{2.35}$$

where $\varepsilon$ is a small positive number, such that it ensures that the response is practically over. The recorded $y_{ij}(t)$ are utilized by the TDVF process. This representation of $y_{ij}(t)$ is reasonable in a passive system because the output responses decay due to the internal loss. In this dissertation, the choice $\varepsilon = 10^{-2}$ has proven to be satisfactory for the example cases considered. However, it is understood that the choice of $\varepsilon$ must be guided by the attributes of the response of the DUT. For example, when there are strong resonances that dominate the response of the DUT, even reflected waves of small magnitude may not be negligible, and $\varepsilon$ should be properly chosen to account for their impact.

## 2.4 Element-by-Element Matrix Rational Function Approximation

Despite the desire to simultaneously fit all elements of the network matrix of a passive electromagnetic multiport using matrix rational function fitting employing a single set of poles, this option may not be feasible when the number of ports is large and the system frequency response spans several tens of GHz while at the same time exhibiting a rich resonant content. For such cases, which are often encountered in the context of signal and power integrity analysis of packaged electronic systems, an

alternative to the matrix rational fitting is to apply an element-by-element fitting of the network matrix using, for example, VF [22,23].

When we look into the structure of $\boldsymbol{A}_f$ in (2.21), it is a block triangular form [46]. The whole matrix $\boldsymbol{A}_f$ is sparse, but the blocks of $\boldsymbol{\Omega}_{f,k}$ and $\boldsymbol{\Omega}_f$ are dense. Because the least squares problem is overdetermined, the blocks are all rectangular. The variables $\boldsymbol{u}_k$ corresponding to the block $\boldsymbol{\Omega}_f$ are only coupled to the variables $\tilde{\boldsymbol{u}}$. Thus the block triangular form of $\boldsymbol{A}_f$ can be substructured or dissected, which provides efficiency in both solution time and storage requirements. We call this dissection element-by-element fitting.

The element-by-element handling casts Equation (2.21) in the form

$$\boldsymbol{A}_{f,k} \cdot \boldsymbol{u}_k = \boldsymbol{b}_{f,k} \tag{2.36}$$

$$\begin{aligned}
&\boldsymbol{A}_{f,k} = \left[ \boldsymbol{\Omega}_f \;\; \boldsymbol{\Omega}_{f,k} \right], \\
&\boldsymbol{\Omega}_f = \begin{bmatrix} \dfrac{1}{s_1 - \tilde{q}_{1,k}} & \cdots & \dfrac{1}{s_1 - \tilde{q}_{N_k,k}} & 1 & s_1 \\ \vdots & \ddots & \vdots & \vdots & \vdots \\ \dfrac{1}{s_{M_f} - \tilde{q}_{1,k}} & \cdots & \dfrac{1}{s_{M_f} - \tilde{q}_{N_k,k}} & 1 & s_{M_f} \end{bmatrix}, \\
&\boldsymbol{\Omega}_{f,k} = \begin{bmatrix} \dfrac{-H_k(s_1)}{s_1 - \tilde{q}_{1,k}} & \cdots & \dfrac{-H_k(s_1)}{s_1 - \tilde{q}_{N_k,ij}} \\ \vdots & \ddots & \vdots \\ \dfrac{-H_k(s_{M_f})}{s_{M_f} - \tilde{q}_{1,k}} & \cdots & \dfrac{-H_k(s_{M_f})}{s_{M_f} - \tilde{q}_{N_k,k}} \end{bmatrix}, \\
&\boldsymbol{u}_k = \left[ r'_{1,k} \cdots r'_{N_k,k} \;\; d'_k \;\; e'_k \;\; \tilde{r}_{1,k} \cdots \tilde{r}_{N_k,k} \right]^T, \boldsymbol{b}_{f,k} = \left[ H_k(s_1) \cdots H_k(s_{M_f}) \right]^T,
\end{aligned} \tag{2.37}$$

where $1 \le k \le K$ . For the computation of (2.36), it is noted that in addition to the fact that these computations can be done in parallel, the computations result in a different set of the coefficients of $\sigma(s)$ for each element of the network matrix, which means the element-by-element fitting has a different set of poles for each element in the matrix.

When a passive $N_p$ – port system represented by its matrix transfer function is considered and it is approximated with an element-by-element rational function approximation, the generalized mathematical representation of each element $(i, j)$ of $\boldsymbol{H}(s)$ can be written as

$$\{\boldsymbol{H}_{fit}(s)\}_{ij} = \sum_{m=1}^{N_{ij}} \frac{r_{m,ij}}{s - q_{m,ij}} + d_{ij} + s e_{ij}. \tag{2.38}$$

In the above equation, $N_{ij}$ is the order of the rational function fit for the element $(i, j)$ of $\boldsymbol{H}(s)$, and $d_{ij}$, $e_{ij}$, $q_{m,ij}$ and $r_{m,ij}$ are constants generated by the rational fitting process. In contrast to the matrix fitter process [23], which is presented in (2.16), all the elements of the matrix $\boldsymbol{H}$(s) are not sharing a common set of poles, so the order of the rational fit can be different for different elements in (2.36).

### 2.4.1 Comparison between the VF and the element-by-element VF

The matrix fitting of VF with $M_f$ samples, $N$ poles for a passive $N_p$ -port system involves the following operations:

- Calculation of poles from starting poles

1) Calculation of coefficient of $\sigma(s)$ by solving the least squares problem $\boldsymbol{A}\cdot\boldsymbol{u}=\boldsymbol{b}$, where $\boldsymbol{A}$ is a sparse matrix of dimension $(2M_f K)$ x $((N+2)K+N)$.

2) Calculation of zeros (new poles) by calculating eigenvalues of a matrix of dimension *N* x *N*.

- Calculation of residues with the new poles by solving the least squares problem $\boldsymbol{A}\cdot\boldsymbol{u}=\boldsymbol{b}$ where $\boldsymbol{A}$ has dimension $(2M_f K)$ x $((N+2)K)$, where *K* is the number of the fitting elements.

On the other hand, the element-by-element fitting with $M_f$ samples, *N* poles for a passive $N_p$-port system repeats the following operations *K* times:

- Calculation of poles from starting poles:

  1) Calculation of coefficient of $\sigma(s)$ by solving the least squares problem $\boldsymbol{A}\cdot\boldsymbol{u}=\boldsymbol{b}$, where $\boldsymbol{A}$ is a dense matrix of dimension $(2M_f)$ x $(2N+2)$.

  2) Calculation of zeros (new poles) by calculating eigenvalues of a *N*-by-*N* matrix.

- Calculation of residues with the new poles by solving the least squares problem $\boldsymbol{A}\cdot\boldsymbol{u}=\boldsymbol{b}$ where $\boldsymbol{A}$ has dimension $2M_f$ x $(N+2)$.

First, we concern ourselves with the issue of the storage requirements. When the nonzero entries of $\boldsymbol{A}$ at the first step in the calculation of poles are counted for storage requirements, the storage required for matrix fitting is at least *K* times larger than that for the element-by-element fitting. In this estimate the fact that only the nonzero

entries of $\boldsymbol{A}$ are considered in the sparse matrix structure representation of $\boldsymbol{A}$ in the MATLAB environment is taken into account. The data structure stores nonzero entries with their indices.

Next, we examine the operation time at each step for the element-by-element fitting. For a *m* x *n* dense matrix $\boldsymbol{A}$, the "\" operator in MATLAB solves the least squares problem making use of the householder method, and it requires about $2mn^2 - 2n^3/3$ flops. Hence, the calculation of the coefficients of $\sigma(s)$ requires about $16M_f N^2 - 16N^3/3$ flops and the calculation of residues requires about $4M_f N^2 - 2N^3/3$ flops. The former case is more expensive. For the eigenvalue calculation of an *N* x *N* matrix via Hessenberg reduction and QR iteration, it requires roughly $10N^3$ flops, which is smaller value than $16M_f N^2 - 16N^3/3$ because $M_f \geq N$. Thus, the calculation of the coefficients of $\sigma(s)$ is the most time-consuming part of the overall process. Therefore, we are going to consider the computational cost for the calculation of the coefficients of $\sigma(s)$ as the metric for comparison of the complexity of the matrix fitting and the element-by-element fitting.

For the QR factorization in the calculation of coefficient of $\sigma(s)$, the element-by-element fitting requires $(16M_f N^2 - 16N^3/3)K$ flops because the process is repeated $K$ times, while the matrix fitting requires about $(16M_f N^2 - 16N^3/3)K^3$ flops assuming that the matrix is a dense matrix. As the number of ports and the number of fitting elements increase, the operation time for the matrix fitting increases much more

rapidly than the element-by-element fitting. In general, since the upper triangular part of $\boldsymbol{H}(s)$ is only considered, $K = N_p(N_p+1)/2$. In this context, the matrix fitting becomes much slower than the element-by-element as the number of port increases.

However, the matrix fitting program of VF, which is available at [47], is implemented using sparse matrix storage and operations in MATLAB, which are different from those we used for the element-by-element fitting. This prevents us from doing a thorough comparison of the computational cost of the two approaches.

However, for two reasons, we still reach the conclusion that the element-by-element fitting is faster than the matrix fitting for a multiport system when the number of ports is large. The first reason is that the "\" operator is used in MATLAB is implemented for the general form of $\boldsymbol{A}$ in order to limit matrix fill due to new nonzero elements generated during the sparse matrix operations [48]. The fill may incur additional operations because it may eventually be annihilated in order to obtain the triangular factors depending on their locations. On the other hand, the matrix $\boldsymbol{A}$ in the dissected block of the element-by-element fitting is dense, and the element-by-element fitting method does not introduce any additional fill. The second reason is that the operation time per flop for a sparse data structure is longer than that for a dense matrix [48]. Even if the "\" operator in MATLAB factorizes the sparse matrix $\boldsymbol{A}$ without generating any fill and it requires about the same flops as the element-by-element fitting, the matrix fitting is much slower than the element-by-element fitting because of its slow flop speed.

It is known that the time-domain simulation for the element-by-element fitting is inefficient because the generated rational function fit involves large dimensions of state equation representations [49]. However, the inefficiency happens only when the state equation representation is used for the time-domain simulation. For the case of the SPICE-compatible equivalent circuit synthesis, element-by-element fitting does not increase complexity of the equivalent circuit or degrade computational efficiency because the circuits are synthesized for each partial term in each element in the network matrix of the rational function representation in (2.6) [23]. This will become clear in Chapter 7.

Also for computational cost of enforcing passivity of the generated rational function fit, the passivity enforcement via quadratic programming, which is discussed in Chapter 6, shows the same computational efficiency both for the matrix rational fitting and the element-by-element fitting.

Actually, the number of poles for the matrix fitting is larger than that of the element-by-element fitting because the common set of poles for the matrix fitting is determined in a manner such that the response attributes of all elements in the matrix are accurately fitted [50]. Finally, the element-by-element fitting is also more efficient than the matrix fitting in the context of passivity enforcement via quadratic programming because of the smaller order used in the fit of each element in the matrix response.

For the purpose of providing a practical comparison of the two approaches to rational fitting, measured admittance matrix data of a 2-port interconnect structure

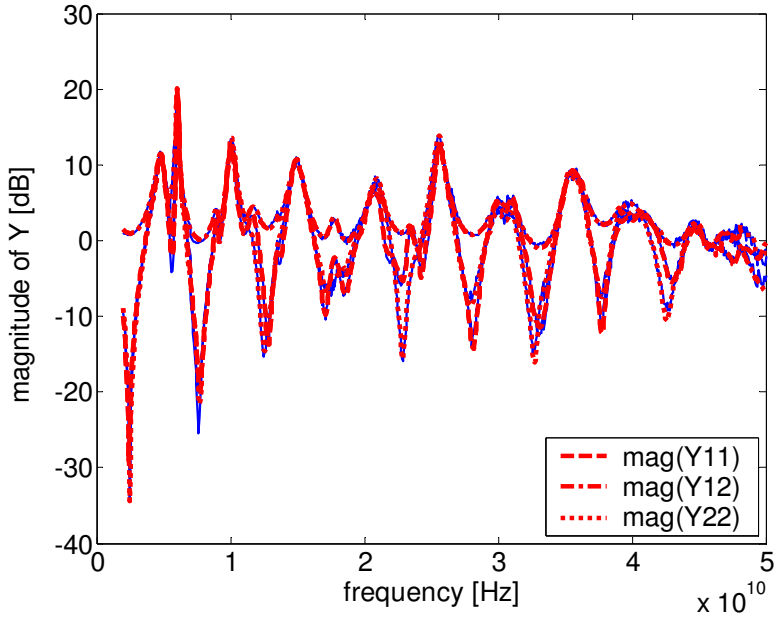
over the bandwidth 2 GHz < $f$ < 50 GHz were used. The available spectra were sampled at 801 points over the aforementioned bandwidth. All computations are done using MATLAB in an IBM notebook computer with an Intel Pentium D processor (1.7 GHz clock frequency) and 1.25 GB of RAM. The matrix entries are stored as double precision floating point values. For the matrix fitting with order 70 and with the constant term and the linear term included in the fit (see Equation (2.16)), the operation time was 20.34 s, the memory for the matrix $\boldsymbol{A}$ was 8.19 MB, and the RMS error was 0.13253. For the element-by-element fitting with order 52 with same conditions as the matrix fitting except the order, the computation time was 2.33 s, the memory for the matrix $\boldsymbol{A}$ was 1.36 MB, and the RMS error was 0.13006. The element-by-element rational function fitting is faster than the matrix fitting in this validation study. Also the element-by-element requires smaller order than the matrix fitting for generating the rational fit with about the same accuracy. The comparison of the element-by-element fitted admittances with the measured data is depicted in Figure 2.1. Very good agreement is observed. This result clearly supports the discussion that the element-by-element fitting is more efficient in the operation time and storage requirement than the matrix fitting.

## 2.5 State Equation Representation of Synthesized Linear Networks

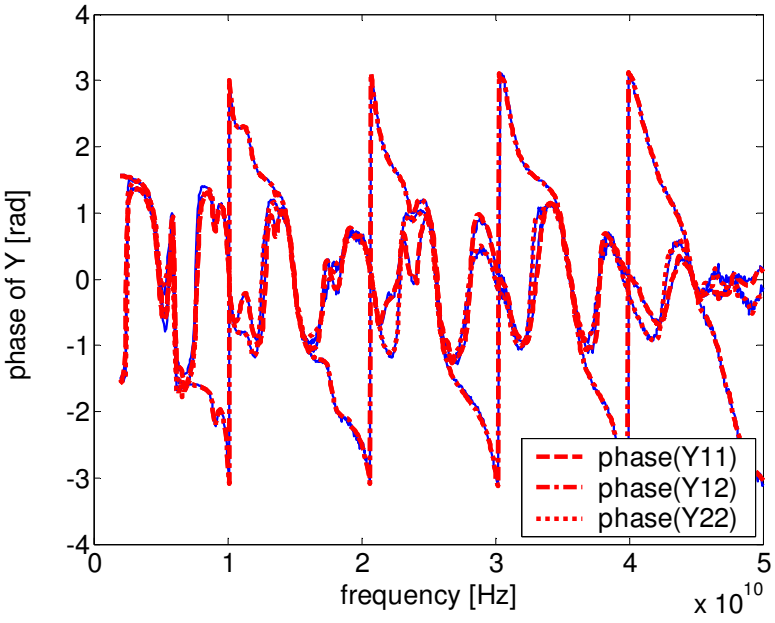
In matrix form, (2.16) and (2.38) can be written in a state equation form as follows:

$$\boldsymbol{H}_{fit}(s) = \boldsymbol{C}(s\boldsymbol{I} - \boldsymbol{A})^{-1}\boldsymbol{B} + \boldsymbol{D} + s\boldsymbol{E}. \tag{2.39}$$

The elements of $\boldsymbol{A}$ and $\boldsymbol{C}$ are either real or complex numbers which come in complex conjugate pairs. $\boldsymbol{D}$ and $\boldsymbol{E}$ can be set to be zero. When $\boldsymbol{E}$ is zero, (2.39) can




(a)




(b)

**Figure 2.1** Comparisons of the measurement data and their approximations via the element-by-element VF.

be expressed in state-space form as

$$\begin{aligned} \dot{\boldsymbol{z}}(t) &= \boldsymbol{A}\boldsymbol{z}(t) + \boldsymbol{B}\boldsymbol{x}(t) \\ \boldsymbol{y}(t) &= \boldsymbol{C}\boldsymbol{z}(t) + \boldsymbol{D}\boldsymbol{x}(t), \end{aligned} \tag{2.40}$$

where $\boldsymbol{x}(t)$ and $\boldsymbol{y}(t)$ are the input and the output of the system, and $\boldsymbol{z}(t)$ is the state vector.

To fix ideas in terms of a specific simple example, consider a two-port system for which the matrix fitting results in a rational function of order 3. Then the matrices in (2.40) assume the explicit form,

$$\begin{aligned} &\boldsymbol{A} = \mathrm{diag}(p_1 \quad p_2 \quad p_3 \quad p_1 \quad p_2 \quad p_3)\ ,\ \boldsymbol{B}^T = \begin{bmatrix} 1 & 1 & 1 & 0 & 0 & 0 \\ 0 & 0 & 0 & 1 & 1 & 1 \end{bmatrix}, \\ &\boldsymbol{C} = \begin{bmatrix} R_{1,11} & R_{2,11} & R_{3,11} & R_{1,12} & R_{2,12} & R_{3,12} \\ R_{1,21} & R_{2,21} & R_{3,21} & R_{1,22} & R_{2,22} & R_{3,22} \end{bmatrix}, \\ &\boldsymbol{D} = \begin{bmatrix} D_{11} & D_{12} \\ D_{21} & D_{22} \end{bmatrix},\ \boldsymbol{E} = \begin{bmatrix} E_{11} & E_{12} \\ E_{21} & E_{22} \end{bmatrix}. \end{aligned} \tag{2.41}$$

On the other hand, an element-by-element fitting of the elements of the admittance matrix, assuming for simplicity and without loss of generality that the same order of 3 is used for all four elements, yields, in the form of (2.40), the following matrices:

$$\begin{aligned} &\boldsymbol{A} = \mathrm{diag}(p_{1,11}\ p_{2,11}\ p_{3,11}\ p_{1,12}\ p_{2,12}\ p_{3,12}\ p_{1,21}\ p_{2,21}\ p_{3,21}\ p_{1,22}\ p_{2,22}\ p_{3,22})\ , \\ &\boldsymbol{B}^T = \begin{bmatrix} 1\ 1\ 1\ 0\ 0\ 0\ 0\ 0\ 0\ 0\ 0\ 0 \\ 0\ 0\ 0\ 1\ 1\ 1\ 0\ 0\ 0\ 0\ 0\ 0 \\ 0\ 0\ 0\ 0\ 0\ 0\ 1\ 1\ 1\ 0\ 0\ 0 \\ 0\ 0\ 0\ 0\ 0\ 0\ 0\ 0\ 0\ 1\ 1\ 1 \end{bmatrix}, \\ &\boldsymbol{C} = \begin{bmatrix} R_{1,11} & R_{2,11} & R_{3,11} & R_{1,12} & R_{2,12} & R_{3,12} & 0 & 0 & 0 & 0 & 0 & 0 \\ 0 & 0 & 0 & 0 & 0 & 0 & R_{1,21} & R_{2,21} & R_{3,21} & R_{1,22} & R_{2,22} & R_{3,22} \end{bmatrix}, \\ &\boldsymbol{D} = \begin{bmatrix} D_{11} & D_{12} \\ D_{21} & D_{22} \end{bmatrix},\ \boldsymbol{E} = \begin{bmatrix} E_{11} & E_{12} \\ E_{21} & E_{22} \end{bmatrix}. \end{aligned} \tag{2.42}$$

To avoid complex numbers in the matrices $\boldsymbol{A}$ and $\boldsymbol{C}$, we can express the matrices using only real numbers via a similarity transformation. In view of the realness of the system, the complex poles come in complex conjugate pairs,

$$H(s) = \frac{r}{s-p} + \frac{\overline{r}}{s-\overline{p}}, \tag{2.43}$$

where $p = \sigma + j\omega$ and $r = \alpha + j\beta$. In a state-space realization of (2.40), the matrices are expressed as

$$\boldsymbol{A} = \begin{bmatrix} \sigma + j\omega & 0 \\ 0 & \sigma - j\omega \end{bmatrix}, \boldsymbol{b} = \begin{bmatrix} 1 \\ 1 \end{bmatrix}, \boldsymbol{C} = \begin{bmatrix} \alpha + j\beta & \alpha - j\beta \end{bmatrix}. \tag{2.44}$$

When we apply a similar transformation using the matrix

$$\boldsymbol{J} = \begin{bmatrix} 1 & 1 \\ j & -j \end{bmatrix}, \tag{2.45}$$

we obtain equivalent matrices as follows:

$$\boldsymbol{A}' = \boldsymbol{J}\boldsymbol{A}\boldsymbol{J}^{-1} = \begin{bmatrix} \sigma & -\omega \\ \omega & \sigma \end{bmatrix}, \boldsymbol{b}' = \boldsymbol{J}\boldsymbol{b} = \begin{bmatrix} 2 \\ 0 \end{bmatrix}, \boldsymbol{C}' = \boldsymbol{C}\boldsymbol{J}^{-1} = [\alpha \quad \beta]. \tag{2.46}$$

The matrices in (2.40) have only real numbers.

# CHAPTER 3
# ORDER ESTIMATION OF RATIONAL FUNCTION APPROXIMATION OF NETWORK TRANSFER FUNCTION

TDVF is not as popular and widely used as VF for rational function fitting of linear network transfer functions, even though it is common for transient data to be available as a means of representation of the system response properties. One of the reasons for this is that, in contrast to VF [23, 51], there exist no robust guidelines for the estimation of the order of the rational function fit using TDVF.

The main objective of this chapter is to propose a methodology for estimating the order of the rational function fitting needed for accurate macromodel generation using TDVF. This technique is based on the *WT* rule, which defines a relation between the order, *N*, of the rational function approximation, the time duration, *T*, of a signal in time and its frequency bandwidth *W*. The *WT* rule is derived from the 2*WT* theorem [52, 53], which is successfully applied to the macromodeling work pursued in Sarkar's group [54, 55]. Their experience with the use of the 2*WT* theorem motivated our work. As will be shown next, the proposed *WT* rule can provide a guideline for determining the order of TDVF from system responses in TD, and thus facilitate automation of the fitting process.

In what follows our development is in the context of the element-by-element fitting of the system network matrix. In addition, we choose to work with the scattering-parameter matrix because of the time-limited nature of their time-dependent transmission and reflection coefficients due to the use of resistive terminations at the ports for their calculation.

## 3.1 *WT* Rule, Order Estimation for TDVF

For simplicity and without loss of generality, a single-input single-output (SISO) passive system is considered. TDVF constructs rational function approximation $H_{fit}(s)$ for the system transfer function using the input $x(t)$ and the excited output response $y(t)$ as explained in Chapter 2. The excitation input $x(t)$ is set to be a Gaussian pulse with 60 dB bandwidth at the upper frequency limit of interest, *W*, as presented in Equation (2.33). Furthermore, it is assumed that $x(t)$ and $y(t)$, which are used as inputs to TDVF, are truncated in time at $(T + t_0)$. Recall that $y(t)$ being time-limited to $(T + t_0)$ is understood to mean that

$$\frac{|\, y(t)\,|}{\max(|\, y(t)\,|)} < \varepsilon \qquad \text{for } t > (T + t_0) \tag{3.1}$$

where $\varepsilon$ is set to be 0.01 (see Section 2.3.1 for the definition of *T*).

In the frequency domain, the input and output relation is presented as

$$Y(s) = H(s)X(s) \approx H_{fit}(s)X(s), \tag{3.2}$$

where $H(s)$ is the transfer function, $X(s)$ and $Y(s)$ are, respectively, the Laplace transforms of $x(t)$ and $y(t)$. Because $X(s)$ is band-limited to $f = W$, $Y(s)$ is also band-

limited to $f = W$, even if $H(s)$ is not. It is worthwhile to note that in this work, the time-limited and band-limited attributes of the response are defined based on the absolute value of a signal relative to its maximum value as presented in (2.33) and (3.1) [54, 55], instead of being defined strictly according to [52, 53].

From the *2WT* theorem [53], a signal $y(t)$ that is time-limited to $(T + t_0)$ and band-limited to *W*, has a Fourier series description as

$$\begin{aligned} y(t) &= \sum_{0}^{\infty} a_n \cos 2\pi f_n t + \sum_{1}^{\infty} b_n \sin 2\pi f_n t, \\ f_n &= \frac{n}{(T + t_0)}, \end{aligned} \tag{3.3}$$

which is valid for $0 < t < T + t_0$, and it can be rewritten as

$$y(t) = \sum_{0}^{\infty} \left( \frac{a_n}{2} + \frac{b_n}{2} \right) \exp(j2\pi f_n t) + \sum_{0}^{\infty} \left( \frac{a_n}{2} - \frac{b_n}{2} \right) \exp(-j2\pi f_n t). \tag{3.4}$$

When the frequency interval of interest is $-W \le f \le W$, $y(t)$ has about $2W(T + t_0) + 1$ nonzero terms in its frequency spectrum.

The order of the rational function approximation is the number of poles, or equivalently, the dimension of the rational function space upon which the frequency data is projected. The projection is carried out in the context of VF through a least squares problem. Therefore, to solve the least squares problem, the order of the rational function approximation (which determines the number of columns of the matrix in the least squares problem) should be larger than or equal to the number of equations (which is the number of row of the matrix) which, in turn, is determined by the number of frequency data. In the fitting process used in VF, only positive

frequencies are used [22, 23]. Therefore, to solve the least squares problem, the number of frequency data, $N_f$, should be larger than the order, which leads to

$$N_y \le N_f, \tag{3.5}$$

where $N_y$ is the order of rational function fit for $Y(s)$.

From the $2WT$ theorem, the time-limited signal $y(t)$ has $W(T + t_0)$ nonzero frequency terms in $0 \le f \le W$, and thus

$$N_y \le N_f \approx W(T + t_0). \tag{3.6}$$

However, TDVF is designed to macromodel the transfer function $H(s)$ instead of $Y(s)$. Hence, the order for the fitting of $H(s)$ should be derived from the order of $Y(s)$ using (3.2).

From (3.2), the order of $Y(s)$ can be presented in terms those for $X(s)$ and $H(s)$:

$$O(Y) \le O(H) + O(X), \tag{3.7}$$

where $O(F)$ represents the order of a rational function representation of the function $F$. The validity of (3.6) can be simply justified as follows.

Let $X(s)$ and $H(s)$ be represented in terms of rational functions as

$$\begin{aligned} X(s) &= \sum_{m=1}^{N_x} \frac{R_{xm}}{s - p_{xm}} + D_x + sE_x \\ H(s) &= \sum_{m=1}^{N} \frac{R_m}{s - p_m} + D + sE, \end{aligned} \tag{3.8}$$

where $N_x$ and $N$ are, respectively, the orders of the rational function fits for $X(s)$ and $H(s)$. The two rational function approximations are multiplied as in (3.2), to yield $Y(s)$ as follows.

$$Y(s) = \left( \sum_{m=1}^{N_x} \frac{R_{xm}}{s - p_{xm}} + D_x + sE_x \right) \left( \sum_{m=1}^{N} \frac{R_m}{s - p_m} + D + sE \right) \tag{3.9}$$

$$= \left( \frac{R_{x1}}{s - p_{x1}} + \frac{R_{x2}}{s - p_{x2}} + \cdots + D_x + sE_x \right) \left( \frac{R_1}{s - p_1} + \frac{R_2}{s - p_2} + \cdots + D + sE \right).$$

When the obtained expression for $Y(s)$ from (3.9) is decomposed into partial fractions, $Y(s)$ has at most all the poles of $X(s)$ and $H(s)$ in the form of union, and the order of $Y(s)$ satisfies the relation in (3.6).

Upon further consideration, $X(s)$ is a delayed Gaussian function that is smooth in magnitude and has variations in phase due to the delay. $N_x$ is determined to present the variation of phase incurred by the turn-on delay, $t_0$; hence, when the turn-on delay is subtracted from the time duration of $y(t)$ in (3.6), Equation (3.6) is modified for $N$

$$N \le TW. \tag{3.10}$$

Equation (3.10) informs the upper limit of the order for TDVF. The upper limit increases as the duration $T$ and bandwidth $W$ increase. Typically, $N$ is chosen to be

$$N \approx WT. \tag{3.11}$$

## 3.2 Validation Studies

The validity the proposed WT rule is demonstrated using two interconnect systems providing a guideline to estimate the order for TDVF. For the time-domain data

computation, the Gaussian pulse in (2.33) was used. To check the accuracy of the generated rational function fit, the RMS (root mean square) error is used. The RMS error in TD is computed as the relative value to the peak value of the Gaussian pulse input.

### 3.2.1 A four-port interconnect system

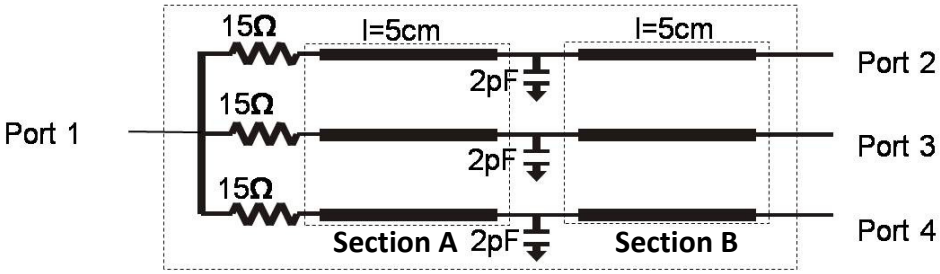



**Figure 3.1** A four-port interconnect system involving two cascaded sections of coupled transmission lines [56].

The first numerical study concerns a four-port interconnect system characterized by S-parameter data up to 10 GHz. The system is shown in Figure 3.1. The two sections of multiconductor interconnects are identical, with per-unit-length (p.u.l.) inductance and capacitance matrices given by

$$\boldsymbol{L} = \begin{bmatrix} 4.976 & 0.765 & 0 \\ 0.765 & 4.975 & 0.765 \\ 0 & 0.765 & 4.975 \end{bmatrix},$$

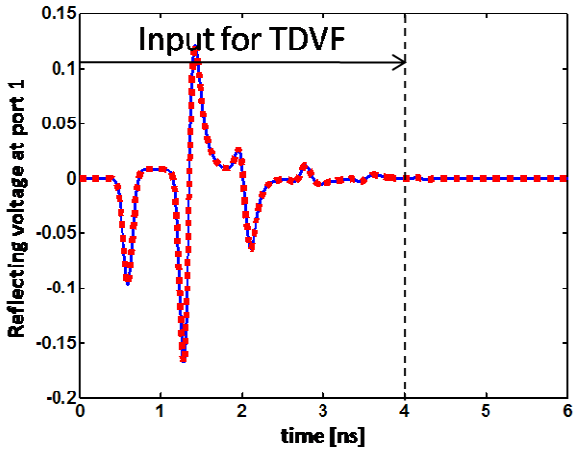
$$\boldsymbol{C} = \begin{bmatrix} 1.082 & -0.197 & 0 \\ -0.197 & 1.124 & -0.197 \\ 0 & -0.197 & 1.082 \end{bmatrix}.$$

The p.u.l. conductance matrix is taken to be zero while a p.u.l. resistance of 3.448 Ω/cm is assumed for each wire.

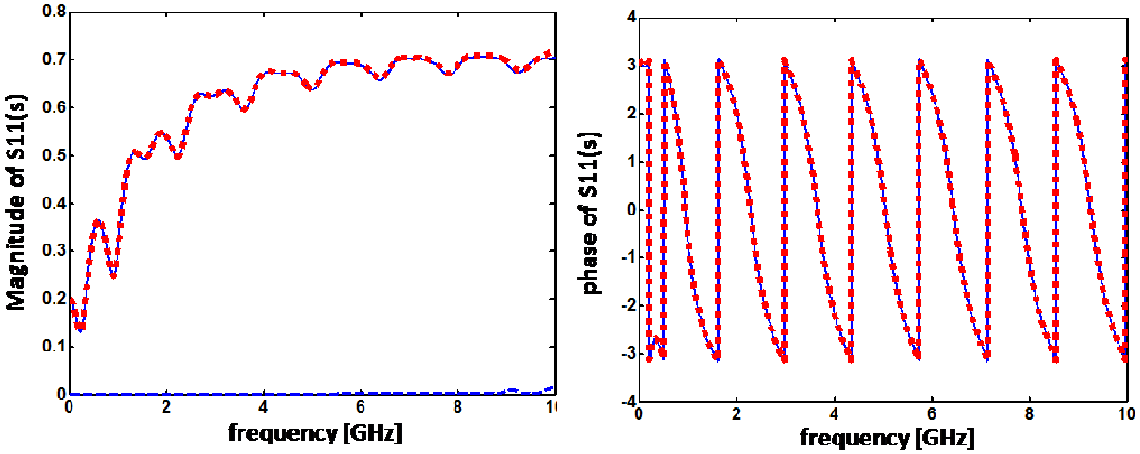
For this validation study, we only fitted the reflection coefficient at port 1, $S_{11}$, over the frequency region up to 10 GHz ($W = 10^{10}$). The $S_{11}$ was chosen as a representative element in the 4 x 4 scattering matrix of the interconnect system. The characteristic impedance for definition of the scattering matrix was 50 Ω.

The time-domain data was obtained via HSPICE as follows. First, all ports except Port 1 were terminated with 50 Ω, and Port 1 was connected to a source that had a source resistor of 50 Ω. A Gaussian pulse with 60 dB bandwidth at 10 GHz, which had twice the value of (2.33) when $U_0 = \alpha\sqrt{\pi}/2$ and a turn-on delay of 0.6 ns, was assigned to the source. Due to this doubling, $x_1(t)$ had the exact value of the Gaussian pulse as described in (2.33). The pulse was sampled with the time step $\Delta t = 5$ ps, and the reflected voltage wave at port 1, $y_{11}(t)$, was analyzed by HSPICE [33]. The obtained $y_{11}(t)$ is plotted in Figure 3.2(a) as a solid line.

The transient data for $x_1(t)$ and $y_{11}(t)$ were truncated at $t = 4$ ns. This is consistent with a value of $\varepsilon = 10^{-2}$ according to (3.1). From Figure 3.2(a), a choice of $T = 3.4$ ns should be acceptable for choosing *N* according to the *WT* rule. Hence, with the predetermined value $W = 10^{10}$, and $T = 3.4$ ns, we obtain $N = 34$. Thus, the truncated time-domain data were put into the TDVF process with the estimated order 34.




(a)




(b) (c)

**Figure 3.2** Comparison of reference values and the data from the macromodel of TDVF. (a) Reflected voltage wave at port 1 (solid line: HSPICE reference solution; dots: TDVF interpolated/extrapolated response). (b) Magnitude and (c) phase of $S_{11}$ (solid line: FD data from Fourier transform; bold dots: data from the TDVF rational approximation; dotted line: error).

Both time-domain and frequency-domain data obtained from the constructed macromodel of $S_{11}$ are presented as dotted lines in Figure 3.2 compared with reference values. The time-domain data, $y_{11}(t)$, from the generated rational fit were extrapolated via recursive convolution and the reference values in the frequency domain were obtained from the Fourier transform of the time-domain data, $x_1(t)$, and $y_{11}(t)$, which were truncated at $t = 15\,\text{ns}$. Very good agreement is observed. The RMS error is $1.083\text{x}10^{-5}$ in the time domain and 0.0038 in the frequency domain.

Next, RMS errors in the time domain and the frequency domain are plotted for various values of the order *N* and the time support *T* in gray scale in Figures 3.3 and 3.4. In the figures, RMS errors show the tendency to decrease as the order *N* and the time support *T* increase. However, boundaries of *N* which support accurate macromodeling exist. Moreover, the boundary values of *N* in the time domain and frequency domain are different when the acceptable RMS error is smaller than 0.01. The time-domain region which covers acceptable RMS errors is larger than the frequency-domain region. It means that the accuracy of the generated macromodel in the time domain cannot guarantee the accuracy in the frequency domain even though, practically, we can check the accuracy only in the time domain. For example, when *T* is 5 ns, the order *N* 100 and the number of iterations 5, the RMS error is $3.0741\text{x}10^{-6}$ in TD and 7.0450 in FD. Even though the RMS error in the time domain is much smaller than 0.01, the error in the frequency domain is not acceptable.

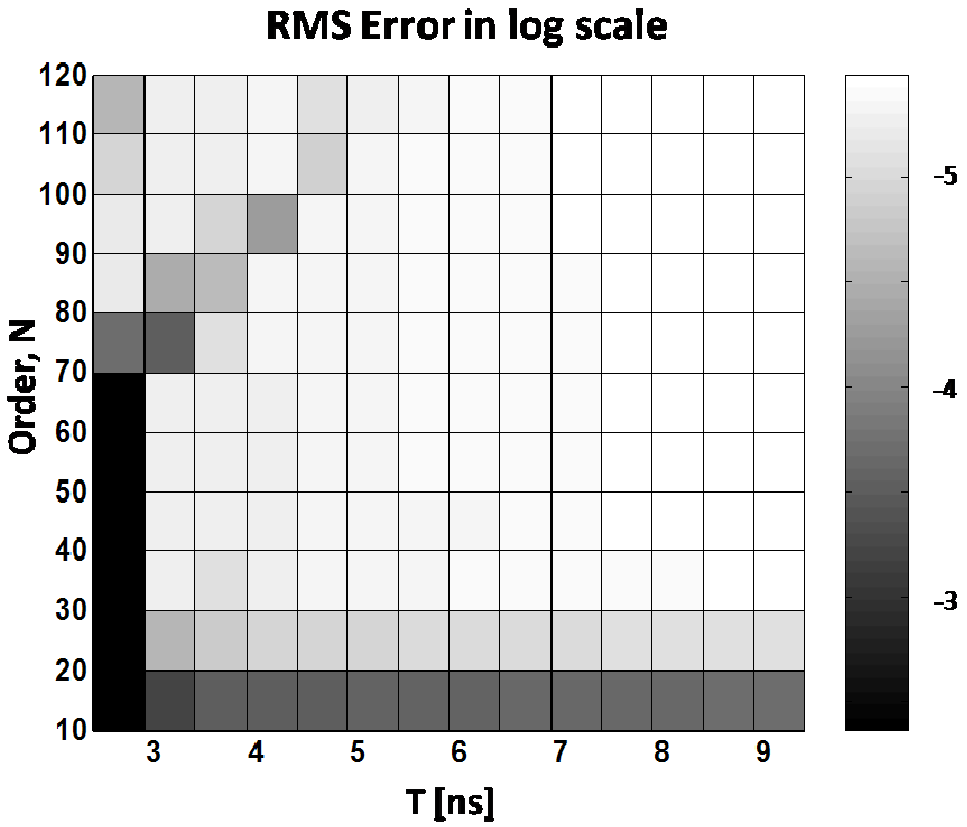



**Figure 3.3** RMS error in gray scale for time-domain data.

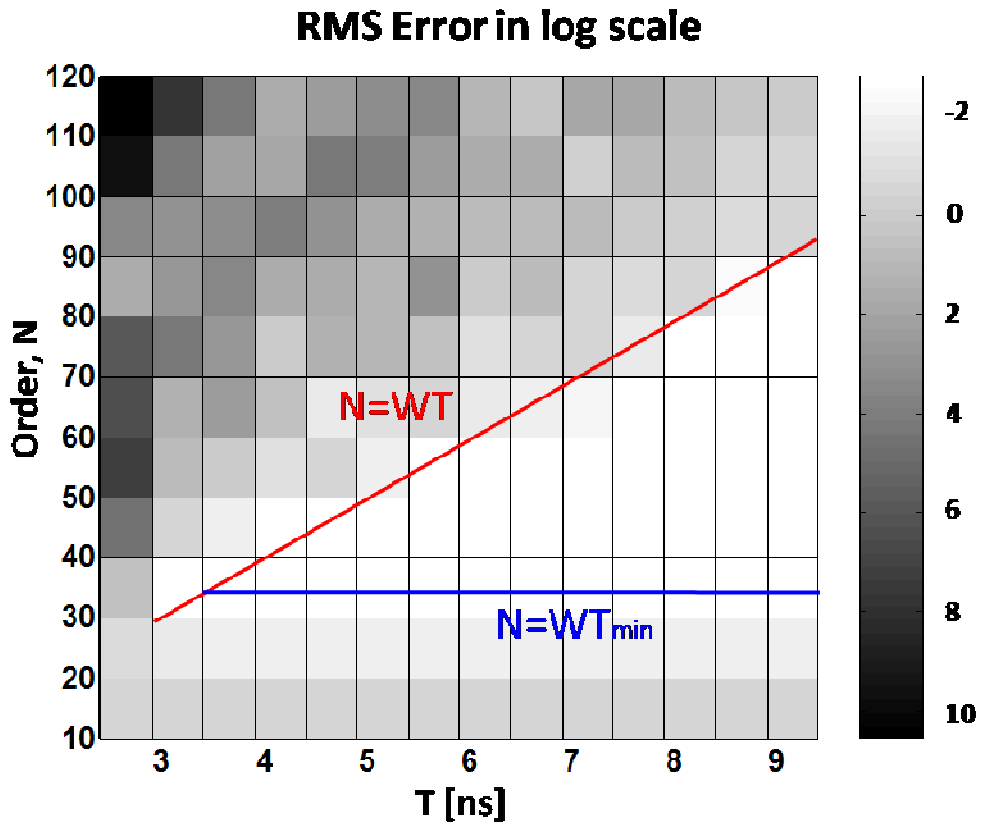



**Figure 3.4** RMS error in gray scale for frequency-domain data.

To demonstrate the validity of the *WT* rule, we draw the line of $WT$ and $WT_{\min}$ (=34) in Figure 3.4. The two lines almost correspond to the boundaries of the region of *N* which supports accurate construction of the macromodel via TDVF. This demonstrates that the *WT* rule in (3.10) can provide a guideline in (3.11) to determine the order of TDVF from the provided time-domain data supporting the accuracy of the macromodel.

### 3.2.2 A SISO interconnect system

The second numerical study concerns the SISO (single input/single output) interconnect circuit system depicted in Figure 3.5; the subcircuit, "sub_crt," involves seven transmission lines. All lines are lossy with the same p.u.l. resistance of 0.1 Ω/cm and zero p.u.l. conductance. The p.u.l. capacitance, *C*, p.u.l. inductance *L*, and length *l* of the lines are as follows. For T1, *C* = 1 pF/cm, *L* = 0.6 nH/ cm, and *l* = 3 cm. For T2, *C* = 1 pF/cm, *L* = 1 nH/ cm, and *l* = 5 cm. For T3, *C* = 1.2 pF/cm, *L* = 0.6 nH/ cm, and *l* = 3 cm. For T4, *C* = 1 pF/cm, *L* = 0.6 nH/ cm, and *l* = 4 cm. For T5, *C* = 1.5 pF/cm, *L* = 1 nH/ cm, and *l* = 2 cm [56].

The SISO interconnect system was analyzed using HSPICE to obtain the time-domain data required for the rational function fitting up to 5 GHz. The Gaussian pulse with a 60 dB bandwidth at 5 GHz ($W = 5\text{x}10^9$), which was sampled every 5 ps, was assigned to $V_{\text{in}}$ as an excitation. The turn-on delay, $t_0$, of the Gaussian pulse was 1.5 ns and $U_0 = \alpha\sqrt{\pi}$. The output voltage was recorded at the junction of the first and second subcircuits. The time response used for fitting was truncated at 8 ns (*T* = 6.5

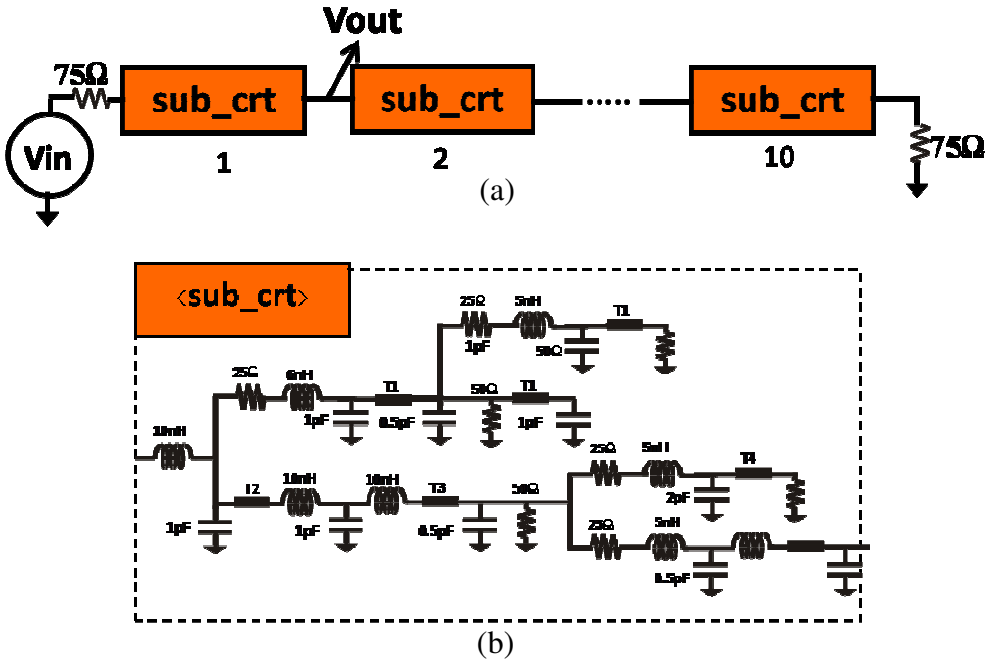



**Figure 3.5** SISO interconnect system. (a) Whole circuit and (b) subcircuit.

ns). This was dictated by the criteria in (3.1) for a value of $\varepsilon = 10^{-2}$. With $T$ taken to be 6.5 ns and $W = 5\text{x}10^{9}$, the order for TDVF was taken to be $WT \approx 34$ according to the $WT$ rule.

The plots in Figure 3.6 depict the accuracy achieved with this order of the rational fitting. The time-domain data from the generated rational fit were extrapolated via recursive convolution, and the values are presented as a dotted line in Figure 3.6(a). The reference time-domain data are obtained from HSPICE. Those for the frequency domain are from the Fourier transform of the transient response reached up to 40 ns. The reference values are plotted as dotted lines in the figure. Very good agreement is observed in both domains. The RMS error for the time-domain data is $4.19\text{x}10^{-6}$, and

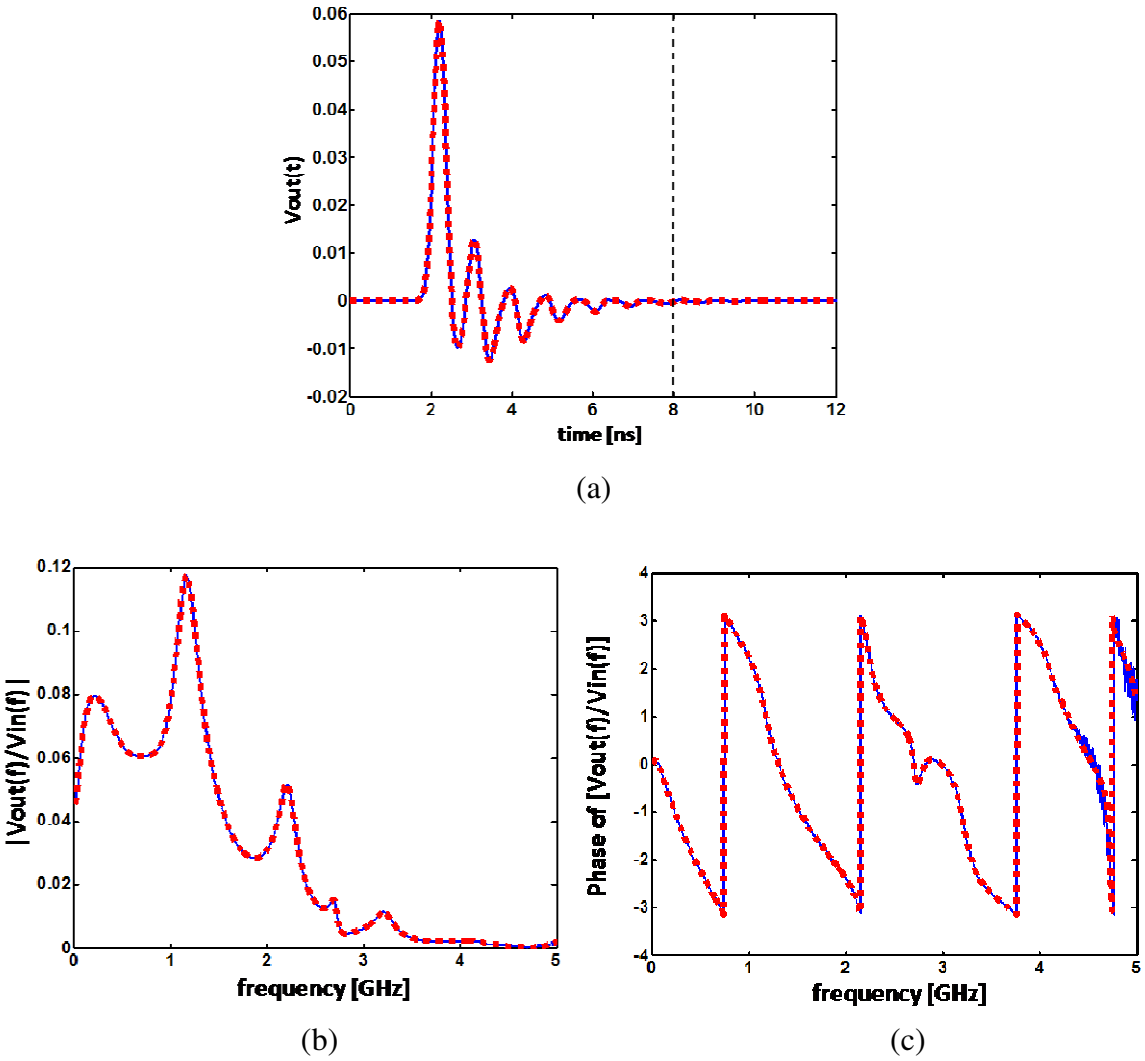



**Figure 3.6** Comparison of reference values and data from the macromodel of TDVF. (a) In the time domain (solid line: HSPICE reference solution; dots: TDVF interpolated/extrapolated response). (b) Magnitude and (c) phase in the frequency domain (solid line: frequency-domain data from Fourier transform; bold dots: frequency-domain data from the TDVF rational approximation).

for the frequency-domain data is $5.65\text{x}10^{-4}$. The observed accuracy demonstrate the effectiveness of the *WT* rule for order estimation.

It is also worth noting that the phase of the reference value is noisy in the high-frequency region while the phase from the macromodel is very smooth even though the shorter time support was used for the TDVF, which means that TDVF provides a reliable means for generating frequency-domain response data reducing the effect of Gibbs phenomenon associated with direct Fourier transformation.

## 3.3 Summary

In this chapter, we introduced the *WT* rule as a robust means for estimating the order of the rational function approximation using TDVF. The *WT* rule was the derivation which, motivated by the 2*WT* theorem, was shown to provide a reliable guideline for selecting the order to be used for accurate rational function approximation given the bandwidth, *W*, of the excitation and the duration, *T*, over which the response needs to be recorded in order to ensure that the output response has been subsided to negligible levels.

# CHAPTER 4
# COMBINED RATIONAL APPROXIMATION FROM FREQUENCY-DOMAIN AND TIME-DOMAIN DATA (CRAFT)

Rational function approximation of EM responses of interconnect structures provides for their convenient and expedient incorporation in commonly used nonlinear circuit simulators, in support of the quantification of interconnect-induced signal degradation and interference. The raw data used for the fitting can be obtained in terms of either finite-transient response recorded over a finite period or through a frequency-domain response over a finite frequency bandwidth. Time-domain modeling is most appropriate for capturing the high-frequency attributes of a device under test (DUT), while the late-time response, associated with the resonant behavior and lower-frequency attributes of the system, comes at the cost of longer simulation times. On the other hand, frequency-domain analysis is computationally most efficient and robust when done over the frequency bandwidth over which the electrical size of the DUT is of the order of the wavelength. However, extracting multiple-tens-of-GHz-frequency response data is cumbersome and expensive.

Hence, the concurrent use of time-domain (TD) and frequency-domain (FD) modeling techniques for the EM modeling of interconnect structures offers the possibility of exploiting their complementary attributes toward achieving an accurate

and very broadband extraction of the response [32]. The advantages of such a hybrid time-frequency characterization have prompted the exploitation of ways in which TD and FD data can be combined toward the synthesis of mathematical models for broadband EM responses.

In this chapter, we present a new methodology for the rational function fitting of broadband EM responses of the DUT utilizing both TD and FD data. The basic idea is to hybridize vector fitting (VF) and time-domain vector fitting (TDVF) into a single algorithm which, through the enrichment of the early-time transient response (rich in high frequencies) of the DUT with low and moderate frequency-domain response data, provides for accurate and broadband rational function fitting of the DUT. The resulting rational fitting algorithm will be referred as CRAFT (Combined Rational Approximation from Frequency-Domain and Time-Domain Data) [30, 31] (see Figure 4.1).

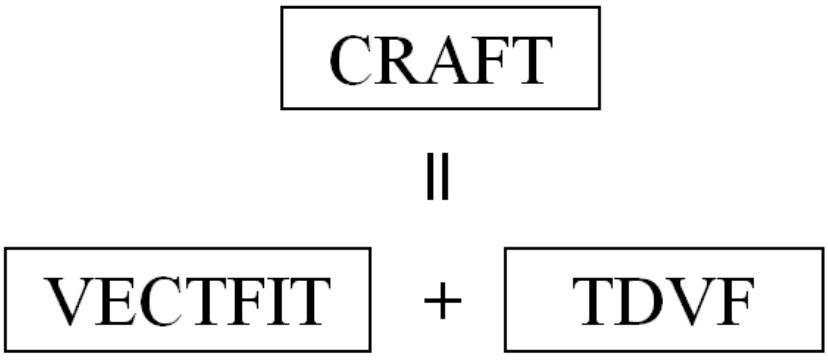



**Figure 4.1** CRAFT is the hybrid method of VF and TDVF.

This hybridization method of TD and FD data, CRAFT was inspired by Sarkar's hybrid extrapolation methods (SHEM) [32, 54-55]. CRAFT and SHEM show similarities in that they construct a wideband macromodel for a DUT using early-time and low-frequency data; however, there are specific differences between CRAFT and SHEM that make a direct comparison of the two rather difficult. To address this issue, the original version of CRAFT presented in [30, 31] has been modified in such a way that a comparison between SHEM and CRAFT is possible.

This chapter is organized as follows. First, the mathematical formulation of CRAFT is presented in Section 4.1, followed by an overview of SHEM and its relation to CRAFT in Section 4.2. In Section 4.3, the modified CRAFT algorithm is briefly introduced, followed by a discussion of data preparation for use of the modified CRAFT in Section 4.4. In Section 4.5, the application of CRAFT to two interconnect systems is considered for validation study purposes. The chapter concludes with a summary of the ideas presented.

## 4.1 Formulation of CRAFT

It is assumed that the DUT is a passive $N_p$ – port system represented by its transfer function matrix, $\boldsymbol{H}(s)$. $M_t$ denotes the recorded time-domain samples of the input and output signals and $M_f$ the number of frequencies at which the transfer function matrix is computed in the frequency domain. The CRAFT algorithm is the hybrid-formulation of VF and TDVF. Because the two fitting algorithms are formulated in a manner of linearized least squares problems as presented in (2.20) and (2.31), we

combine the linear equations of (2.20) from VF and (2.31) from TDVF, into one whole least squares problem using the time-domain data of $x_j(t)$ and $y_{ij}(t)$ and frequency-domain data of $H_{ij}(s)$ as

$$\boldsymbol{A}\cdot\boldsymbol{u}=\boldsymbol{b}$$
$$\boldsymbol{A}=\begin{bmatrix}\boldsymbol{A_f}\\ \boldsymbol{A_t}\end{bmatrix},\quad \boldsymbol{b}=\begin{bmatrix}\boldsymbol{b_f}\\ \boldsymbol{b_t}\end{bmatrix}, \tag{4.1}$$

where $\boldsymbol{u}=\begin{bmatrix} r'_{1,ij} & \cdots & r'_{N,ij} & d'_{ij} & e'_{ij} & \tilde{r}_1 & \cdots & \tilde{r}_N \end{bmatrix}^T$, and $1\le i, j\le N_p$. The overall $\boldsymbol{A}$ matrix is composed of the matrix $\boldsymbol{A_f}$ from VF and the matrix $\boldsymbol{A_t}$ from TDVF. Also, the overall forcing vector $\boldsymbol{b}$ consists of $\boldsymbol{b_f}$ from VF and $\boldsymbol{b_t}$ from TDVF. The unknown vector $\boldsymbol{u}$ consists of the coefficients of rational function approximation.

Equation (4.1) is subsequently used to effect the fitting process described in Chapter 2 for the VF and the TDVF case.

## 4.2 Comparison with Sarkar's Hybrid Extrapolation Methods

CRAFT as a hybridization method that uses time-domain and frequency-domain data was first suggested in Sarkar's hybrid extrapolation method (SHEM) [32, 54, 55]. CRAFT and SHEM are similar in that they are constructing a wideband macromodel for DUT relying upon early-time and low-frequency data.

However, they are basically different. CRAFT uses rational functions for basis, while SHEM uses Laguerre functions, Hermite functions, as well as other orthogonal fuctions [32, 54, 55]. An important advantage of the rational function fitting method,

CRAFT, is that it provides for the direct synthesis of a SPICE-compatible circuit representation from the generated rational function fit.

The difference between SHEM and the CRAFT is not only in the basis functions, but also in the types of inputs used and the types of outputs generated. SHEM uses the early-time response of $y_{ij}(t)$ and the low-frequency data of $Y_{ij}(s)$ to extrapolate those data in late-time and high-frequency regions. Actually SHEM constructs the macromodel of $Y_{ij}(s)$, which is the product of $X_j(s)$ and $H_{ij}(s)$. In contrast, CRAFT uses $x_j(t)$ and $y_{ij}(t)$ for early-time data and $H_{ij}(s)$ for the low frequency data to generate a macromodel of $H_{ij}(s)$ that is valid over the broad frequency bandwidth. From the generated fit of $H_{ij}(s)$, late-time data of $y_{ij}(t)$ can be subsequently generated and also the system output for arbitrary inputs can be obtained via a recursive convolution process. The direct macromodeling of $H_{ij}(s)$ is another advantage of CRAFT over SHEM. In Figure 4.2, differences between the inputs and outputs used by the two methods are summarized in visual form

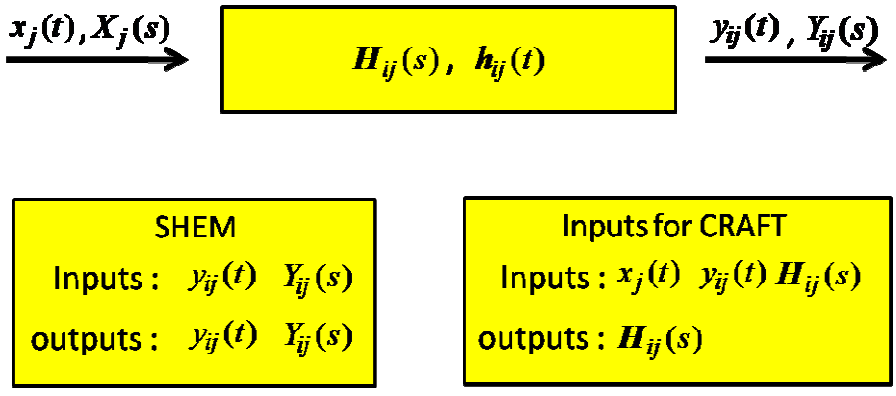



**Figure 4.2** Input and output configurations.

In view of the aforementioned differences, in order to clearly compare CRAFT with SHEM, a modified CRAFT method will be presented that extrapolates $y_{ij}(t)$ to later time and $Y_{ij}(s)$ to higher frequency as driven by SHEM.

## 4.3 The Modified CRAFT

To compare the performance of a hybrid rational function fitting method of CRAFT with SHEM, we modify CRAFT to extrapolate a system's early-time response, $y_{ij}(t)$, to later times and low-frequency domain data, $Y_{ij}(s)$, to higher frequencies. This modification means a change of the $x_j(t)/y_{ij}(t)/H_{ij}(s)$ framework of the original CRAFT to the $y_{ij}(t)/Y_{ij}(s)$ framework used in SHEM.

The framework change in the frequency domain is realized by replacing $H_{ij}(s)$ with $Y_{ij}(s)$ for the VF part in (2.19) as

$$\left(\sum_{n=1}^{N}\frac{r'_{n,ij}}{s-\tilde{q}_n}+d'_{ij}+se'_{ij}\right)-\left(\sum_{n=1}^{N}\frac{\tilde{r}_n}{s-\tilde{q}_n}\right)\cdot\{\boldsymbol{Y}(s)\}_{ij}=\{\boldsymbol{Y}(s)\}_{ij}, \tag{4.2}$$

where $Y_{ij}(s)=X_j(s)\cdot H_{ij}(s)$. For the time-domain formulation, we take the inverse Laplace transform of both sides of (4.2) except for the first order term of $s$ in the left side:

$$\left(\sum_{n=1}^{N}r'_{n,ij}e^{\tilde{q}_n t}+d'_{ij}\right)*\delta_j(t)-\left(\sum_{n=1}^{N}\tilde{r}_n e^{\tilde{q}_n t}\right)*y_{ij}(t)=y_{ij}(t), \tag{4.3}$$

where $*$ represents the convolution operator which is numerically calculated using the recursive convolution as presented in Chapter 2, and $\delta_j(t)$ is an impulse function. For the numerical implementation, the impulse function is evaluated as

$$\begin{aligned} \delta_j(t) &= 0 && \text{when} \quad t \neq 0, \\ \delta_j(t) &= 1/(\Delta t) && \text{when} \quad t = 0, \end{aligned} \tag{4.4}$$

where $\Delta t$ is the sampling time.

The formulation of the modified CRAFT is completed via (4.2) and (4.3) in the manner of a least squares problem using the early-time data of $y_{ij}(t)$ and the low-frequency data of $Y_{ij}(s)$ to extrapolate them in late-time and high-frequency regions, respectively.

## 4.4 Data Preparation

CRAFT is the hybridization of TDVF and VF. Hence, we excite the system with a Gaussian pulse as we did for the TDVF, utilizing the attributes of the Gaussian pulse that provide an effective way to set the frequency bandwidth of the response to an upper frequency limit. More specifically we use a Gaussian pulse with 60 dB bandwidth at $f = W$ for excitation input $x_j(t)$ as presented in Chapter 2.

$$x_j(t) = \frac{1}{\alpha\sqrt{\pi}} U_0 e^{-\left(\frac{t-t_0}{\alpha}\right)^2} \tag{4.5}$$

where $\alpha$ determines the frequency bandwidth, while the turn-on delay, $t_0$, is used to make $x_j(t) \approx 0$ for $t < 0$. In the frequency domain, the pulse spectrum is

$$X_j(f) = e^{-[(\pi f \alpha)^2 + j2\pi f t_0]}. \tag{4.6}$$

In order to set a duration for the early-time response, $y_{ij}(t)$ is truncated at time $T_E$, according to the condition

$$\frac{|\, y_{ij}(t)\,|}{\max(|\, y_{ij}(t)\,|)} < 0.1 \qquad \text{for} \quad t > (T_E + t_0). \tag{4.7}$$

To facilitate the use of the modified CRAFT, it is desirable to have in place guidelines for the estimation of the order *N* of the rational function fit to be generated. Following the line of thinking in Chapter 3, we would like to use the *WT* rule to provide an estimate for the order *N* as $N \approx WT$. With *W* defined in terms of the bandwidth of the Gaussian pulse used for the excitation, all that remains is the determination of *T*. For this purpose, the following approach is used. Through an inverse Fourier transform of the low-frequency data of $Y_{ij}(s)$, a time-domain response $\tilde{y}_{ij}(t)$ is obtained. This response is used for the determination of *T* through (3.1). It should be noted that the value of *T* obtained from the low-frequency data though (3.1) is rather smaller than the actual time support of the low-frequency data.

## 4.5 Validation Studies

In this section, two interconnect systems are considered to demonstrate the performance of CRAFT, the modified CRAFT, and the validity of the *WT* rule for order estimation.

### 4.5.1 A four-port interconnect system

The first study concerns the four-port interconnect system characterized in terms of S-parameter data up to 10 GHz described in Chapter 3. The $S_{11}$ was chosen as a

representative element in the 4 x 4 scattering matrix of the interconnect system. The characteristic impedance used for the definition of the scattering matrix was 50 Ω.

The time-domain and frequency-domain data used for the CRAFT fitting were obtained by analyzing the circuit with 50 Ω terminations in HSPICE. All the ports except Port 1 were terminated with 50 Ω, and Port 1 was connected to a source that had a source resistor of 50 Ω for obtaining the time-domain data for the scattering parameters.

For time-domain data, the Gaussian pulse with 60 dB bandwidth at 10 GHz of the same parameters as in (2.33) ($U_0 = 1$, $\alpha = 8.336\text{x}10^{-11}$ and the turn-on delay $t_0 = 0.6\,\text{ns}$), was assigned to the source. The pulse was sampled with the time step $\Delta t = 5\,\text{ps}$, and the reflected voltage wave at port 1, $y_{11}(t)$, was recorded over the interval $0 \le t \le 6$ ns, with sampling time step $\Delta t = 25\,\text{ps}$.

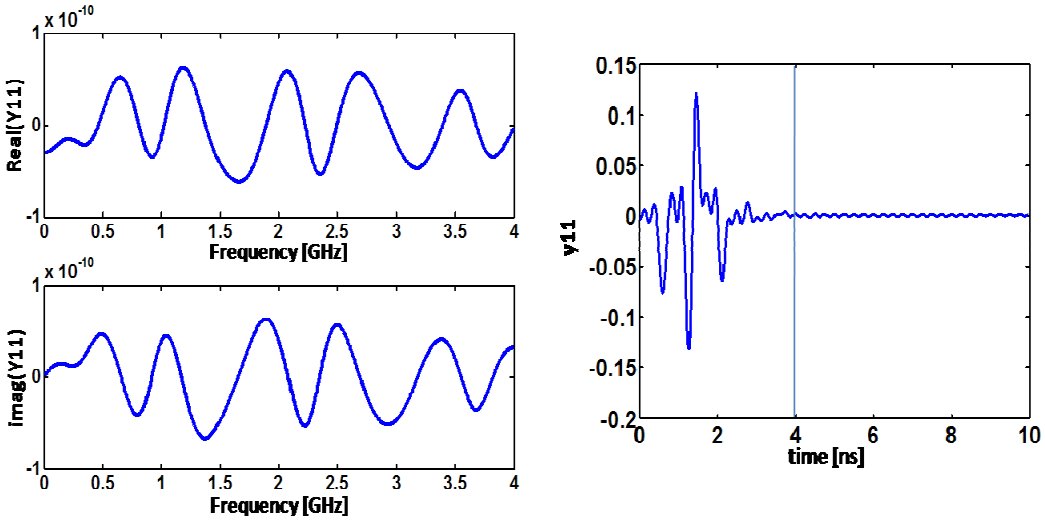
The frequency data were collected through a linear AC sweep from 1 Hz to 10 GHz. A total of 250 frequency-domain data were linearly collected with the sampling frequency step $\Delta f = 40.04$ MHz. These time-domain and frequency-domain data were used both for the selection of the subset of data points used for the fitting and also for the reference values for testing the accuracy of the generated fit. In this study, the RMS error in the time domain is computed as the relative value to the peak value of the Gaussian pulse input to present the accuracy clearly.

The frequency-domain data, $S_{11}(s = j2\pi f)$ over $0 \le f \le 4$ GHz were used as the low-frequency data and are depicted in Figure 4.3(a). This amounted to $M_f = 100$,

frequency-domain data samples. Regarding the time-domain data, $y_{11}(t)$ over the time interval $0 \le t \le 2.475$ ns was used for the fitting and is depicted in Figure 4.4. This amounted to $M_t = 100$ samples.

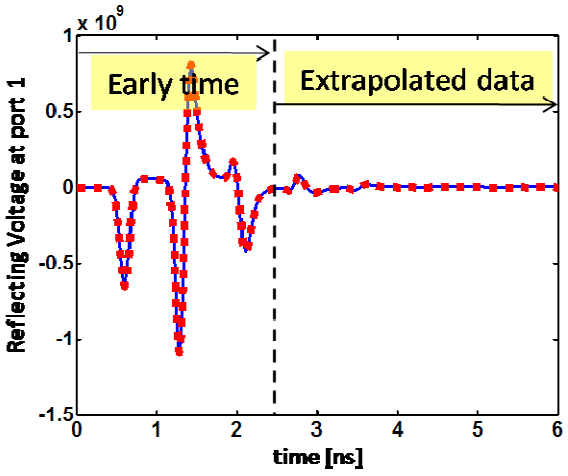
For order estimation for CRAFT, $T$ was estimated using the low-frequency data of $S_{11}$. The low-frequency data of $Y_{11}$ $(= X(s) \cdot S_{11}(s))$ were inverse Fourier transformed to the TD data as shown in Figure 4.3(b). $T$ was estimated at 3.4 ns. The order was set to be 60, a value larger than the $TW = 34$ value suggested by the *WT* rule.

The CRAFT with the order $N = 60$ using the early-time and the low-frequency data, generated the rational function fit of $S_{11}(s)$. From the generated rational function fit, we could obtain the reflected wave at port 1, $y_{11}(t)$ for the Gaussian input of $x_1(t)$ via recursive convolution. The time-domain and frequency-domain data from the constructed macromodel of $S_{11}$ are presented as dotted lines in Figure 4.4 and are compared with reference values.

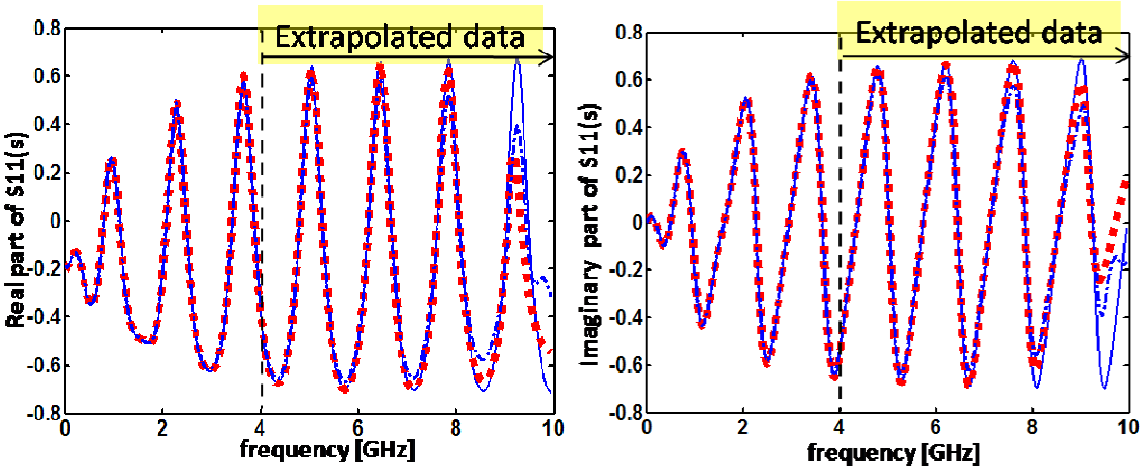



(a) (b)

**Figure 4.3** (a) Low-frequency data and (b) estimated late-time response from the Fourier transform of the low-frequency data.




(a)




(b) (c)

**Figure 4.4** Comparison of reference values and data from the macromodel of CRAFT. (a) In the time domain (solid line: HSPICE reference solution; dots: CRAFT interpolated/extrapolated response). (b) Magnitude and (c) phase in the frequency domain (solid line: FD data from HSPICE; dash and dot: data from Fourier transform; dots: data from CRAFT).

More specifically, in Figure 4.4(a), the time-domain data of $y_{11}(t)$ obtained from the generated macromodel are compared with the reference values. Very good agreement is observed over both the early-time interval and the extrapolated, late-time response. The RMS error in the time domain was $1.6819\text{x}10^{-4}$, indicating a very accurate fit.

The frequency-domain data are plotted in Figures 4.4(b) and (c). The macromodel shows good agreement with reference values in the low-frequency region of interpolation, and acceptable accuracy in the lower-frequency portion of the extrapolated higher-frequency range. However, at high frequencies the discrepancy is significant, indicating unacceptable accuracy of the fit at the highest frequencies.

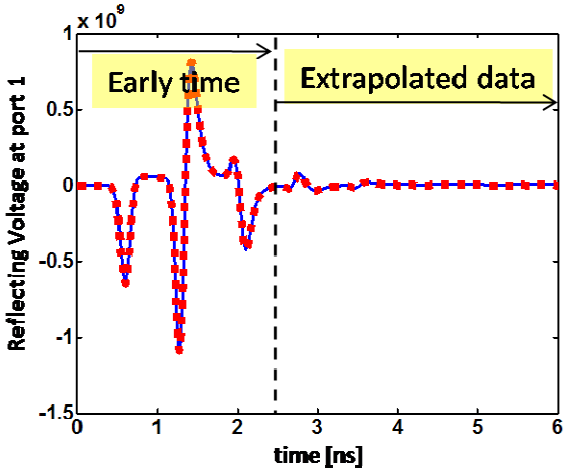
The inaccuracy in the high-frequency region may be attributed to the lower sampling rate involved in aliasing, which is plainly observed from the Fourier transformed data in Figure 4.4 (b) and (c). Another reason for the inaccuracy of the macromodel may be the limitation of CRAFT fitting the transfer function $S_{11}(s)$, which is not band-limited, instead of macromodeling the Gaussian windowed transfer function $Y_{11}(s)$.

In order to examine these two possible sources of error, we are going to repeat the testing of the performance of CRAFT in two ways. One is to increase the sampling rate of the TD data and construct the macromodel via CRAFT. The other one is to construct the macromodel using the modified CRAFT without increasing the sampling rate.

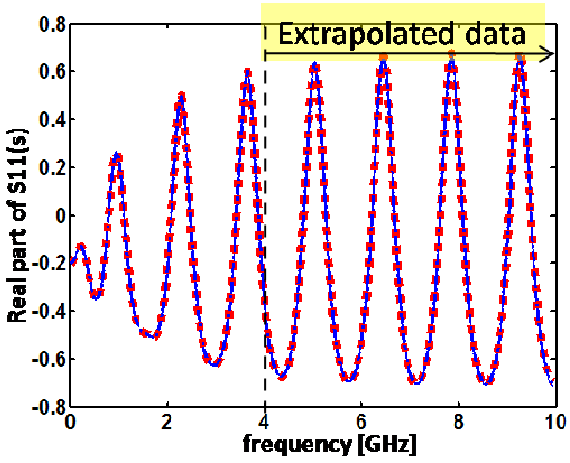
First, we decreased the sampling time to $\Delta t = 5$ ps and used the same time support of the time-domain data $(M_t = 500)$ and the frequency-domain data $(M_f = 100)$ sets. The result is presented in Figure 4.5.

In Figure 4.5, the data from the macromodel of CRAFT show excellent agreement with reference values in both the time domain and the frequency domain over the entire domains of interpolation and extrapolation. The difference is negligible. The RMS error in the time domain was $6.0311 \text{x} 10^{-5}$. Similarly, the one in the frequency domain was 0.0092, where the frequency-domain data from the macromodel are compared with data obtained from the Fourier transformation of the time-domain data over the interval $0 \le t \le 14.995$ ns. The accuracy of the frequency-domain data is greatly enhanced with the increased sampling rate of the time-domain data. We can distinctly observe the accuracy in the high-frequency region of extrapolation, which implies that the CRAFT can construct the broadband macromodel accurately when both the early-time response and the low-frequency data characterize the system completely in a complementary manner.

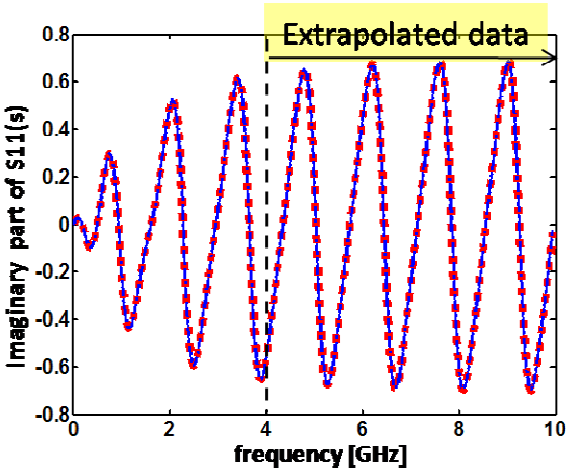
Next, the performance of the modified CRAFT is considered. The time-domain and the frequency-domain data sets in the first study of CRAFT were used, where the sampling time step was $\Delta t = 25$ ps and the order of the fit was $N = 60$. The only difference was that the early-time interval was extended to 3 ns and thus, the number of time samples was $M_t = 120$.




(a)




(b)




(c)

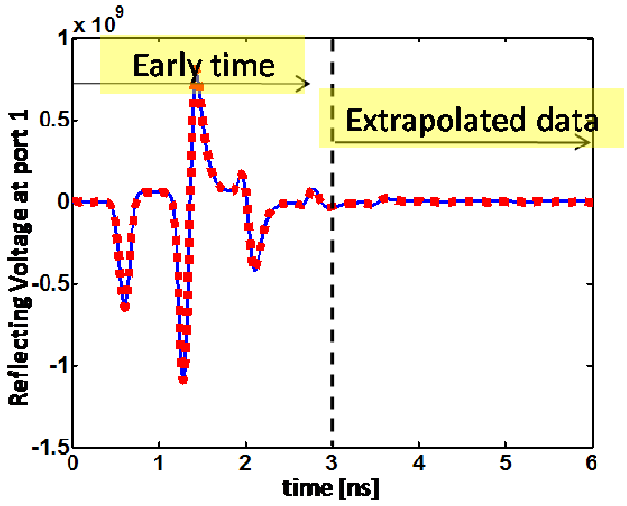
**Figure 4.5** Comparison of reference values from HSPICE and data from the macromodel of CRAFT. (a) In the time domain (solid line: HSPICE reference solution; dots: CRAFT interpolated/extrapolated response). (b) Magnitude and (c) phase in the frequency domain (solid line: FD ata from HSPICE; dash and dot: data from Fourier transform; dots: data from the CRAFT).

Figure 4.6 shows the fitting result of the modified CRAFT in both time domain and frequency domain. The result shows very good agreement with the reference values from HSPICE. The RMS error in the time domain was $2.2145\text{x}10^{-4}$ and the RMS error in the frequency domain was 0.0026. As in [54], to evaluate the performance of the extrapolation, the normalized mean-squared errors (MSEs) in time domain and frequency domain are computed as

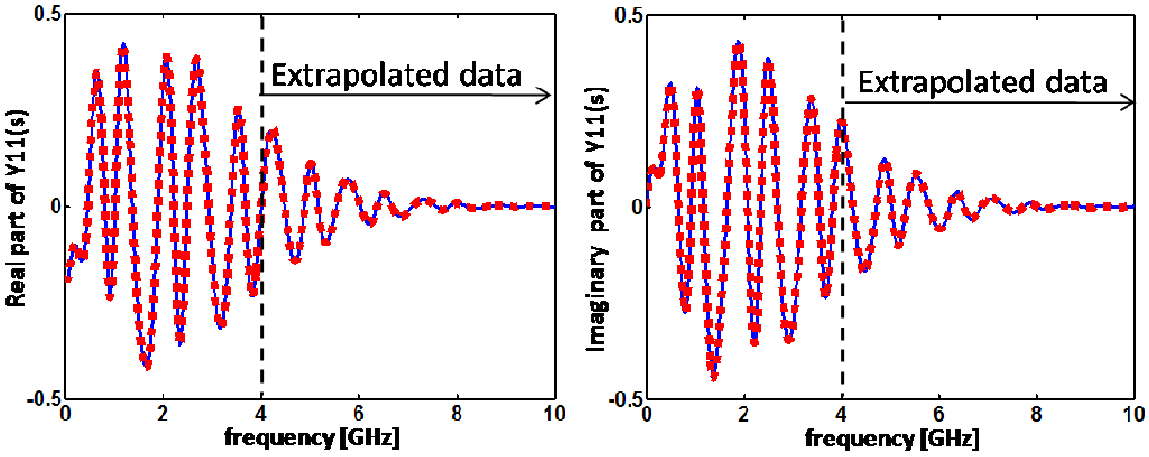
$$E_t = \frac{\| \hat{\boldsymbol{y}}_{11} - \boldsymbol{y}_{11} \|_2}{\| \boldsymbol{y}_{11} \|_2}, \quad E_f = \frac{\| \hat{\boldsymbol{Y}}_{11} - \boldsymbol{Y}_{11} \|_2}{\| \boldsymbol{Y}_{11} \|_2} \tag{4.8}$$

where $\| \bullet \|_2$ is the $L^2$-norm of a vector, and $\hat{\boldsymbol{y}}_{11}$ and $\hat{\boldsymbol{Y}}_{11}$ are the vectors of extrapolated data in the time domain and the frequency domain while $\boldsymbol{y}_{11}$ and $\boldsymbol{Y}_{11}$ are the vectors of reference values in the time-domain and frequency-domain extrapolation regions. In this validation test, $E_t$ was 0.1345 and $E_f$ was 0.0080, demonstrating the accuracy of the modified CRAFT.

However, when the Gaussian window $X_1$ was extracted from the macromodel $Y_{11}$ to compute the scattering parameter $S_{11}$, the computed data of $S_{11}$ were quite different from reference values in the high-frequency region as depicted in Figure 4.7. The RMS error in the frequency domain was 0.2636, which implies that the macromodel of $Y_{11}$ shown in $E_f$ cannot guarantee accuracy in the calculation of $S_{11}$, and the performance of the modified CRAFT is also limited by the quality of the time-domain and frequency-domain data. The time-domain and frequency-domain data should complementarily represent the whole set of characteristics of a broadband system.

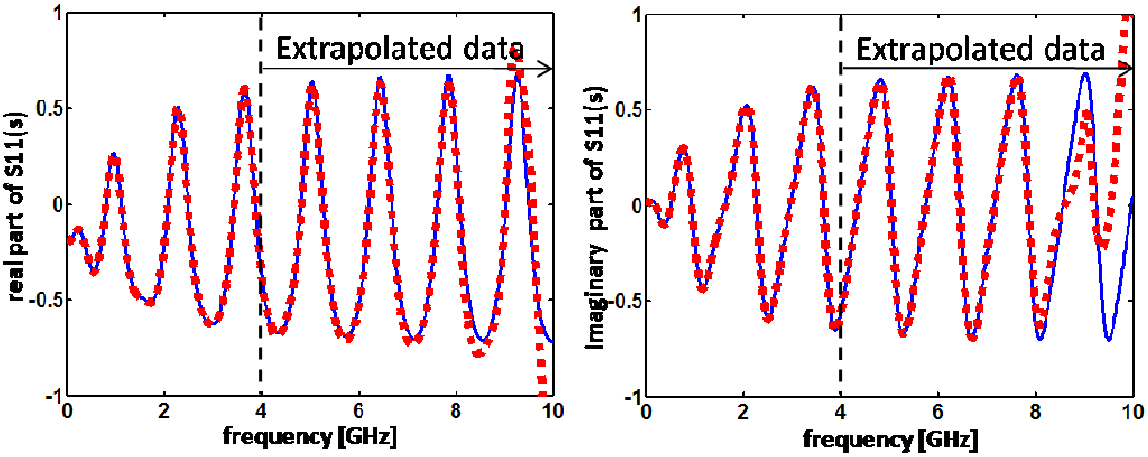



(a)




(b) (c)

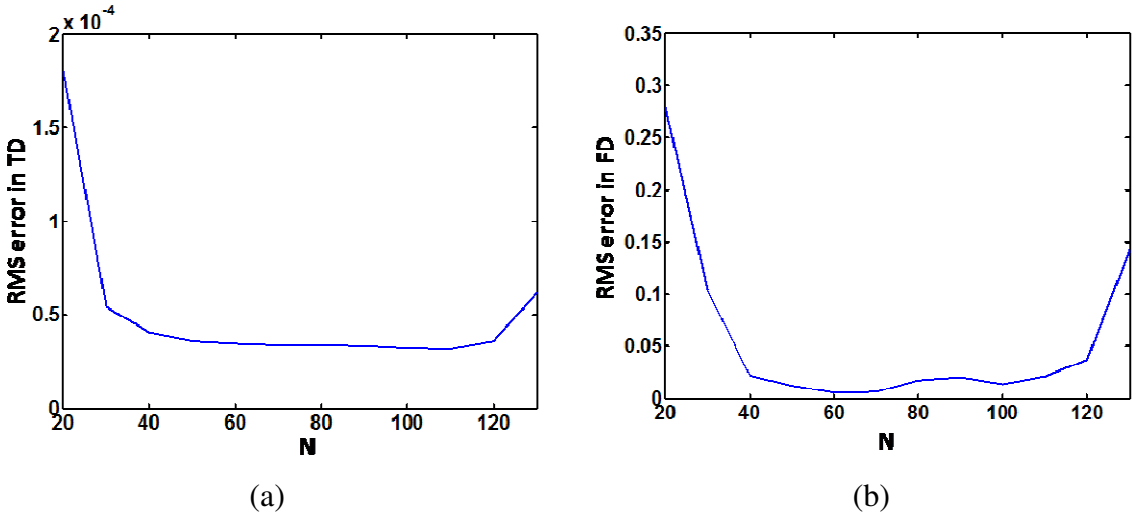
**Figure 4.6** Comparison of reference values from HSPICE and data from the macromodel of the modified CRAFT. (a) In the time domain (solid line: HSPICE reference solution; dots: modified CRAFT interpolated/extrapolated response). (b) Magnitude and (c) phase in the frequency domain (solid line: from HSPICE; dots: from the modified CRAFT).




(a) (b)

**Figure 4.7** Comparison of reference values from HSPICE and data from the macromodel of the modified CRAFT after the Gaussian window extraction. (a) Magnitude and (b) phase of $S_{11}$ in the frequency domain (solid line: from HSPICE; dots: from the modified CRAFT after the window extraction).

To examine the usefulness of the guideline for the estimation of the order of the rational function fit generated by CRAFT, we calculated the RMS error of the fit for different values of *N*. The sampling time $\Delta t$ was 5 ps and the same time support of the time-domain data ($M_t = 500$) and the frequency-domain data ($M_f = 100$) were used. Because $T$ was estimated to be 3.4 ns and $W$ = 10 GHz, we expect the lower limit of the order to be 34. The values of RMS error depending on the order *N* are plotted in Figure 4.8. As the order *N* increases, the RMS error decreases, reaching a minimum around $N = TW = 34$, and it starts to diverge around 120 for both time domain and frequency domain. We attribute this to numerical error on the solution of the least squares problem used for the generation of the rational function fit. We conclude that




(a) (b)

**Figure 4.8** RMS error depending on the order $N$ (a) in the time domain and (b) in the frequency domain.

the *WT* rule provides a reliable and useful means for estimating the order of the rational function fit.

### 4.5.2 A terminated coaxial cable

The second example considered was a terminated air-filled coaxial cable, which was studied in [57]. The cable is 1 m long with inner radius 4 mm and outer radius 8 mm, and terminated at the near end by a current source with a 5 Ω resistor in parallel and at the far end by a lumped circuit composed of a 100 pF capacitor in series with the parallel combination of a 10 nH inductor and another 5 Ω resistor. The current excitation input was taken to be

$$x_1(t) = \exp(-(t-t_0)^2 / t_w^2)\ \cos(2\pi f_0 (t-t_0)), \tag{4.9}$$

where $f_0 = 0.3\,\text{GHz}$, $t_0 = 5.0 / f_0$, and $t_w = 1.0 / f_0$. The current pulse $x_1(t)$ was sampled at every $\Delta t = 0.02\,\text{ns}$. The output voltage at the port 1, $y_{11}(t)$, was the measured output quantity.

The time-domain data of $y_{11}(t)$ was recorded over the interval $0 \le t \le 70$ ns. The frequency-domain data over the interval $2 \le f \le 500$ MHz were computed with a sampling of $\Delta f = 2$ MHz via TDVF using the time-domain data over the interval $0 \le t \le 59.98\,\text{ns}$ ($N = 22, M_t = 3000$). These time-domain and frequency-domain data were used both for the selection of the subset of data points used for the fitting and also for providing the reference solution for testing the accuracy of the generated fit.

Regarding the input for CRAFT, the time-domain data over $0 \le t \le 27.98$ ns ($M_t = 1400$) and the frequency-domain data over $2 \le f \le 280$ MHz ($M_f = 140$) were used for CRAFT with an order of $N = 22$. The fitting results are presented in Figure 4.9. The interpolated/extrapolated data in both time domain and frequency domain show very good agreement with the reference values. The RMS error in the time domain was $8.1671\text{x}10^{5}$ (relative value to the maximum of $y_{11}(t)$ was $1.3513\text{x}10^{-5}$) and that in the frequency domain was 0.0011. Even though the shape of $x_1(t)$ was different from the Gaussian pulse presented before, the CRAFT constructed the macromodel very accurately.

## 4.6 Summary

In summary, we have introduced a new methodology for constructing the broadband rational function approximation using early-time response data and low-

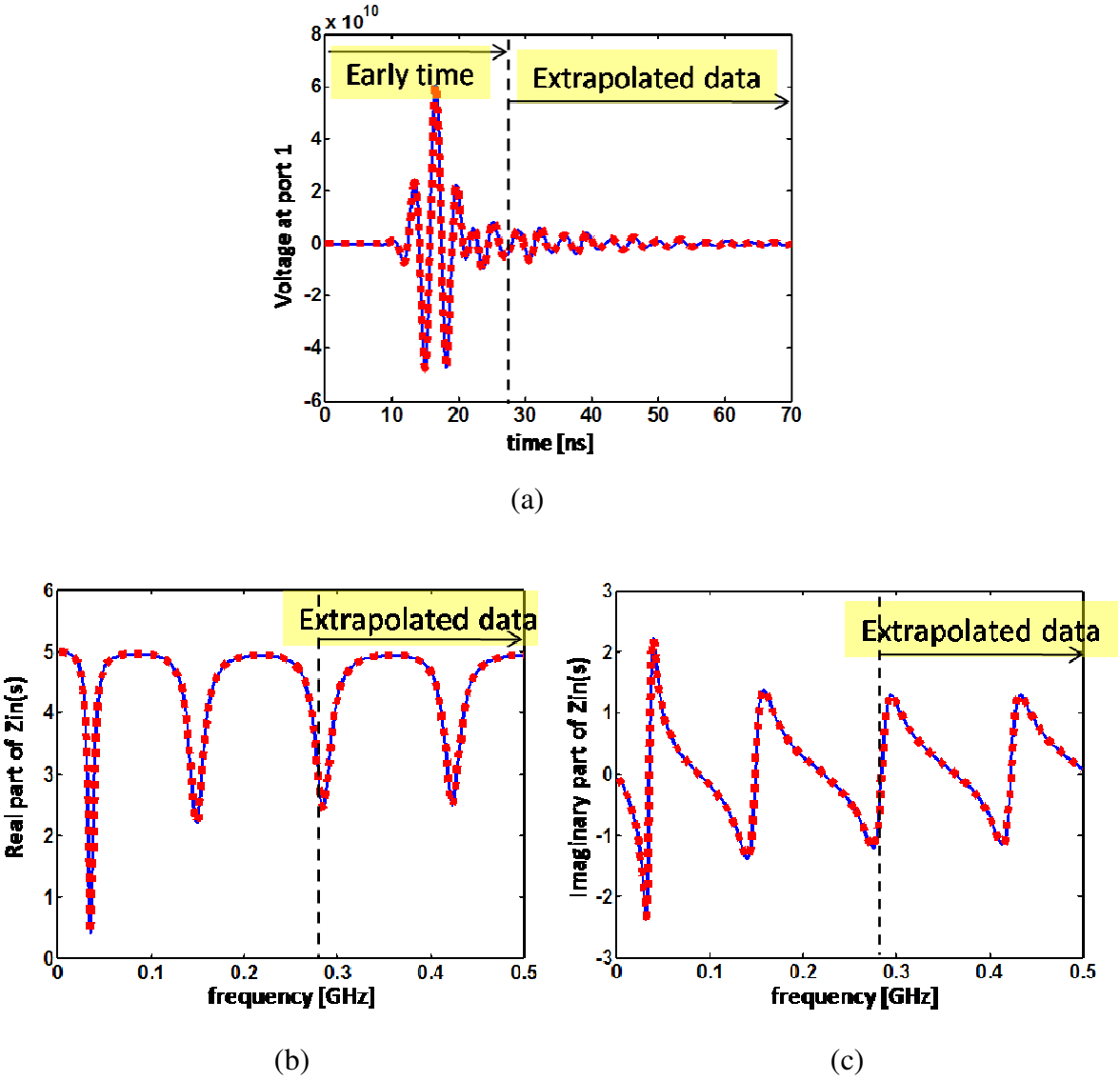



**Figure 4.9** Comparison of reference values and data from the macromodel of the CRAFT. (a) In the time domain (solid line: reference solution; dots: CRAFT interpolated/extrapolated response). (b) Magnitude and (c) phase in the frequency domain (solid line: from the TDVF; dots: from the CRAFT).

frequency data in a complementary and concurrent manner. The proposed fitting methodology, CRAFT, is the hybridization of the frequency-domain rational fitting process, VF, and its time-domain counterpart, TDVF.

The validity and accuracy of the method have been demonstrated through its application in the fitting of a four-port MIMO (multi-input multi-output) interconnect circuit, and a terminated coaxial cable. The modified CRAFT was demonstrated to extrapolate the time-domain and frequency-domain data successfully like Sarkar's extrapolation methods, and the *WT* rule which was discussed in Chapter 2 was also successfully applied to the order estimation of CRAFT.

# CHAPTER 5
# DELAYED RATIONAL FUNCTION APPROXIMATION

Recent advances in modeling high-speed interconnects have demonstrated the benefits of extracting the transport delay from the frequency data prior to generating the rational function fit. The delay extraction reduces the order of the rational function fit, enhances the accuracy, and preserves the causality of a device under test (DUT).

There are three essentially different approaches to macromodeling with delay extraction. The first approach is based on the method of characteristics (MoC) [7], the second is based on the matrix rational function approximation (MRA) [8], and the third is based on the transfer function approximation [30, 31]. Unlike other approaches that have only been applied to single or coupled transmission lines with p.u.l parameters, the third approach, the transfer function approximation approach, can be applied to large portions of interconnects that have discontinuities and multiple cascaded transmission lines. Furthermore, the third approach can be applied to an arbitrary system that has frequency data representing the relation between input and output.

In our approach, we employ the third approach to macromodel the S parameter (instead of the Y or the Z parameter) using the vector fitting (VF) after delay extraction; VF is done element by element, which results in a different set of poles for each element of the S parameter matrix.

There are several reasons why the S parameter, instead of the Y or the Z parameter, is used for macromodeling the high-speed interconnects. In measurement, it is very inconvenient and tedious to terminate a circuit with short/open in the microwave region for the Y/ Z parameters. In contrast, the S parameter is very easily measured from a device embedded in properly selected termination. Furthermore, high-frequency characterization equipment such as the vector network analyzer (VNA) is elaborately developed to measure directly S parameters from as low as 300 kHz to greater than 100 GHz. In theory, S parameters are defined using traveling waves; hence, transport delay can be readily extracted from S parameters representing transfer functions, and then the S parameters are fitted as the product of a rational function and the transcendental function $exp(-Ts)$, where $T$ is the transport delay. Consequently the macromodeling based on the S parameters requires relatively smaller order for the rational approximation. When the S parameters are computed or measured, a device under test (DUT) is terminated with resistors, thereby suppressing reflections at ports. For the Y/Z parameters, however, all the ports are short/open-circuited, and internal reflections arise at the ports. Hence, more peaks appear in the frequency responses due to the internal reflections, and a higher order is demanded for macromodeling. For these reasons, our proposed method is based on S parameters.

This chapter is organized as follows to present the delayed rational function approximation of the S parameters for a distributed system modeling method toward causality preservation, order reduction and accuracy enhancement. First, causality preservation in the modeling process via delay extraction will be discussed in Section

5.1, and the procedure of the delayed rational function approximation will be presented next. In Section 5.3, the amount of order reduction is derived from the consideration of lossless transmission lines, and in Section 5.4 the computation of the delay and the optimization procedure of the delayed rational function fitting are stated. Then the limitation of the fitting method will be discussed, and validation studies will follow. In the last section, we will conclude with a summary.

## 5.1 Causality and Delay Extraction

Causality becomes more demanding in high-speed interconnects because the delays are not negligible in distributed circuits and causality must be preserved to obtain the correct signaling in time. Causality must also be preserved to guarantee the passivity of the system.

The rational function approximation is commonly used for modeling the distributed system, but it cannot model the causality of the DUT correctly. Delays are embedded in the data as exponential forms, and make the order of rational function fit infinite. Therefore, a rational function fit with a finite order cannot show delays correctly, and violates the causality [28].

Therefore, we suggest that the delay extraction be considered as preprocessing of the rational function approximation. With the delay extraction, it is possible to obtain accurate time-domain responses and preserve causality even with the reduced order of rational function fit [28, 61].

## 5.2 Rational Function Approximation with Delay Extraction

It is assumed that the DUT is a passive $N_P$-port system; hence, its network representation is in terms of an $N_P \times N_P$ S parameter matrix, $\boldsymbol{S}(s)$. We are interested in the development of the macromodel of a delayed rational fit for each one of the elements of the S-parameter matrix as

$$\{\boldsymbol{S}(s)\}_{ij} \cong e^{-jt_{ij}s}\left(D_{ij}+\sum_{m=1}^{N_{ij}}\frac{R_{m,ij}}{s-p_{m,ij}}\right). \tag{5.1}$$

In the above equation, $N_{ij}$ is the order of the rational fit, and $D_{ij}$, $p_{m,ij}$, and $R_{m,ij}$ are constants obtained through the rational fit following the extraction of the time constant $t_{ij}$, which is recognized as the transport delay between port *i* and port *j*, and $i, j = 1,2,...,N_P$.

For simplicity, a SISO system is considered and Equation (5.1) is written as

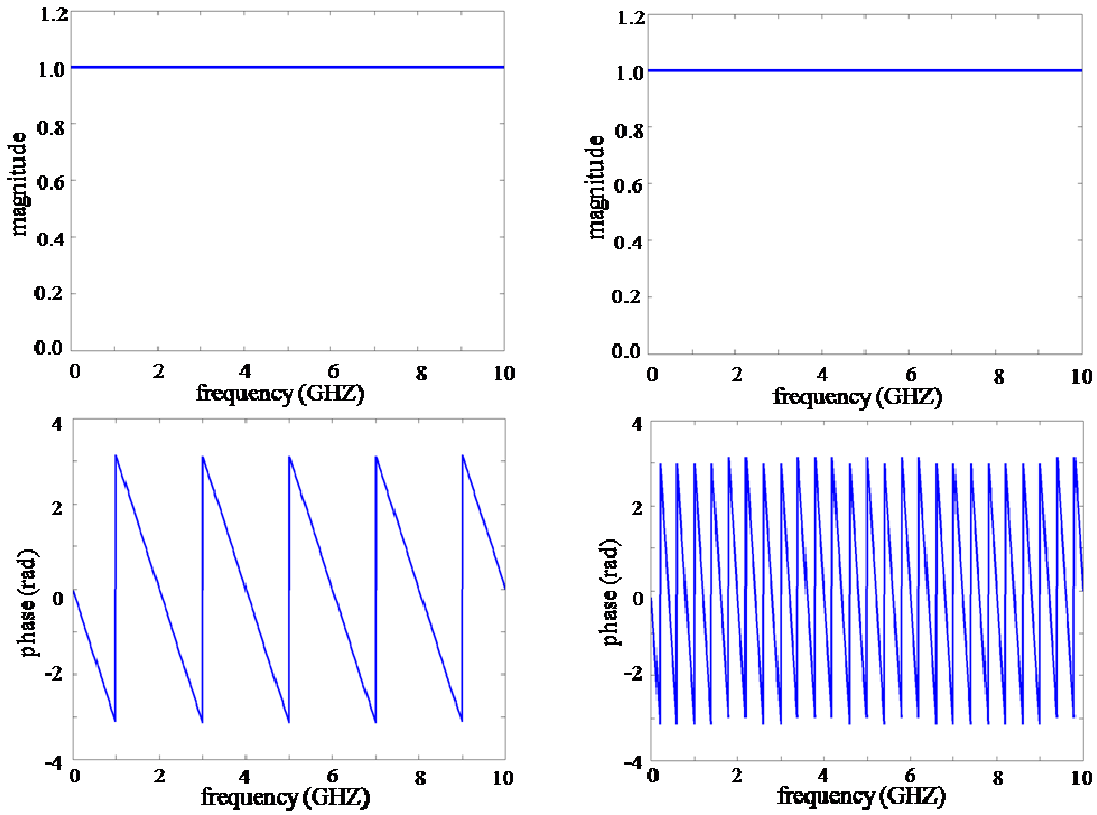
$$H(s)=e^{jt_d s}S(s)\cong D+\sum_{m=1}^{N}\frac{R_m}{s-p_m} \tag{5.2}$$

where the subscripts *ij* are dropped, and $t_{ij}$ is replaced by $t_d$. $H(s)$ is the rational function part in the delayed rational fit of $S(s)$. $H(s)$ is obtained by multiplying $S(s)$ by the transcendental function of the delay, as shown in (5.2), which presents delay extraction. The modified frequency-domain data of $e^{jt_d s}S(s)$ are put into VF, which was described before, and the rational function approximation $H(s)$ can be obtained.

## 5.3 Rational Function Order Reduction Due to Delay Extraction

In the context of delayed rational fits, the delay term is represented by $e^{-jt_d s}$, which is the transfer scattering parameter of a lossless transmission line (TL) when that is terminated with its characteristic impedance. So we are going to macromodel a lossless TL for examining the benefits of delay extraction and the order reduction.

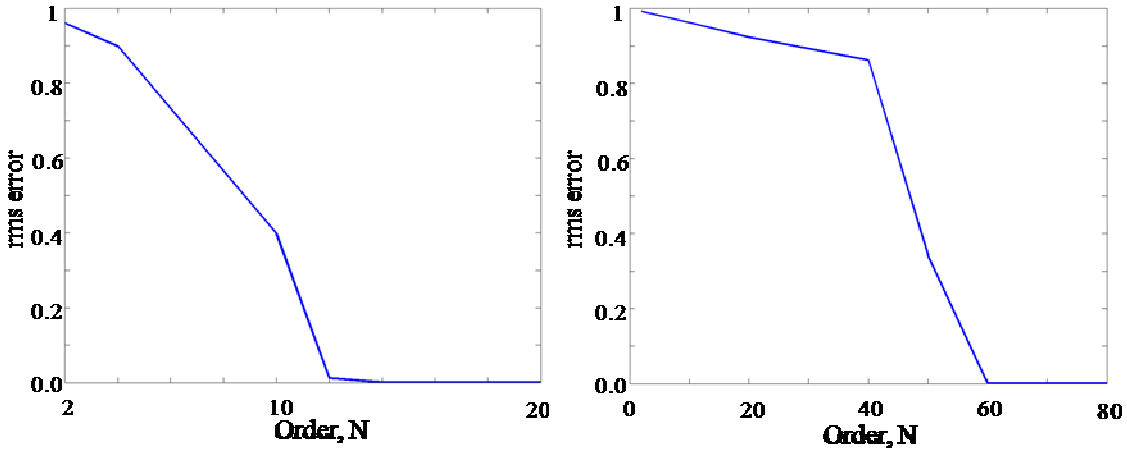
Two lossless TLs with $L = 2.5$ nH/cm, $C = 1$ pF/cm and different lengths, $l$ = 10 cm and 50 cm are considered. Figure 5.1 depicts the transfer scattering parameter for each case. The magnitude is constant value '1' and only the phase is changing.




(a) (b)

**Figure 5.1** Magnitude and phase of $S_{21}$ for lossless TL of (a) 10 cm and (b) 50 cm length.

The frequency data are linearly sampled at 1000 points from 10 MHz to 10 GHz and the transport delay between two ports was computed by dividing the length by its phase velocity: 0.5 ns for the TL of 10 cm and 2.5 ns for that of 50 cm. The frequency data were put into the VF process without delay extraction. The RMS error of the generated fit is plotted in Figure 5.2.




(a) (b)

**Figure 5.2** RMS error depending on the order *N* of the rational function approximation without delay extraction for lossless TL (a) 10 cm and (b) 50 cm long.

When 1% RMS error is admitted, the minimum value of the order *N* is 14 for 10 cm TL and 54 for 50 cm TL. In [22], *N* was determined to be about twice the number of peaks in the magnitude of the function, which is not applicable to a delayed system. Even though the magnitude $S_{21}$ of a lossless is constant, rational function approximation requires *N* more than 2. The minimum *N* is about twice the number of $2\pi$ phase shifts in the phase plot. Hence, not only peaks in magnitude but also $2\pi$ phase shifts should be counted for order determination.

When delay was extracted prior to rational function approximation, the RMS error of the delayed rational function approximation with $N = 2$ was 4.8941 x $10^{-16}$ for the 10 cm TL, and was 1.1384 x $10^{-15}$ for the 50 cm TL. The RMS error decreased significantly with the considerably reduced order $N$. This result demonstrates order reduction and accuracy enhancement resulting from delay extraction.

Next, we examine how much the transport delay term $e^{-jt_d s}$ contributes to increase the order $N$ of a rational function fit in the frequency range of $[0, f_{\max}]$, which is the amount of order reduction caused by delay extraction. Figure 5.3 depicts the phase of $e^{-jt_d s}$ depending on the frequency. From Figure 5.3,

$$\frac{2N_{\max}+1}{2t_d} \le f_{\max} < \frac{2N_{\max}+3}{2t_d} \tag{5.3}$$

where $N_{\max}$ is the number of the $2\pi$ phase shifts. When $N_d$ is the order increment due to the delay,

$$N_d \sim 2N_{\max} \sim 2 f_{\max} t_d , \tag{5.4}$$

based on the observation that a $2\pi$ phase shift counts about 2 for the order of rational function fit for modeling lossless TL lines.

The approximation in (5.4) states that $N_d$, which is the amount of order reduction after delay extraction, is proportional to the maximum frequency of interest, $f_{\max}$, and the transport delay $t_d$. This estimation is supported by the lossless TL study above. For the 10 cm TL, this estimate is supported by the lossless TL studies above. For the

10 cm TL, $f_{\max} t_d$ and $N_{\max}$ were 5; $N_d$ was 12, which is about $2N_{\max}$. For 50 cm TL, $f_{\max} t_d$ and $N_{\max}$ were 25; $N_d$ was 54, which is about $2N_{\max}$ also.

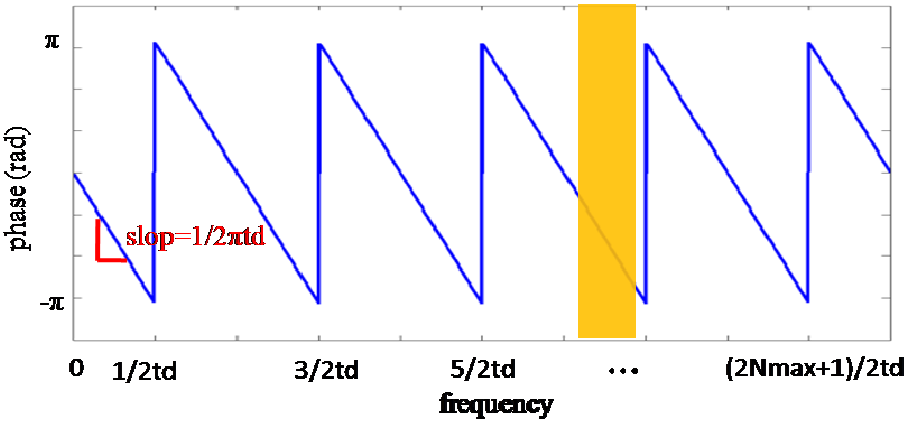



**Figure 5.3** Phase of the exponential delay term $e^{-t_d s}$.

## 5.4 Computation of Transport Delay and Optimized Delayed Rational Fit

The transport delay can be derived from the time responses, which are numerically obtained from time-domain field solvers or measured using TDR (time-domain reflectrometer), or from the frequency-domain data using characteristics of minimum phase or IFFT.

In this dissertation, we use inverse fast Fourier transform (IFFT) to compute transport delays from frequency-domain data. First, IFFT converts the frequency-domain data into the time-domain responses. After obtaining the time-domain responses via convolution of the obtained time-domain responses and a Gaussian pulse in (2.33), the peak-to-peak delays between ports are measured. A procedure of IFFT to ensure that the time-domain responses will be real is provided in the Appendix A.

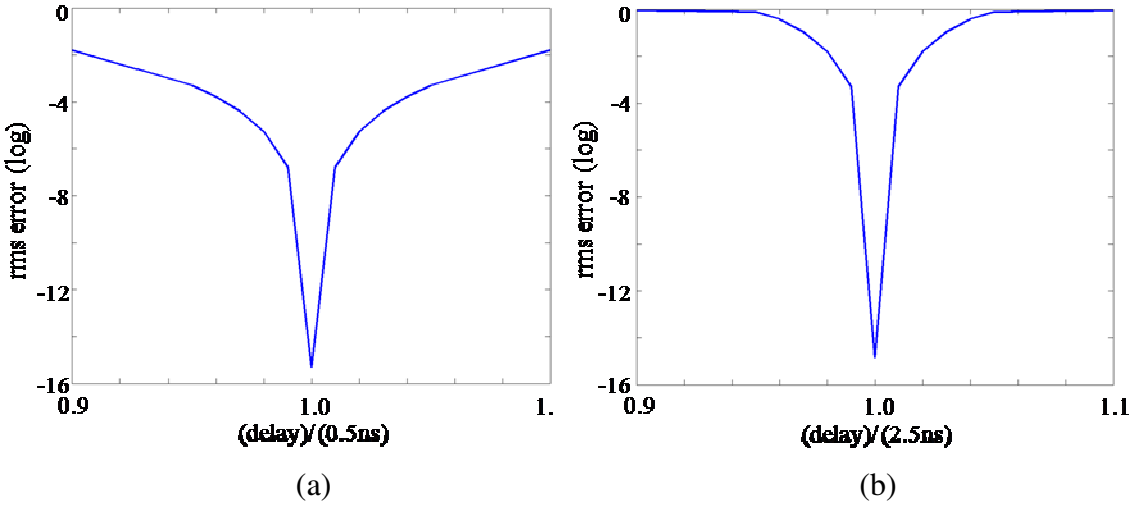
However, the estimated delay via IFFT is only the approximate value, so the estimated delay can be larger or smaller than the actual transport delay in the system. When the delay is overestimated, the delay extracted frequency data become noncausal and have the $e^{jt_d s}$ term embedded in the delay extracted data. For the underestimated delay, the delay extracted data also have the $e^{-jt_d s}$ term inside, which prevents order reduction and accuracy enhancement of the delayed rational function approximation. Therefore, it is expected that the delayed rational function approximation can be optimized by changing the estimated delay.

Next, we are going to address the accuracy of delayed rational function approximations depending on the estimated delay, and find out the optimized delayed rational function approximation based on the discussion checking the RMS error depending on the estimated delay.

Figure 5.4 shows RMS error of the delayed rational function approximation with the order $N = 2$ as a function of the estimated transport delay, when only stable poles are used for the rational function fitting (kill = 2 in vecfit.m). In the figure, RMS error reaches the minimum value and the generated fit becomes most accurate when the estimated delay equals the ideal value of the actual transport delay.

When we take a close look at the shape of the RMS error plots, the plots are symmetrical around the minimum value. However, the slopes around the minimum value for the 50 cm lossless TL are steeper than those for the 10 cm lossless TL. This implies that RMS error variation of the longer TL is more critical to the delay around the peak, which may be due to the shapes of the phase of the transfer scattering

parameter. For a long TL, the phase of the transfer function changes more rapidly, and the slope of the linear phase is larger. Hence, RMS error of the delayed rational function fit becomes more critical to the estimated value of the transport delay.

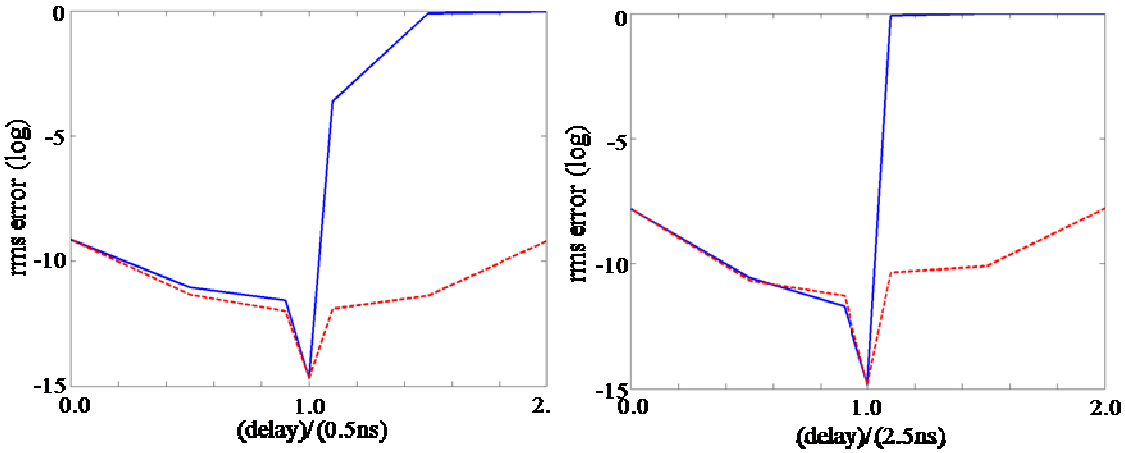



(a) (b)

**Figure 5.4** RMS errors depending on the extracted delay for the lossless TL of (a) 10 cm, (b) 50 cm length when $N = 2$. The x-axis is rescaled to the ideal value of the time delay.

Next, we extend the range of the time delay and plot the RMS errors depending on the transport delay. We computed the RMS errors of the delayed rational function approximation via VF, with $N = 20$ for the 10 cm TL, and $N = 50$ for the 50 cm TL. This time, the order $N$ of the rational function fit was set to be large enough not to influence the accuracy of the macromodel in that time delay range. The computed RMS errors are plotted in Figure 5.5. The solid line depicts RMS error when only stable poles are used, and the dotted line shows when unstable poles are allowed.

In Figure 5.5, the minimum RMS error was also obtained at the actual transport




(a) (b)

**Figure 5.5** RMS error depending on the extracted delay for lossless TL (a) 10 cm and (b) 50 cm long. *N* was assigned 20 for the 10 cm TL, 50 for the 50 cm TL. The *x*-axis is rescaled to the ideal value of the time delay. Solid line: only stable poles are used; dots: unstable poles are allowed.

delay; the plot is not symmetric when stability is enforced, and it increases significantly beyond the minimum point, while the plot is almost symmetric when the stability is not enforced. For the overestimated delay, VF with stability enforcement cannot approximate the delay extracted data accurately. This result suggests that the stable model of VF from the non-causal data becomes an ill-posed problem with negative impact on accuracy of the rational fit [34], which will be explained next.

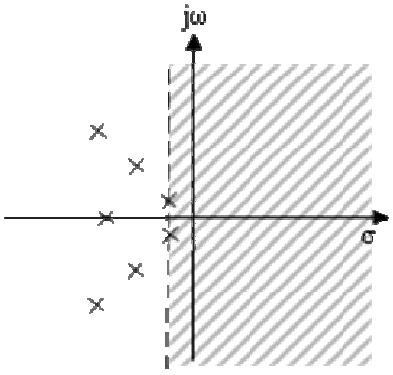
As mentioned in Chapter 2, the system is causal when the ROC is a half-plane open on the right, i.e., $Re\{s\}>\sigma_0$ for some real value of $\sigma_0$, and the existence of the frequency data indicates the existence of the Fourier transform, which is the sufficient and necessary condition for a system to be BIBO (bounded input bounded output)

stable, and the stability indicates that the ROC includes the imaginary axis in the Laplace domain.

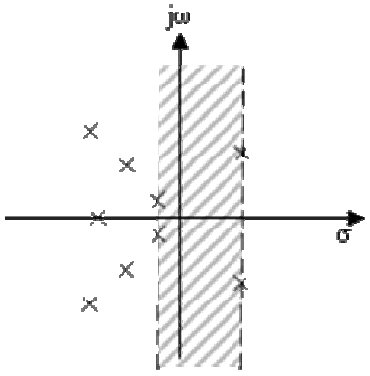
Actually, when the frequency data are given, the ROC of a rational function approximation for a system function can be presented in three ways in accordance with the pole distribution as shown in Figure 5.6. The system poles are represented as crosses. The first one has all poles in the left half-plane, the second has poles in both planes, and the third has all poles in the right half-plane. Among the three ROCs, only the first one is causal because the ROC is a half-plane open on the right. It means that the rational function fitting of a non-causal system has poles in the right half-plane also.

When transfer function data of a system are regarded as the system equivalently, the reason why the stable macromodel of VF from the data becomes an ill-posed problem can be explained by the previous discussion. If the delay is overestimated, delay-extracted data become non-causal and poles of the generated rational function fit begin to locate in the right half-plane as in (b) and (c). Hence, the VF algorithm with the poles in the left half-plane only for stability enforcement, which is used for the delayed rational function approximation, cannot accurately capture the noncausal data.

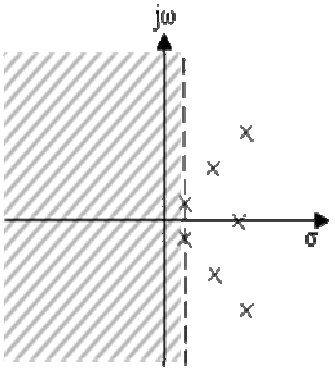
Using this inaccuracy of VF with stability enforcement for approximating non-causal data, the delayed rational function approximation can be optimized, preserving the causality of the system.




(a)




(b)




(c)

**Figure 5.6** Three possible ROCs for an arbitrary frequency dataset: (a) causal, (b) and (c) non-causal.

## 5.5 Limitation of Delayed Rational Function Approximation

In Section 5.3, we proved the benefits of the delay extraction using the lossless transmission line with matched terminations. However, not all types of transfer functions can benefit from the delay extraction in the accuracy and order reduction. Even after extracting the transcendental function of the delay from the transfer function, the other transcendental terms can still reside in frequency data.

For example, consider the transmission coefficient, $S_{21}$, of a two-port cable which is characterized by p.u.l. parameters of *R, L, C*, and *G*, and is *d* m long,

$$S_{21} = \frac{(1-\Gamma^2)X}{(1-\Gamma^2 X^2)}, \tag{5.5}$$

where

$$\begin{aligned} &\Gamma = \frac{Z_c - Z_0}{Z_c + Z_0}, \quad X = e^{-\gamma d}, \\ &Z_c = \sqrt{\frac{R + j\omega L}{G + j\omega C}}, \quad \gamma = \sqrt{(R + j\omega L)(G + j\omega C)}. \end{aligned} \tag{5.6}$$

The denominator of $S_{21}$ can be expanded using the Taylor expansion as

$$\begin{aligned} S_{21} &= [(1-\Gamma^2)X]\sum_{k=0}^{\infty}(\Gamma^2 X^2)^k, \\ S_{21} &= (1-\Gamma^2)e^{-\gamma d}[1+\Gamma^2 e^{-2\gamma d} + \Gamma^4 e^{-4\gamma d} + \cdots], \end{aligned} \tag{5.7}$$

where *d* is the length between the ports. Let $\gamma = \alpha + j\beta$ and $\beta = \omega / v_p$ when $v_p$ is the phase velocity in the cable. Then, (5.7) can be represented as

$$S_{21} = (1-\Gamma^2)e^{-\alpha d}e^{-j(d/v_p)\omega}[1+\Gamma^2 e^{-2\alpha d}e^{-j2(d/v_p)\omega} + \Gamma^4 e^{-4\alpha d}e^{-j4(d/v_p)\omega} + \cdots]. \tag{5.8}$$

Let $j\omega = s$ and $d / v_p = t_d$, where $t_d$ is the transport delay.

$$\begin{aligned} S_{21} &= (1-\Gamma^2)e^{-t_d s}e^{-\alpha d}[1+(\Gamma^2 e^{-2\alpha d})e^{-2t_d s}+(\Gamma^4 e^{-4\alpha d})e^{-4t_d s}+\cdots] \\ &= e^{-t_d s}F(e^{-2t_d s}), \end{aligned} \tag{5.9}$$

where $F(s) = (1-\Gamma^2)e^{-\alpha d}[1+(\Gamma^2 e^{-2\alpha d})e^{-2t_d s}+(\Gamma^4 e^{-4\alpha d})e^{-4t_d s}+\cdots]$, which is approximated with rational functions. Equation (5.9) shows that the proposed delayed extraction method prior to the rational function fitting is the one dominant delay extraction because the equation involves other transcendental functions of multiple delays. The one dominant delay extraction is valid when the second term in the bracket is negligible compared with 1, which means that the reflection coefficient, $\Gamma$, should be small enough, or the cable should be lossy enough for reflected waves to decay out in the DUT when terms other than the first term represent the waves that are reflected at ports and travel inside of the cable physically.

Next, we are going to consider mismatched conditions to provide a guideline to choose the delayed rational function approximation instead of VF. $S_{21}$ of a lossless TL with $L = 2.5$ nH/cm, $C = 1$ pF/cm and length $l$ = 10 cm was analyzed [33] depending on the characteristic impedance of 50 Ω, 55 Ω and 300 Ω, and the values are plotted in magnitude (first row), phase (second row), and the delay-extracted phase (third) in Figure 5.7. The reflection coefficient $\Gamma$ was 0 for 50 Ω (matched), 0.048 for 55 Ω, 0.71 for 300 Ω. The mismatched termination (the characteristic impedance of the TL and that of $S_{21}$ are different) develops reflected waves at ports.

It is observed from the figure that as the reflecting coefficient is larger, the peak values of variation in the magnitude become larger, and that the phase still shows 2π

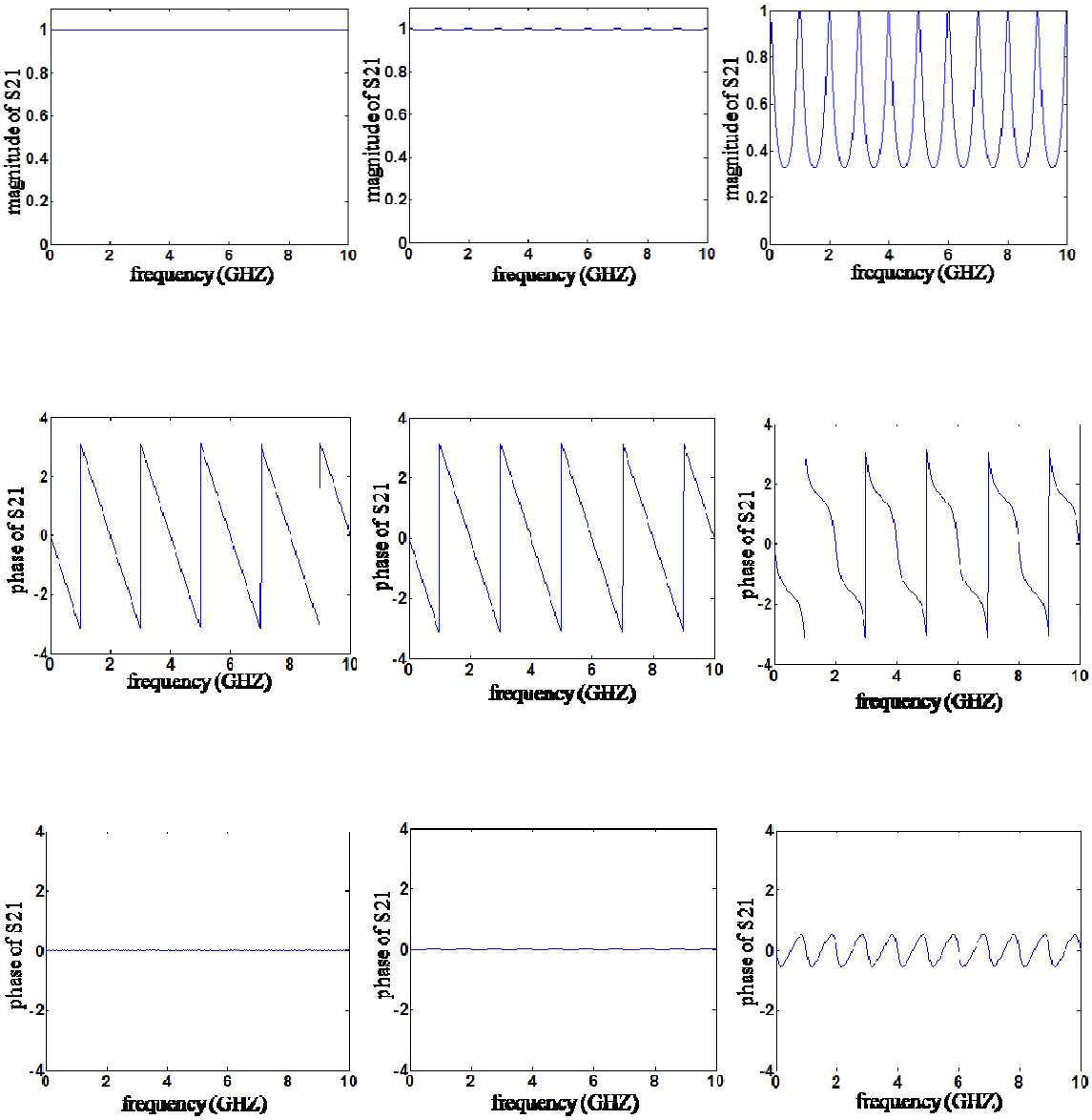
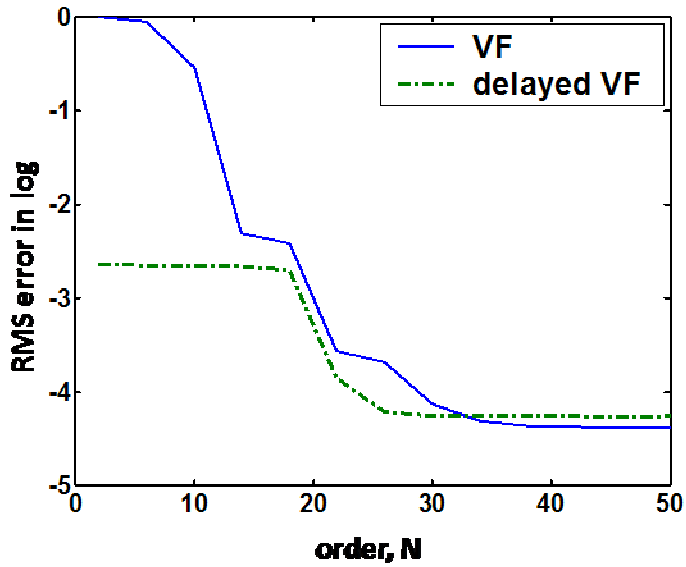



**Figure 5.7** Plots of $S_{21}$. The first column is for matched termination, the second for 55 Ω termination, and the third for 300 Ω termination. The first row is for magnitude, the second for phase, and the third for delay extracted phase.

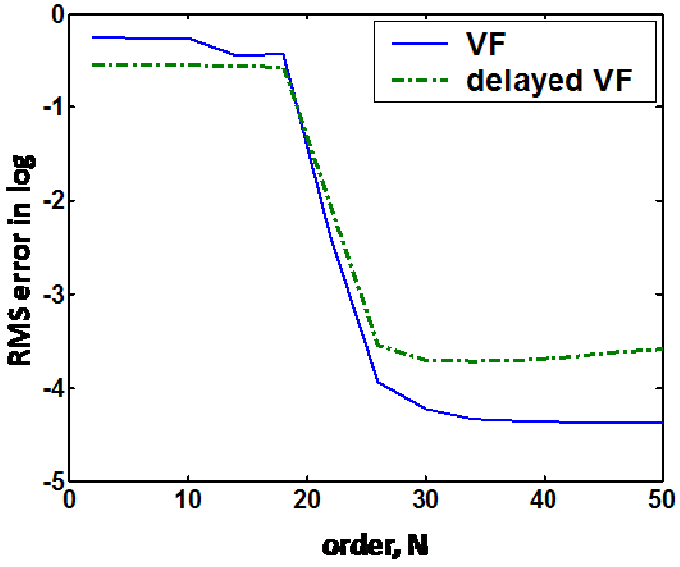
jumps but the straight line becomes curved. As the reflection becomes larger, the shapes of frequency data in magnitude and phase are perturbed from those of the lossless TL. After delay extraction, there are still ripples in phases because of reflections for both mismatched terminations even though the ripples are small for the 55 Ω termination. From the graphical viewpoint of peak location and number [22], we can expect that one dominant-delay extraction cannot reduce the order of rational function fit to present ripples in phase and magnitude when the reflection is significance like the 300 Ω termination.

We approximated the $S_{21}$ using VF and the delayed VF. Figure 5.8 plots the RMS errors of the macromodels. When 1% error is accepted, the order reduction via the delayed VF can be observed for the case of 55 Ω termination ($N = 2$ is good enough as the matched case), but for the case of 300 Ω termination the order reduction is not observed and even VF works better than the delayed VF. For the 55 Ω termination, magnitudes of reflecting waves are smaller than the error limit; the transfer function could be treated as a lossless transmission line, so delayed rational function was effective. However, the reflections from 300 Ω terminations are not negligible, resulting in significant ripples in phase and magnitude even after delay extraction, so the delayed rational function presenting one dominant delay term is not suitable.

From this result, we can derive a guideline for the usage of the delayed rational function approximation. For effective modeling via the delayed VF, the magnitude should be smooth with negligible ripples (compared with error limit) and only the phase varies linearly with 2π jumps, like that of a lossy TL.




(a)




(b)

**Figure 5.8** Plots of RMS errors of macromodes of $S_{21}$ with (a) 55 Ω terminations and (b) 300 Ω terminations.

## 5.6 Validation Studies

In this section, two examples are considered to demonstrate the performance and accuracy of the delayed rational function approximation based on scattering parameters; we also consider the validity and the guidelines for using the approximation method.

### 5.6.1 Coupled transmission lines

Our first example concerns the two coupled transmission lines shown in Figure 5.9 [8]. The transmission lines are 30 cm long and have the following parameters:

$$R = \begin{bmatrix} 1.24 & 0 \\ 0 & 1.24 \end{bmatrix} \Omega/\text{cm}$$

$$L = \begin{bmatrix} 3.361 & 0.865 \\ 0.865 & 3.361 \end{bmatrix} \text{nH/cm}$$

$$C = \begin{bmatrix} 1.29 & -0.197 \\ -0.197 & 1.29 \end{bmatrix} \text{pF/cm}$$

$$G = 0 \text{ S/cm.}$$

S parameters were analyzed in HSPICE [33] over the frequency range from 10 MHz to 20 GHz. The transport delays between ports were extracted using the IFFT. The obtained transport delay between the near end and the far end was 1.825 ns. Both the

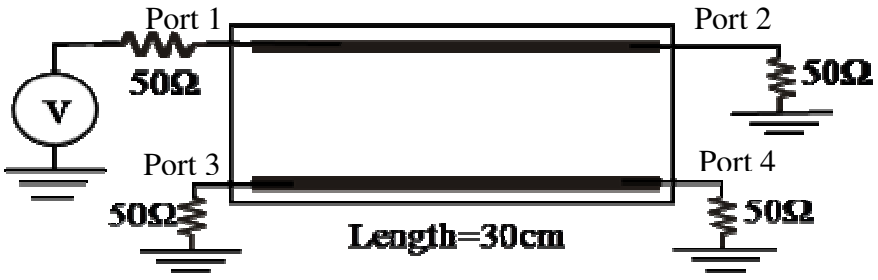



**Figure 5.9** Coupled transmission line network.

frequency data and the delay were used for the delayed rational function approximation for the S-parameter matrix, element by element, using VF after delay extraction.

Figure 5.10 shows the fitting result of $S_{21}$. In Figure 5.10, RMS errors of the rational function approximation, with and without delay extraction, are compared depending on the order *N* when stability of the fit was enforced. The solid line in Figure 5.10(a) shows the RMS error of the macromodeling without delay extraction, while Figure 5.10(b) plots the one with delay extraction. The dot line plots $5e^{-3}$ in log (which is the largest RMS error that makes the difference between the approximation and the input data insignificant for these lossless transmission lines). So when the value $5e^{-3}$ is admitted for the RMS error, 90 is required for the order of the macromodel of no delay extraction, while 20 is enough for the delay extracted macromodel. The order reduction is observed.

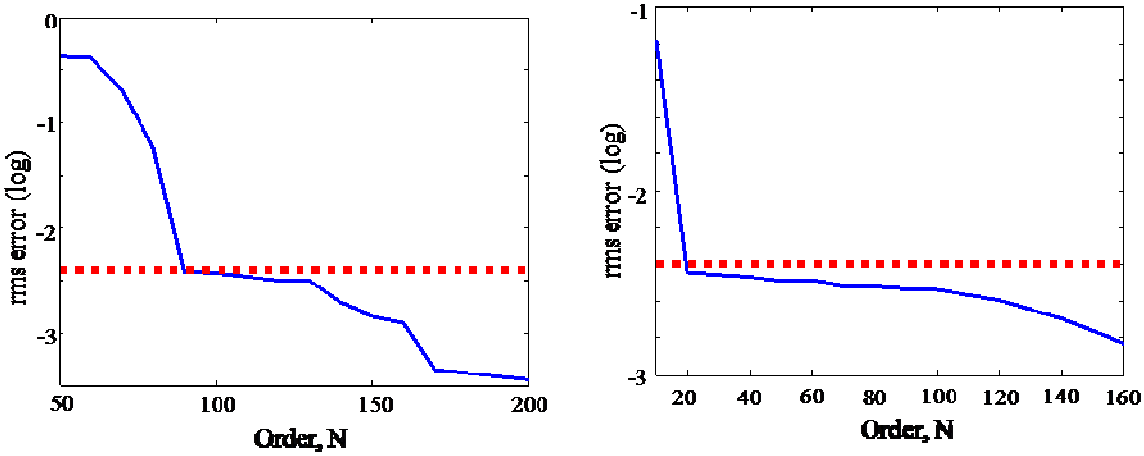



**Figure 5.10** RMS error depending on the order *N* of the rational function approximation for coupled transmission lines: (a) without delay extraction, and (b) with delay extraction. Solid line: RMS error in log; dotted line: log($5e^{-3}$).

In Figure 5.11, the RMS error is plotted versus the estimated delay between ports of far-end and near-end when the order $N$ is 170 for the elements of no delay extraction and 20 for the delay extracted elements. When the extracted delay is 1.825 ns, the RMS error reaches the minimum value, and it rapidly increases beyond 1.825 ns. Hence, the delayed rational function approximation could be optimized at the transport delay of 1.825 ns.

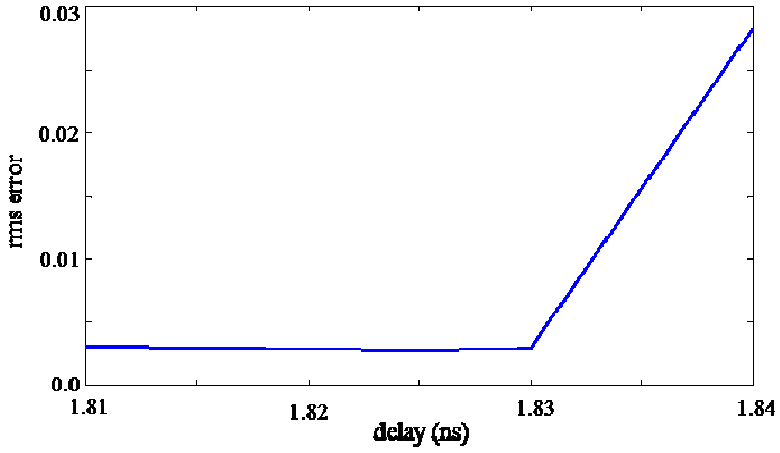
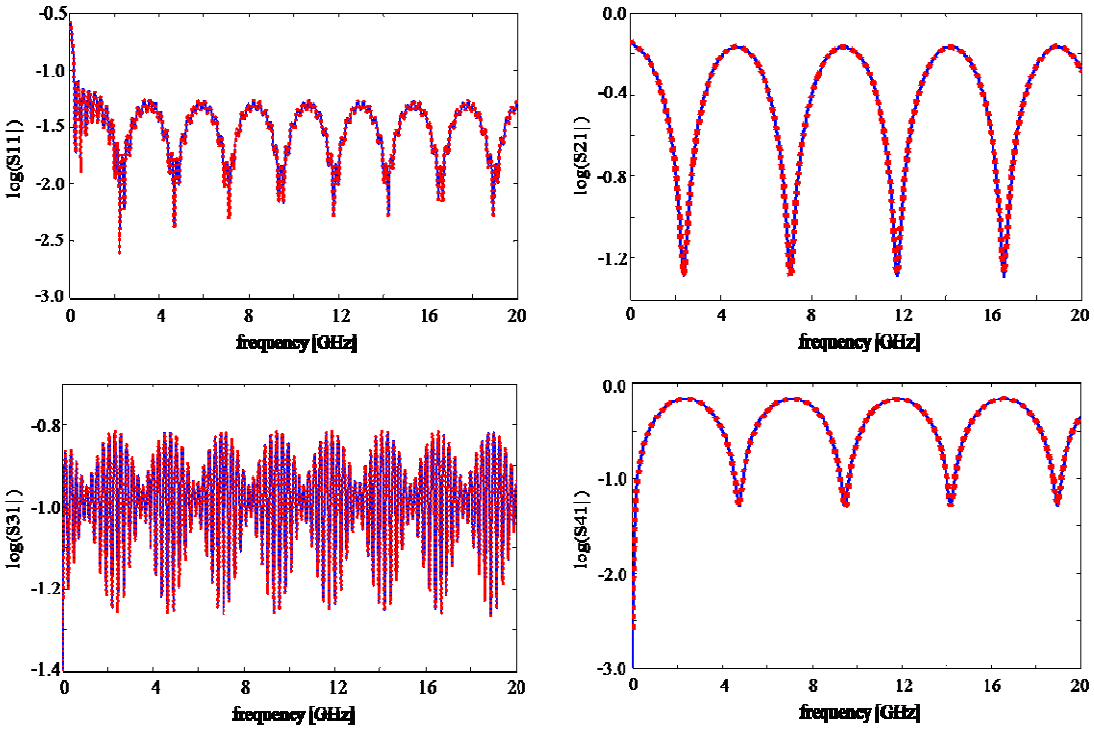


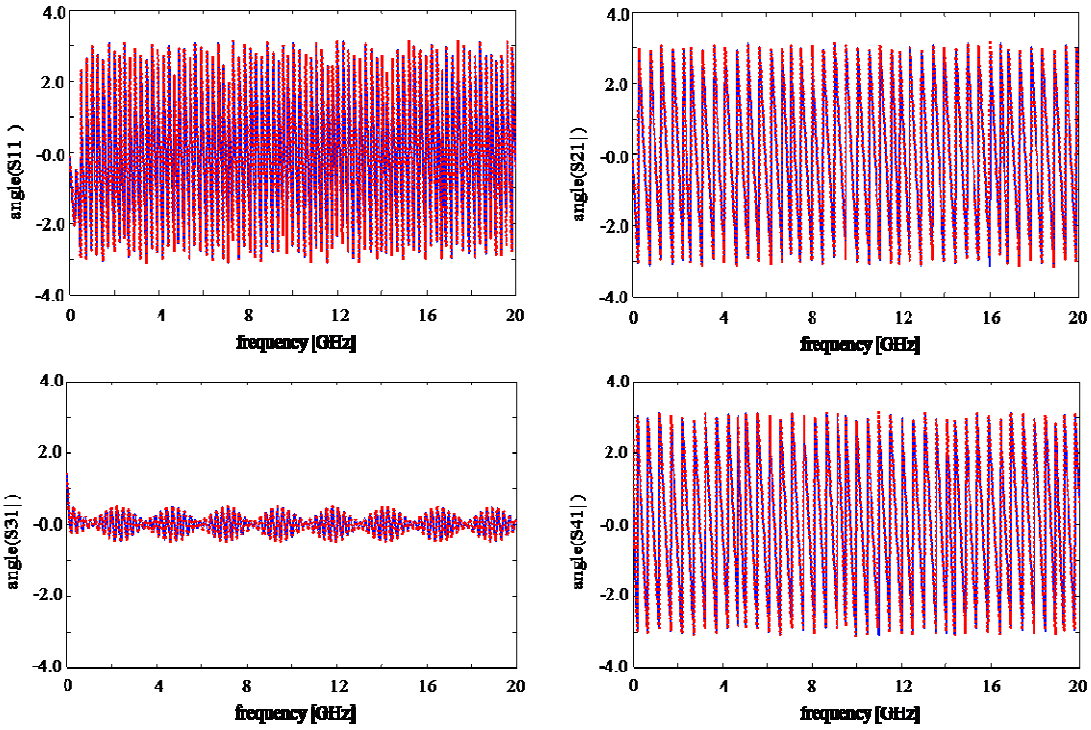

**Figure 5.11** RMS error depending on the estimated transport delay between ports of near-end and far-end.

For the elements between the near-end and the far-end, 1.825 ns was extracted, and 20 was assigned for the order $N$. For others without delays, 170 was assigned. The magnitudes and the phases of the elements from $S_{11}$ to $S_{41}$ are plotted in Figure 5.12. Very good agreement is observed between the data from the macromodel and reference values. The errors are plotted in log scale in Figure 5.13, which demonstrate the accuracy of the delayed rational function approximation method.




(a)

**Figure 5.12** Comparison between reference values and data from macromodel. (a) Magnitudes (in dB), and (b) phases (in radians) of the S parameters from $S_{11}$ to $S_{41}$. Solid line: reference values; dots: values from the macromodel of the proposed method.




(b)

**Figure 5.12** Continued.

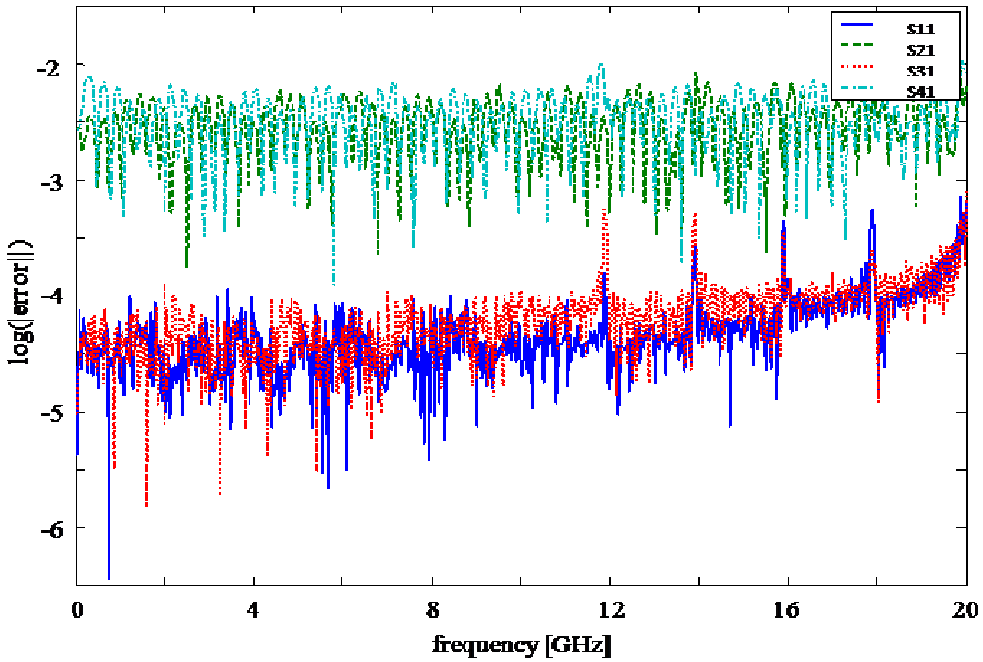



**Figure 5.13** Absolute values of the difference between reference values and data from macromodel in log scale.

### 5.6.2 Lossy transmission line

The transporting scattering parameter data $S_{21}$ which were measured from a lossy transmission line over the bandwidth 0 Hz < $f$ < 50 GHz were used. The data were sampled at 2001 points over the bandwidth.

The delay was estimated to be 0.45 ns in an optimized manner by computing the RMS error depending on the estimated value of the transport delay. Both VF and the delayed VF as proposed in this work were used for macromodeling. The RMS errors for the two fitting methods are plotted depending on the order of the rational function fit in Figure 5.14. When 1% error is accepted, about 20 is large enough for the delayed rational function fit while about 60 is necessary for VF.

When we take a look at the $S_{21}$ in magnitude and phase, the magnitude is very smooth and the phase is changing linearly with 2π jumps because of the transport delay in Figure 5.15. Hence, even without the comparison of RMS errors, we could expect that the delayed rational function works better for this lossy TL based on the discussion in Section 5.5.

Figure 5.15 shows the fitting result of the delayed rational function approximation with $N = 20$ and estimated delay 0.45 ns. The fitting data show very good agreement with the reference values of the measurement data.

## 5.7 Summary

In this chapter, the delayed rational function approximation of S parameters of the passive DUT was proposed to facilitate causality preservation, and to enhance the

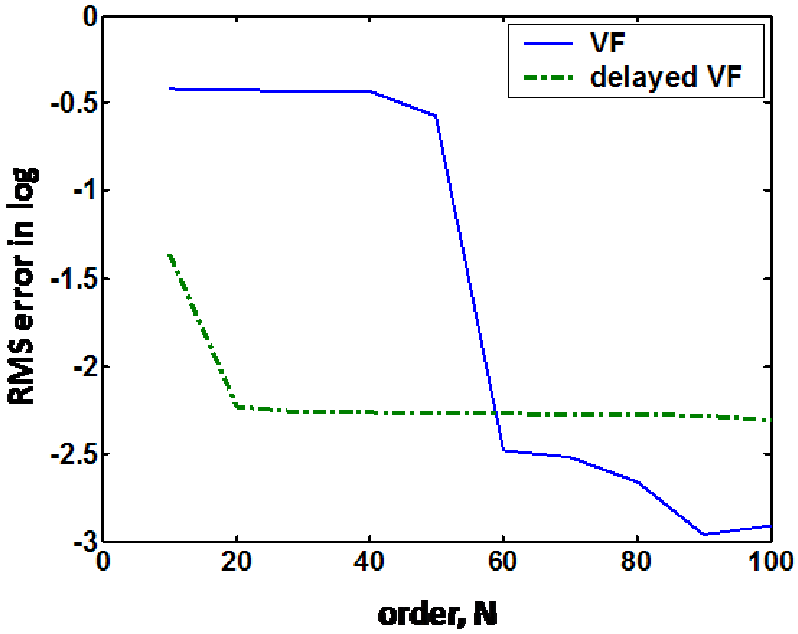
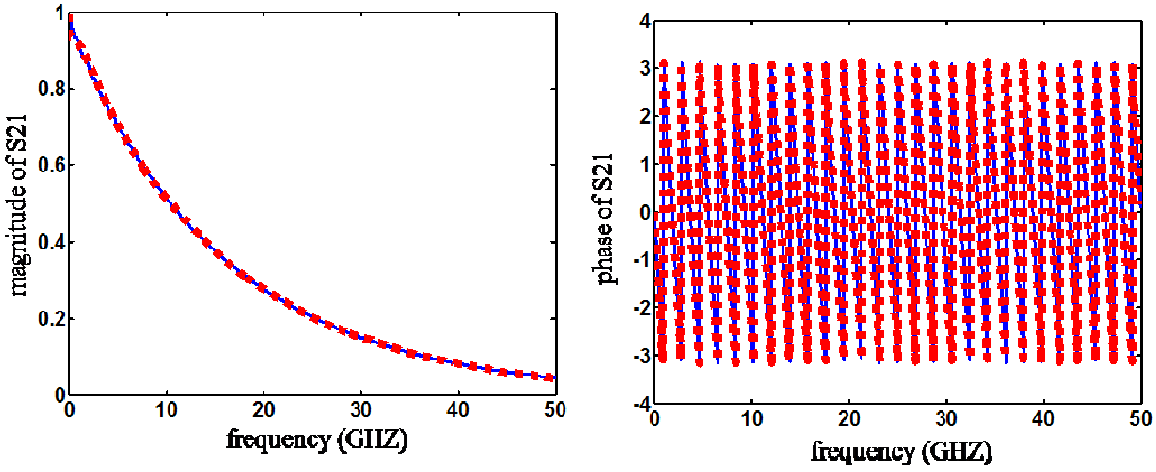



**Figure 5.14** Plots of RMS errors vs. order *N*.




(a) (b)

**Figure 5.15** Comparison between reference values (solid) and data from macromodel (dotted). (a) Magnitude and (b) phases of $S_{21}$.

fitting accuracy with reduced order. Toward these goals, a dominant transport delay is first extracted from the given frequency data and VF is applied for rational function fitting. From the fitting results of lossless TLs, we could derive the amount of order reduction resulting from the delay extraction. Also, we presented the limitation of the one dominant delay extraction for modeling systems with multiple reflections via the proposed method. From the discussion of the limitation, we could derive a guideline for the usage of the delayed VF. When the magnitude of frequency data are smooth and the phase is linearly changing with $2\pi$ jumps, the delayed rational function approximation shows its benefits in modeling.

For validation study, two interconnect systems were considered. Their fitting results successfully demonstrated the performance of the delayed rational function approximation.

# CHAPTER 6
# PASSIVITY ENFORCEMENT METHODS

Passivity implies that the system cannot generate more energy than it absorbs. In this dissertation, developed modeling methods only focus on passive systems; therefore, generated models should be passive also. The violation of passivity incurs artificial oscillations even when the generated models are connected to other passive networks, thus prohibiting stable time-domain simulations.

The passivity violation may occur at two points in the modeling process. First, the measured or the numerically obtained data from a passive system can be nonpassive due to measurement errors caused by improper measurement process or the presence of spurious noise, or computational errors in the numerical analysis. Second, the passivity of the resultant macromodel cannot be guaranteed unless it is imposed as a constraint in the mathematical procedure used for macromodel generation, even when the original input data are passive.

Hence, we need a passivity enforcement process to be used as part of the macromodel generation [36, 40, 58-61]. In this chapter, we focus mainly on methods that attempt to enforce passivity after the macromodel has been generated, and among various macromodeling methods, the element-by-element fitting method in Chapter 2 is considered.

The element-by-element rational function fitting method shows benefits in computational cost and efficiency. However, passivity enforcement techniques have

been developed for rational function approximations which share a common set of poles for the whole elements. Hence, we explored passivity enforcement algorithms for the element-by-element fitting method, and we realized that the quadratic programming method [40] is originally designed to admit rational function approximations with different sets of poles for each matrix element.

The objective of this chapter is to demonstrate that the element-by-element fitting method can be rendered passive through the theory and application of the passivity enforcement via quadratic programming (PEQP) method. This chapter is organized as follows. In Section 6.1, various passivity enforcement techniques are reviewed, and the theory of PEQP is presented in Section 6.2. In Section 6.3, PEQP is demonstrated as a means for enforcing passivity of rational function fits of network matrices of passive multiports generated via an element-by-element rational function fitting.

## 6.1 Background

Passivity enforcement methods are aptly categorized into three approaches: passive filter approach, quadratic programming approach, and Hamiltonian matrix approach [62].

First, the passive filter approach is based on the macromodel of an admittance (or an impedance) matrix with a single set of poles used in the rational fitting of all elements. Then the rational function approximation for a single-port system can be written as

$$
\begin{aligned}
Y(s) &= D_0 + \sum_{r=1}^{Nr} \frac{R_r}{s - p_r} + \sum_{c=1}^{Nc} \left( \frac{R_c}{s - p_c} + \frac{\overline{R}_c}{s - \overline{p}_c} \right) \\
&= D_0 + \sum_{r=1}^{Nr} \frac{R_r}{s - p_r} + \sum_{c=1}^{Nc} \frac{\gamma_1^{(c)} s + \gamma_0^{(c)}}{s^2 + \delta_1^{(c)} s + \delta_0^{(c)}}.
\end{aligned}
\tag{6.1}
$$

Equation (6.1) shows separately the terms with real poles and residues, $p_r$, $R_r$, and $r$=1,2,...,$N_r$, and the terms with complex-conjugate poles and residues, $p_c$, $R_c$, and $c$=1,2,...,$N_c$. When $p_c = -\sigma_c + j\omega_c$ and $R_c = \alpha_c + j\beta_c$, $\gamma_0^{(c)} = 2(\alpha_c \sigma_c - \beta_c \omega_c)$, $\gamma_1^{(c)} = 2\alpha_c$, $\delta_0^{(c)} = |p_c|^2$, $\delta_1^{(c)} = 2\alpha_c$. For a multiport system, (6.1) assumes the form

$$
\boldsymbol{Y}(s) = [D_0] + \sum_{r=1}^{Nr} \frac{1}{s - p_r} [R_r] + \sum_{c=1}^{Nc} \frac{s}{s^2 + \delta_1^{(c)} s + \delta_0^{(c)}} [\gamma_1^{(c)}] + \frac{1}{s^2 + \delta_1^{(c)} s + \delta_0^{(c)}} [\gamma_0^{(c)}], \tag{6.2}
$$

where the matrices $[D_0]$, $[R_r]$, $[\gamma_1^{(c)}]$, and $[\gamma_0^{(c)}]$ are $N_p$x$N_p$ residue matrices for an $N_p$-port system.

Then, the passive filter approach makes each partial term matrix in (6.2) passive based on the passivity condition of

$$
\mathrm{Re}\{\boldsymbol{Y}(s = j\omega\} \geq 0 \tag{6.3}
$$

for all $\omega$.

This approach guarantees the global passivity of the passivity enforced macromode in this manner, however, each partial term in (6.2) need not necessarily be passive for the entire macromodel to be passive. Accuracy of the macromodel may be impaired by excessively imposed passivity constraints [50].

Second, the quadratic programming approach perturbs the residues of the rational approximations to make the real part of the admittance (or impedance) matrix positive

definite under the minimal perturbation via quadratic programming at the selected frequency points. The limitation of this method is that the passivity of the resultant macromodel depends on the fineness of the selected frequency points, and that cannot be guaranteed in the entire frequency domain. In other words, the possibility exists that the macromodel may still violate passivity at frequencies different from those used for passivity enforcement.

Third, the Hamiltonian approach [60] is based on the characteristics of the Hamiltonian matrix for detecting the passivity-violating frequency band, and compensating for the violation via an iterative perturbation scheme.

The Hamiltonian matrix is determined by the matrices of state-space representations in accordance with the type of the system matrix: admittance, impedance, hybrid, or scattering matrix. When a time-invariant multiport system is macromodeled as the rational function approximation of the system matrix, the state-space representation is expressed as

$$\begin{aligned} \dot{\boldsymbol{z}}(t) &= \boldsymbol{A}\boldsymbol{z}(t) + \boldsymbol{B}\boldsymbol{x}(t) \\ \boldsymbol{y}(t) &= \boldsymbol{C}\boldsymbol{z}(t) + \boldsymbol{D}\boldsymbol{x}(t), \end{aligned} \tag{6.4}$$

where $\boldsymbol{x}(t)$ and $\boldsymbol{y}(t)$ are the system input and output variables, and $\boldsymbol{z}(t)$ is the state vector (see Section 2.5 for more information).

Then, the Hamiltonian matrix $\boldsymbol{H}$ for the scattering matrix is defined as

$$\boldsymbol{H} = \begin{bmatrix} \boldsymbol{A} - \boldsymbol{B}\boldsymbol{R}^{-1}\boldsymbol{D}^{T}\boldsymbol{C} & -\boldsymbol{B}\boldsymbol{R}^{-1}\boldsymbol{B}^{T} \\ \boldsymbol{C}^{T}\boldsymbol{S}^{-1}\boldsymbol{C} & -\boldsymbol{A}^{T} + \boldsymbol{C}^{T}\boldsymbol{D}\boldsymbol{R}^{-1}\boldsymbol{B}^{T} \end{bmatrix}, \tag{6.5}$$

where $\boldsymbol{R} = (\boldsymbol{D}^T\boldsymbol{D} - \boldsymbol{I})$ and $\boldsymbol{S} = (\boldsymbol{D}\boldsymbol{D}^T - \boldsymbol{I})$. For the admittance (impedance, hybrid) matrix, the Hamiltonian matrix $\boldsymbol{H}$ is defined as

$$\boldsymbol{H} = \begin{bmatrix} \boldsymbol{A} - \boldsymbol{B}(\boldsymbol{D} + \boldsymbol{D}^T)^{-1}\boldsymbol{C} & -\boldsymbol{B}(\boldsymbol{D} + \boldsymbol{D}^T)^{-1}\boldsymbol{B}^T \\ \boldsymbol{C}^T(\boldsymbol{D} + \boldsymbol{D}^T)^{-1}\boldsymbol{C} & -\boldsymbol{A}^T + \boldsymbol{C}^T(\boldsymbol{D} + \boldsymbol{D}^T)^{-1}\boldsymbol{B}^T \end{bmatrix}. \tag{6.6}$$

From the defined Hamiltonian matrix of $\boldsymbol{H}$, violation of passivity is detected if the matrix has any imaginary eigenvalue, $j\omega_0$. From the imaginary eigenvalue, we can obtain the radial frequency $\omega_0$ which determines the boundary values of the passivity-violating frequency bands. After the passivity-violating frequency band is determined, the matrix $\boldsymbol{C}$ is modified for the system to be passive in an iterative scheme.

## 6.2 Passivity Enforcement via Quadratic Programming for Element-by-Element Rational Function Approximations

The objective of this section is to provide a brief overview of PEQP and to show that it is originally designed for element-element rational function fitting, which has different sets of poles for each matrix element, even though, in the context of the VF applications, it has only been used for matrix rational function fitting.

It is assumed that the system under consideration is a passive $N_p$-port system; hence, its network representation is in terms of an $N_p$ x $N_p$ admittance matrix. When the element-by-element rational fitting is used, the generalized mathematical representation of each element $(i, j)$ of $\boldsymbol{Y}(s)$ can be written as

$$\{\boldsymbol{Y}(s)\}_{ij} = \sum_{m=1}^{N_{ij}} \frac{R_{m,ij}}{s - p_{m,ij}} + D_{ij} + sE_{ij}, \tag{6.7}$$

where $N_{ij}$ is the order of the rational function fit for the element (*i, j*) of $\boldsymbol{Y}(s)$, and $D_{ij}$, $E_{ij}$, $p_{m,ij}$ and $R_{m,ij}$ are constants obtained by the rational fitting process.

As presented in Chapter 2, a system is passive if and only if its admittance matrix $\boldsymbol{Y}$ satisfies the following conditions [63]:

(1) Each element of $\boldsymbol{Y}(s)$ is defined and analytic in $\mathrm{Re}(s) > 0$.

(2) $\boldsymbol{Y}(\overline{s}) = \overline{\boldsymbol{Y}}(s)$, where $\overline{\ }$ denotes complex conjugation.

(3) $\boldsymbol{Y}(s)$ is positive real.

Condition (3) may be expressed mathematically as $\boldsymbol{v}^H[\boldsymbol{Y}^T(\overline{s}) + \boldsymbol{Y}(s)]\boldsymbol{v} \geq 0$ for all complex values of *s* with $\mathrm{Re}(s) > 0$ and for any arbitrary vector $\boldsymbol{v}$, where the superscript *H* denotes the transpose conjugate operation. Alternatively, this condition means that all eigenvalues of $\boldsymbol{G} = \mathrm{Re}\{\boldsymbol{Y}\}$ must be positive for $\omega \in \mathbb{R}$ when $s = j\omega$.

The first two conditions are automatically ensured via the rational function fitting of each element with the stability constraint enforced. In order to enforce the third condition, PEQP [40] perturbs the residues of the rational approximations $\boldsymbol{C}$ and the constant terms $\boldsymbol{D}$ to make $\boldsymbol{G}$ positive definite under the minimal perturbation via quadratic programming. The reason for dropping $\boldsymbol{E}$ in the consideration of passivity is that the first order tern in (6.7) is purely imaginary for $s = j\omega$.

In the context of the element-by-element fitting of the admittance matrix, $\boldsymbol{Y}(s)$ is first unfolded into a single vector $\boldsymbol{y}_{fit}$, and the elements of $\boldsymbol{C}$ and $\boldsymbol{D}$ into a single vector $\boldsymbol{u}$. Then the relation between $\boldsymbol{y}_{fit}$ and $\boldsymbol{u}$ is

$$\boldsymbol{y}_{fit} = \boldsymbol{M}\boldsymbol{x} = \begin{bmatrix} \frac{1}{s-p_{1,11}} & \cdots & \frac{1}{s-p_{N_{11},11}} & 1 & \cdots & 0 & \cdots & 0 & 0 \\ \vdots & \ddots & \vdots & \vdots & \ddots & \vdots & \ddots & \vdots & \vdots \\ 0 & \cdots & 0 & 0 & \cdots & \frac{1}{s-p_{N_{nn},nn}} & \cdots & \frac{1}{s-p_{N_{nn},nn}} & 1 \end{bmatrix} \boldsymbol{u}, \quad (6.8)$$

which is same as the one in [40]. In [40], the calculation of the matrix $\boldsymbol{M}$ for a rational function fitting process which uses different poles for each one of the elements of the admittance matrix is also considered in one of the appendices. This means that the PEQP is more general than its specific application to enforcing passivity of a response matrix with all elements sharing a common set of poles. The more general form of approach, as depicted in (6.8), is the one we use for our purposes of enforcing passivity to element-by-element rational function fitting of response matrices.

A perturbation of $\boldsymbol{u}$ causes the change in $\boldsymbol{y}_{fit}$, which can be expressed as an incremental relationship as

$$\Delta\boldsymbol{y}_{fit} = \boldsymbol{M}\,\Delta\boldsymbol{u} \quad (6.9)$$

When we take the real part of (6.9),

$$\Delta\boldsymbol{g}_{fit} = \mathrm{Re}\{\Delta\boldsymbol{y}_{fit}\} = \mathrm{Re}\{\boldsymbol{M}\}\Delta\boldsymbol{u} = \boldsymbol{P}\,\Delta\boldsymbol{u}, \quad (6.10)$$

where vector $\boldsymbol{g}_{fit}$ holds all the columns of $\boldsymbol{G}$. Via the perturbation theory of eigenvalues, the relationship between the change of the eigenvalues of $\boldsymbol{G}$ and $\Delta\boldsymbol{u}$ can be derived as

$$\Delta\boldsymbol{\lambda} = \boldsymbol{Q}\Delta\boldsymbol{g}_{fit} = \boldsymbol{Q}\boldsymbol{P}\Delta\boldsymbol{u} = \boldsymbol{R}\Delta\boldsymbol{u}. \quad (6.11)$$

Then we can construct the constrained least squares approximation in order to force any negative eigenvalue of $\boldsymbol{G}$ to be positive via the smallest perturbation of $\Delta\boldsymbol{u}$ to the constructed rational function fit $\boldsymbol{y}_{fit}$ as

$$\begin{aligned} &\boldsymbol{y}(s) - (\boldsymbol{y}_{fit}(s) + \boldsymbol{M}\Delta\boldsymbol{u}) \to 0, \\ &\Delta\lambda = \boldsymbol{Q}\Delta\boldsymbol{g}_{fit} = \boldsymbol{QP}\Delta\boldsymbol{u} = \boldsymbol{R}\Delta\boldsymbol{u} \geq -\lambda \end{aligned} \tag{6.12}$$

for the negative eigenvalues. A least squares problem of (6.12) is solved via quadratic programming: Minimize

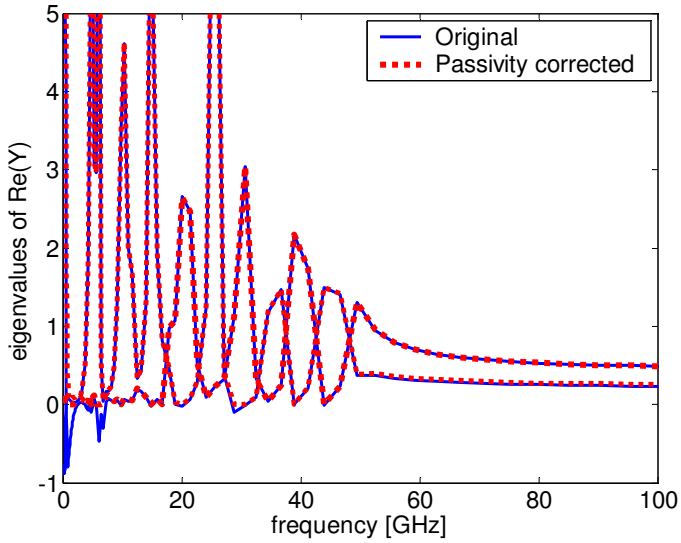
$$\frac{1}{2}\Delta\boldsymbol{x}^T\boldsymbol{W}\Delta\boldsymbol{u} - \boldsymbol{f}^T\Delta\boldsymbol{u}$$

$$\text{subject to } \boldsymbol{B}\Delta\boldsymbol{u} \leq \boldsymbol{c}\text{, where } \boldsymbol{W} = \boldsymbol{A}^T\boldsymbol{A}, \quad \boldsymbol{f} = \boldsymbol{A}^T\boldsymbol{b}. \tag{6.13}$$

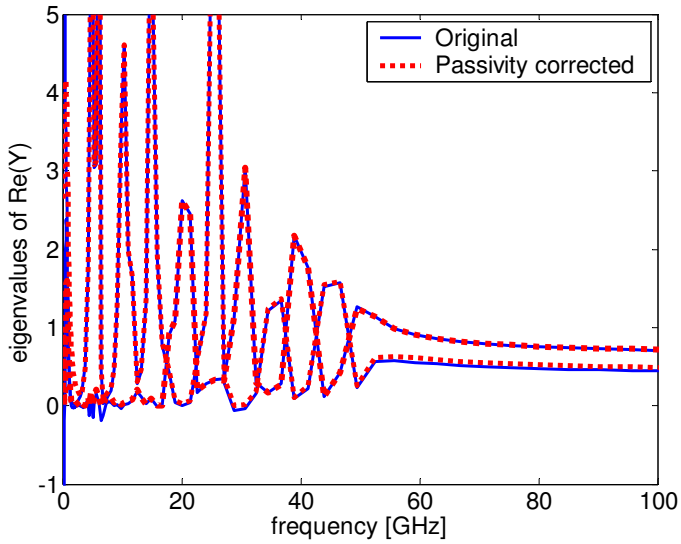
## 6.3 Validation Study

For the purpose of validating the proposed methodology for passivity enforcement of the element-by-element rational function fitting of the admittance matrix of a multi-port, measured admittance matrix data for an interconnect structure over the bandwidth 2 GHz $< f <$ 50 GHz were used. The available spectra were sampled at 801 points over the aforementioned bandwidth. Both matrix fitting and element-by-element matrix fitting were used for macromodeling the admittance matrix.

After constructing rational function fittings, the passivity of the constructed rational fit was checked and enforced in the frequency bandwidth of 10 Hz to 500 GHz. Figure 6.1 shows the eigenvalues of $\boldsymbol{G}$(s) for the case of both matrix fitting and element-by-element fitting, before and after passivity enforcement. The figure shows the existence of the nonpositive eigenvalues in both fittings, which means that both constructed




(a)




(b)

**Figure 6.1** Comparisons of the eigenvalues of the real part of the admittance matrix **G** from the rational function fit of (a) the original VF and (b) the element-by-element VF before and after passivity enforcement.

rational fits are not passive. But after passive enforcement with PEQP, all eignvalues become larger than or equal to zero. PEQP successfully enforced not only the passivity of the matrix fitting, but also the passivity of the element-by-element fitting. Also, the perturbation of the passivity enforcement process was negligibly small such that the application increased the RMS error from 0.13253 to 0.1368 for matrix fitting and from 0.1167 to 0.12861 for the element-by-element fitting. Considering the maximum eigenvalue of the admittance matrix, the perturbed RMS errors are negligible.

## 6.4 Summary

In this chapter, we have demonstrated that the passivity enforcement via quadratic programming methodology of [40] can be used to enforce passivity of rational function approximations which are generated via an element-by-element fitting method and have different sets of poles for each matrix element of admittance matrices of passive multiport systems.

# CHAPTER 7
# SPICE-COMPATIBLE EQUIVALENT CIRCUIT SYNTHESIS

There are basically two ways to incorporate the macromodel of distributed interconnect structures into circuit simulators [64]: (1) synthesize the equivalent circuit using basic circuit elements of the circuit simulator, or (2) use recursive convolution [45]. In this chapter, we present the application of both techniques for interfacing rational function approximations of the Y parameter with SPICE. In addition, we introduce an equivalent circuit synthesis scheme for delayed rational function fitting of S parameters.

## 7.1 Recursive Convolution

In general, converting a frequency-domain representation to a time-domain model through convolution has a quadratic runtime cost [64]. However, the computational cost through the recursive convolution is constant irrespective of the time when the frequency-domain macromodels are represented with the rational function fit of the pole-residue form, which is obtained by VF [64].

The recursive convolution is discussed in Chapter 2, in the context of TDVF. The recursive convolution method is based on the first order interpolation (piecewise linear) of time-domain data. At this time, a piecewise constant voltage waveform assumption is considered for the recursive convolution of the rational function approximation of the Y parameter.

For simplicity, consider a one-pole model of a SISO system as

$$Y(s) = \frac{r}{s - p}. \tag{7.1}$$

In time domain, (7.1) can be expressed as

$$i(t) = L^{-1}[Y(s)] * v(t) = \int_0^t re^{p(t-\tau)} v(\tau) d\tau, \tag{7.2}$$

where $i(t)$ and $v(t)$ are the current and the voltage at the port.

The current at time $t_{m+1}$ can be expressed as

$$\begin{aligned} i(t_{m+1}) &= \int_0^{t_m} re^{p(t_{m+1}-\tau)} v(\tau) d\tau + \int_{t_m}^{t_{m+1}} re^{p(t_{m+1}-\tau)} v(\tau) d\tau \\ &= e^{p\Delta t} \int_0^{t_m} re^{p(t_m-\tau)} v(\tau) d\tau + \int_{t_m}^{t_{m+1}} re^{p(t_{m+1}-\tau)} v(\tau) d\tau, \end{aligned} \tag{7.3}$$

when the time-interval is $\Delta t$. Because a piecewise constant voltage waveform is assumed, $v(t) = v(t_{m+1})$ for $t_m < t \le t_{m+1}$. Then, we can obtain the following recursive form for $i(t_{m+1})$:

$$i(t_{m+1}) = e^{p\Delta t} i(t_m) + v(t_{m+1}) \frac{r(1 - e^{p\Delta t})}{p}. \tag{7.4}$$

Equation (7.4) can be rewritten as

$$i(t_{m+1}) = I_{eq}(t_{m+1}) + v(t_{m+1}) G_{eq}, \tag{7.5}$$

where $I_{eq}(t_{m+1}) = e^{p\Delta t} i(t_m)$ and $G_{eq} = \frac{r(1 - e^{p\Delta t})}{p}$.

The basic concept for the recursive convolution and its time-domain model is presented for a SISO system. Extension to a MIMO system is discussed at length in [64-65].

## 7.2 Equivalent Circuit Synthesis of Rational Function Fit of Y Parameter

Among various equivalent circuit synthesis methods [16, 23, 33, 38, 43, 66, 67], two methods in [38, 66] are presented in this section. In [23], the authors generated an equivalent circuit for each passive partial term in the rational function fit obtained. However, the partial terms in the rational function fit can be nonpassive even in a passive macromodel. The non-passive terms generate negative values for lumped elements in the equivalent circuit, which prevent the circuit from being executable in HSPICE.

First, we present the circuit synthesis method in [38] which modifies nonpassive partial terms to make them passive by adding compensating terms. Second, the LAPLACE element serves as the alternative method without concerning the negative value of the lumped element [66].

### 7.2.1 Lumped circuit realization

It is assumed that the DUT is a passive $N_p-$port system represented by rational function matrix $\boldsymbol{Y}(s)$ of its admittance matrix. The generalized mathematical representation of the element $(i, j)$ of $\boldsymbol{Y}(s)$, considering different sets of poles for each element, can be written as

$$I_i(s) = Y_{ij}(s)V_j(s) = \left\{ sE_{ij} + D_{ij} + \sum_{m=1}^{N_{rij}} \frac{B_{ijm}}{s - p_{ijm}} + \sum_{m=1}^{N_{cij}} \left( \frac{C_{ijm}}{s - q_{ijm}} + \frac{\overline{C}_{ijm}}{s - \overline{q}_{ijm}} \right) \right\} V_j(s) \,. \quad (7.6)$$

In Equation (7.6), the terms associated with real poles and residues, and $p_{ijm}$ and $B_{ijm}$, $m = 1, 2, \ldots, N_{rij}$, and the terms associated with the pair of complex conjugate poles

and residues, $q_{ijm} = -\sigma_{ijm} + j\omega_{ijm}$ and $C_{ijm} = \alpha_{ijm} + j\beta_{ijm}$, $m = 1, 2, \ldots, N_{cij}$, with $1 \le i, j \le N_p$ are shown separately. When all the poles are forced to be stable, the following conditions hold:

$$\begin{aligned} p_{ijm} &< 0, \quad m = 1,2,\ldots,M_r \\ \sigma_{ijm} &> 0, \quad m = 1,2,\ldots,M_c. \end{aligned} \tag{7.7}$$

The circuit synthesis of (7.6) can be realized through the connection of dependent current sources at the ports for each partial term in (7.6) as shown in Figure 7.1(a).

The first order term of *s* can be realized using a current-controlled current source, where the controlling current flows through a capacitor of $|E_{ij}|$ which is connected across a dependent voltage source $V_j(s)$ with amplitude sign($E_{ij}$). Figure 7.1(b) shows the circuit for the first order term.

The constant term in (7.6) can be considered as a linear current-controlled current source, where the controlling current is the current through a conductance of 1 Ω with the voltage $V_j(s)$ of amplitude $D_{ij}$ connected across it. In Figure 7.1(c), the circuit realization of the constant term for admittance (7.6) is shown.

Each real pole term in (7.6) can be synthesized in terms of a linear current controlled source, where the controlling current is the current flowing through an inductor of 1 H in series with a resistor of value $-p_m$ Ω, with the voltage $V_j(s)$ with coefficient $B_{ijm}$ connected across them. In view of the condition in (7.6), the resistor in this subcircuit is positive. The circuit realization for the real pole term is presented in Figure 7.1(c).

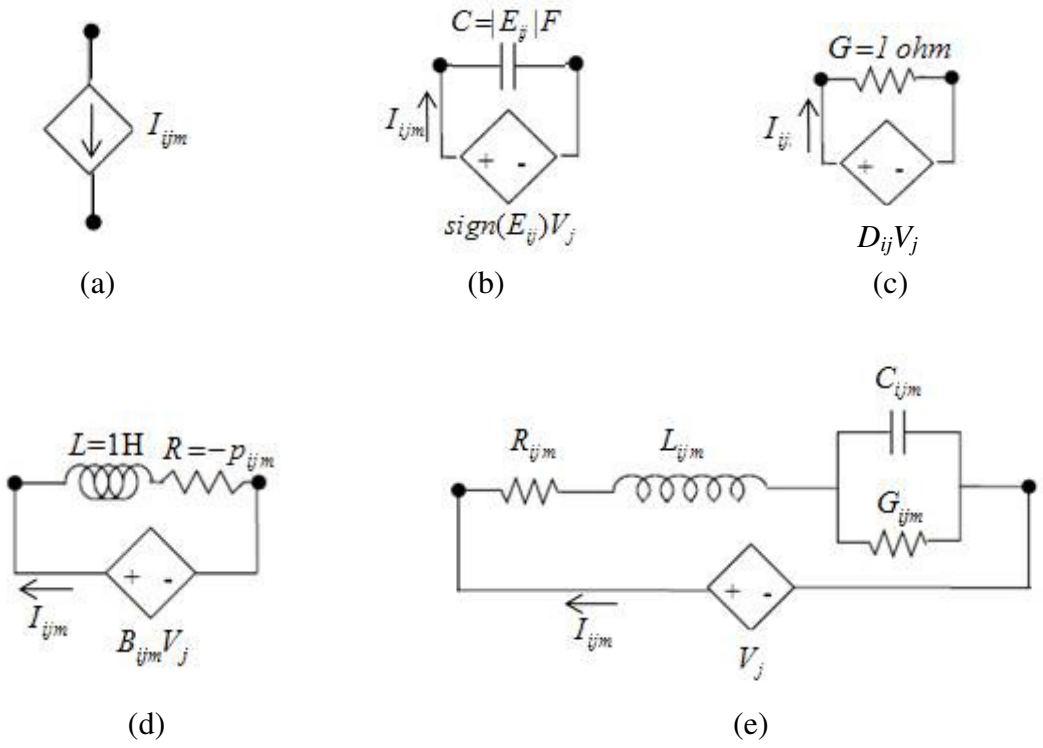



**Figure 7.1** Circuit realization of (a) current source at port *i*, (b) the first order term of *s*, (c) the constant term, (d) a real pole term, and (e) a complex-conjugate pole term for the admittance in (7.6).

Each pair of the complex conjugate poles in (7.6) can be written in the following form:

$$G_{ijm}(s) = \frac{2\alpha_{ijm}s + 2(\alpha_{ijm}\sigma_{ijm} - \beta_{ijm}\omega_{ijm})}{s^2 + 2\alpha_{ijm}s + \left|q_{ijm}\right|^2} = \frac{\gamma_1^{(ijm)}s + \gamma_0^{(ijm)}}{s^2 + \delta_1^{(ijm)}s + \delta_0^{(ijm)}}, \tag{7.8}$$

where the following quantities have been introduced:

$$\gamma_0^{(ijm)} = 2(\alpha_{ijm}\sigma_{ijm} - \beta_{ijm}\omega_{ijm}),\ \gamma_1^{(ijm)} = 2\alpha_{ijm},\ \delta_0^{(ijm)} = \left|q_{ijm}\right|^2,\ \delta_1^{(ijm)} = 2\alpha_{ijm}. \tag{7.9}$$

For ensuring all the lumped elements in the subcircuit positive in this text, $G_{ijm}(s)$ should be a positive real function for $s = j\omega$ and it requires the following condition to be satisfied by the coefficient $\gamma_1^{(ijm)}$, $\gamma_0^{(ijm)}$, and $\delta_1^{(ijm)}$:

$$\gamma_1^{(ijm)}\delta_1^{(ijm)} \geq \gamma_0^{(ijm)} \geq 0. \tag{7.10}$$

An alternative form of the above constraint equation can be obtained by utilizing (7.7) and (7.8) and making use of (7.6) and the fact that $\omega_{ijm}$ is positive. The resulting constraint equation is as follows:

$$\frac{\alpha_{ijm}}{\left|\beta_{ijm}\right|} \geq \frac{\omega_{ijm}}{\sigma_{ijm}}. \tag{7.11}$$

Therefore, the circuit realization of the pair of complex conjugate pole terms for admittance is given by

$$G_{ijm}(s) = \frac{K_{ijm} + sC_{ijm}}{L_{ijm}C_{ijm}s^2 + (K_{ijm}L_{ijm} + R_{ijm}C_{ijm})s + (1 + R_{ijm}K_{ijm})} \tag{7.12}$$

$$Y_{ijm}(s)=\frac{\dfrac{s}{L_{ijm}}+\dfrac{K_{ijm}}{C_{ijm}L_{ijm}}}{s^2+\left(\dfrac{K_{ijm}}{C_{ijm}}+\dfrac{R_{ijm}}{L_{ijm}}\right)s+\left(\dfrac{K_{ijm}}{C_{ijm}}\dfrac{R_{ijm}}{L_{ijm}}+\dfrac{1}{C_{ijm}L_{ijm}}\right)}.$$

Hence, the circuit of Figure 7.1(e) provides for the circuit realization of (7.12) for the complex conjugate pole term in admittance rational function approximation.

It is a matter of simple algebra to show that the values of the circuit elements are obtained in terms of the coefficients of the numerator and denominator polynomials of (7.8) as follows:

$$\begin{aligned}
L_{ijm}&=\frac{1}{\gamma_1^{(m)}},\quad R_{ijm}=\frac{\gamma_1^{(ijm)}\delta_1^{(ijm)}-\gamma_0^{(ijm)}}{(\gamma_1^{(m)})^2}\\
C_{ijm}&=\frac{(\gamma_1^{(ijm)})^3}{(\gamma_1^{(m)})^2\delta_0^{(m)}-(\gamma_1^{(ijm)}\delta_1^{(ijm)}-\gamma_0^{(ijm)})\gamma_0^{(ijm)}}\\
K_{ijm}&=\frac{\gamma_0^{(ijm)}(\gamma_1^{(ijm)})^2}{(\gamma_1^{(ijm)})^2\delta_0^{(ijm)}-(\gamma_1^{(ijm)}\delta_1^{(ijm)}-\gamma_0^{(ijm)})\gamma_0^{(ijm)}}
\end{aligned}\quad . \tag{7.13}$$

All four elements are nonnegative provided that (7.11) holds.

Next the case when (7.11) is not positive real is considered. To show one possible way of dealing with such cases, let us rewrite (7.8) as follows:

$$G_{ijm}(s)=\underbrace{\left[\frac{(\alpha_{ijm}+\Delta_{ijm})+j\beta_{ijm}}{s-q_{ijm}}+\frac{(\alpha_{ijm}+\Delta_{ijm})-j\beta_{ijm}}{s-q_{ijm}^*}\right]}_{\hat{G}_{ijm}(s)}-\underbrace{\left[\frac{\Delta_{ijm}}{s-q_{ijm}}+\frac{\Delta_{ijm}}{s-q_{ijm}^*}\right]}_{\Delta G_{ijm}(s)}. \tag{7.14}$$

If $\Delta_{ijm}$ is taken to be positive and of values such that

$$\frac{\alpha_{ijm}+\Delta_{ijm}}{|\beta_{ijm}|}\geq\frac{\omega_{ijm}}{\sigma_{ijm}}, \tag{7.15}$$

then, according to (7.11), the rational functions $\hat{G}_{ijm}(s)$ and $\Delta G_{ijm}(s)$ in (7.14) are positive real for $s = j\omega$, and they can be realized in terms of the circuit of Figure 7.2(e) with all positive circuit element values. In this program code, $\Delta_{ijm}$ is chosen to be

$$\Delta_{ijm} = 2\left(\frac{\omega_{ijm}}{\sigma_{ijm}}\left|\beta_{ijm}\right| - \alpha_{ijm}\right). \tag{7.16}$$

From Equation (7.5), all the currents which flow to the load in each subcircuit are attached to output ports via current-controlled current sources in Figure 7.1(a) and the synthesis of the circuit network can be completed as shown in Figure 7.2. It is important to notice that the polarization of the dependent current sources relating to $\Delta G_{ijm}(s)$ should be reversed because of the minus sign in front of $\Delta G_{ijm}(s)$ in (7.14).

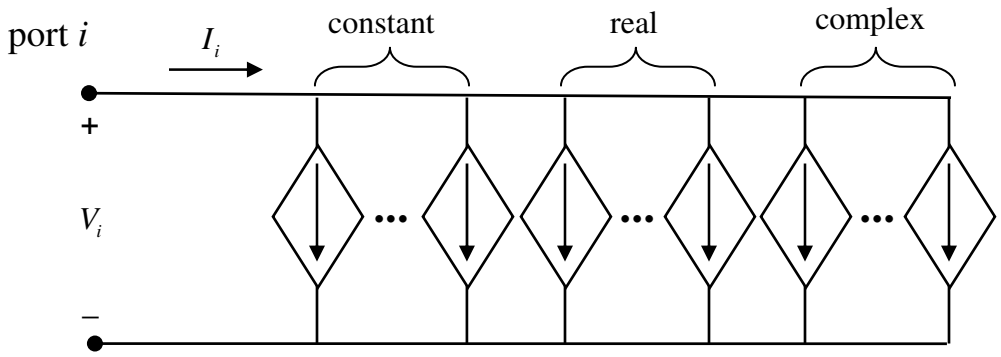



**Figure 7.2** Development of the SPICE netlist for the admittance matrix at port $i$, $1 \le i \le n$.

### 7.2.2 LAPLACE element realization

An arbitrary rational function representation of the admittance $Y_{ij}(s)$ as

$$Y_{ij}(s) = \frac{b_{ij}^{0} + b_{ij}^{1}s + ... + b_{ij}^{m}s^{m}}{a_{ij}^{0} + a_{ij}^{1}s + ... + a_{ij}^{n}s^{n}}, \tag{7.17}$$

can be represented in HSPICE netlist as transconductance,

$$G_{xxx}\ i+ \quad i- \quad LAPLACE \quad j+ \quad j- \quad b_{ij}^{0}, b_{ij}^{1}, ..., b_{ij}^{m} / a_{ij}^{0}, a_{ij}^{1}, ..., a_{ij}^{n} \tag{7.18}$$

where $i+$ and $i-$ are the positive and negative nodes of port *i* that the *G* element is connected to and from which the current flows; $j+$ and $j-$ are the positive and negative node of port *j* for the voltage input.

Equation (7.17) is rewritten in the summation of pole-residue terms as

$$Y_{ij}(s) = D_{ij} + \sum_{r=1}^{Nr}\frac{R_{r,ij}}{s - p_{r,ij}} + \sum_{c=1}^{Nc}\left(\frac{R_{c,ij}}{s - p_{c,ij}} + \frac{\overline{R}_{c,ij}}{s - \overline{p}_{c,ij}}\right) \tag{7.19}$$

where $N = 1 + Nr + Nc$. Equation (7.19) shows separately the terms with real poles and residues, $p_{r,ij}$, $R_{r,ij}$, and $r$=1,2,...,$N_r$, and the terms with complex-conjugate poles and residues, $p_{c,ij}$, $R_{c,ij}$, and $c$=1,2,...,$N_c$. Each term in (7.19) is represented in terms of the LAPLACE element, and connected as the circuit shown in Figure 7.3.

The constant term in (7.19) connected to port *i* is represented as

$$G_{xxx}\ i+ \quad i- \quad LAPLACE \quad j+ \quad j- \quad D_{ij}\,. \tag{7.20}$$

The real term in (7.19) is

$$G_{xxx}\ i+ \quad i- \quad LAPLACE \quad j+ \quad j- \quad R_{r,ij} / -p_{r,ij} 1. \tag{7.21}$$

And the complex pair is

$$G_{xxx}\,i+\;i-\;LAPLACE\;\;j+\;j-\;-(R_{c,ij}\bar{P}_{c,ij}+\bar{R}_{c,ij}P_{c,ij})(R_{c,ij}+\bar{R}_{c,ij})/|P_{c,ij}|^2\;-(P_{c,ij}+\bar{P}_{c,ij})\,1\,. \qquad (7.22)$$

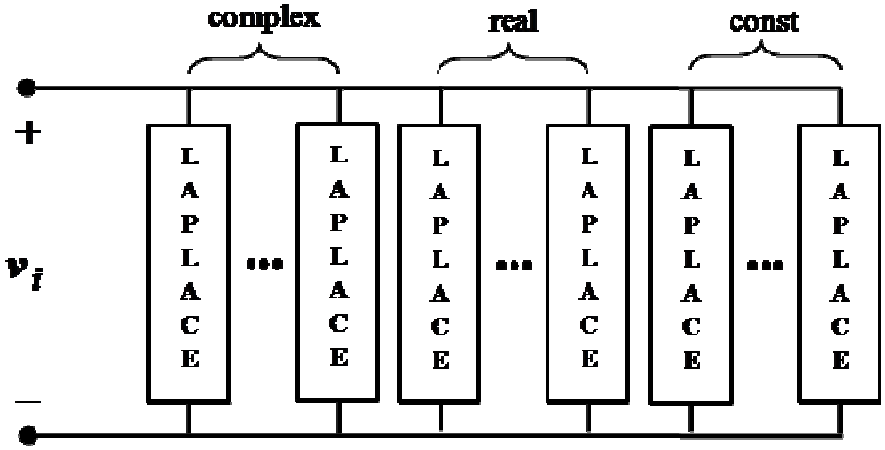



**Figure 7.3** HSPICE compatible equivalent circuit representation at port *i.*

## 7.3 Equivalent Circuit Synthesis of Delayed Rational Function Fit of S Parameter

The macromodeling method of the delayed rational function approximation using the S parameter was presented in Chapter 5. In this section, a new methodology for the synthesis of SPICE-compatible, delayed rational function approximation of the S parameter is presented. When the equivalent circuit for a macromodel of the S parameter is synthesized, special attention should be paid to its development because SPICE and other transient circuit simulators use the port voltage/current variable framework, while the S parameter is the ratio of transmitted (or reflected) to incident waves at the ports of the DUT.

It is assumed that the DUT is a passive $N_p-$port system; hence, its network representation is in terms of an $N_p$ x $N_p$ S parameter matrix, $\mathbf{S}(s)$. We are interested in the development of a SPICE-compatible, equivalent circuit realization of a delayed rational approximation for each element of the *S* parameter matrix as

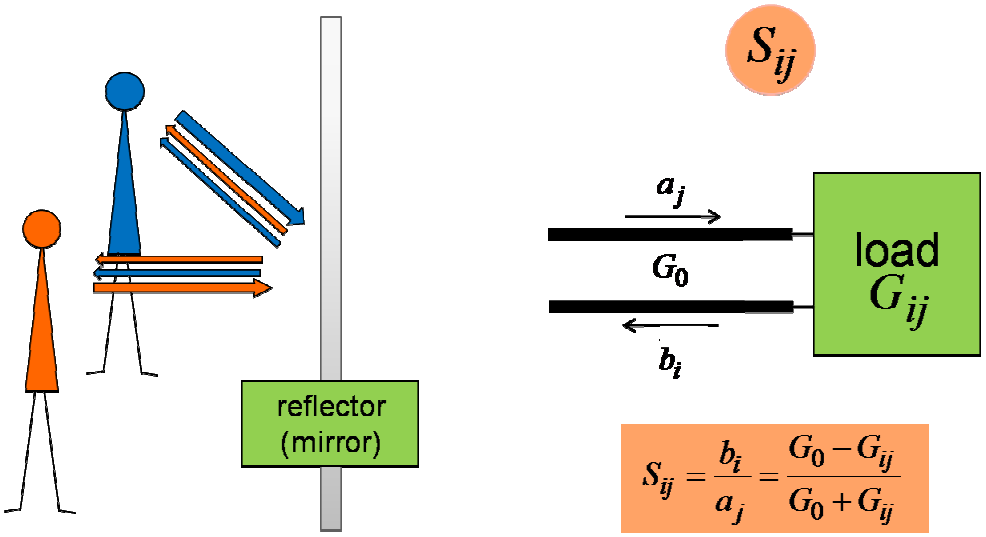
$$S_{ij}(s) = e^{-jt_{ij}s}\left( D_{ij} + \sum_{m=1}^{N} \frac{R_{m,ij}}{s - p_{m,ij}} \right). \tag{7.23}$$

In the above equation, *N* is the order of the rational approximation; $D_{ij}$, $p_{m,ij}$, and $R_{m,ij}$ are constants obtained through the rational fit following the extraction of the time constant $t_{ij}$, which is recognized as the transport delay between port *i* and port *j*, and $i, j = 1,2,...,N_p$.

### 7.3.1 Circuit synthesis

By definition, scattering parameters are ratios of outgoing and incident waves at the ports of the DUT. In Figure 7.4(a), two persons are looking at a mirror. When they can see each other in their positions, the self-image from the mirror explains the self scattering parameter, while the image of the other person explains the transfer scattering parameter. Our equivalent circuit synthesis is motivated by this concept. As the mirror reflects some portion of the incident light, the load is synthesized to reflect or transmit the incident wave with the portion of the scattering parameter. The admittance of the load is determined by

$$S_{ij} = \frac{\bar{V}_i^-}{\bar{V}_j^+} = \frac{G_0 - G_{ij}}{G_0 + G_{ij}} \tag{7.24}$$




(a) (b)

**Figure 7.4** Mirror/mirror images (a) vs. load/S parameters (b).

where $\bar{V}_j^+$ is the incident wave at port $j$, $\bar{V}_i^-$ is the transmitting or reflected voltage wave at port $i$, $G_{ij}$ is the admittance of a circuit for $S_{ij}$ presented in Figure 7.4(b), and $G_0$ is the characteristic admittance. When $i = j$, $S_{ij}$ is called the reflection coefficient. When $i \neq j$, $S_{ij}$ is the transfer coefficient.

Our equivalent circuit synthesis method is composed of two parts. One is to make the load on the basis of $S_{ij}$ and the other is to make a circuit that connects the incident/reflected wave variable framework of the S parameter with the port voltage/current variable framework of SPICE.

### 7.3.1.1 Synthesis of directional coupler

In the macromodel of the S parameter, traveling waves are used for variables; therefore, a circuit, like a directional coupler in measurement, is necessary to extract traveling waves from the port voltages and currents. The synthesis of the circuit, call it a directional coupler, is based on the definition of the port voltage and current in terms of the incident and reflecting waves,

$$\begin{aligned} V_i &= \bar{V}_i^+ + \bar{V}_i^- \\ \bar{I}_i &= \bar{I}_i^+ + \bar{I}_i^- = (\bar{V}_i^+ - \bar{V}_i^-)/Z_{i0} \end{aligned} \tag{7.25}$$

where $V_i$, $\bar{I}_i$ are respectively the voltage and the current at port $i$. From Equation (7.25), the traveling voltage waves can be derived as

$$\begin{aligned} \bar{V}_i^+ &= (V_i + Z_{i0}\bar{I}_i)/2 = V_i - \bar{V}_i^- \\ \bar{V}_i^- &= (V_i - Z_{i0}\bar{I}_i)/2 = V_i - \bar{V}_i^+ . \end{aligned} \tag{7.26}$$

The circuit representation of (7.26) is realized using controlled voltage sources in SPICE as shown in Figure 7.5.

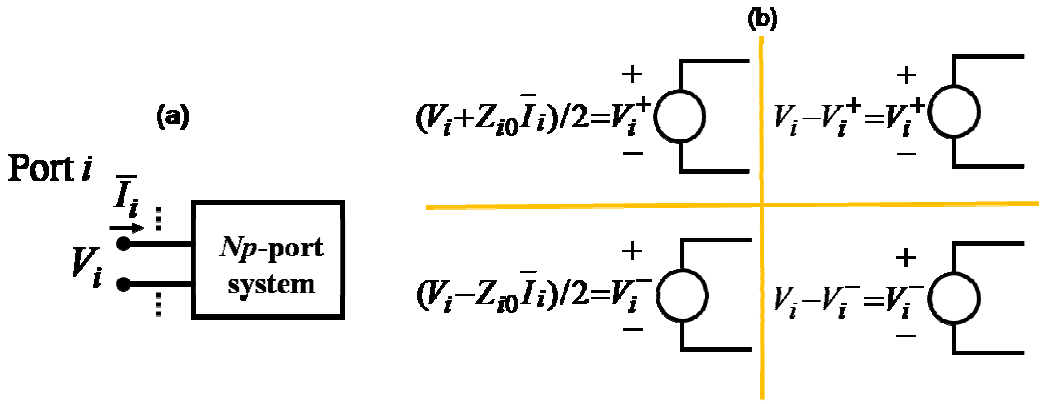



**Figure 7.5** Circuit representation of a directional coupler. (a) Port voltages and currents, and (b) couplers.

### 7.3.1.2 Synthesis of the load

$S_{ij}$ is the ratio of the reflected wave at port $i$ $\bar{V}_i^-$ to the incident voltage wave at port $j$ $\bar{V}_j^+$. Hence Equation (7.24) can be rewritten as

$$\begin{aligned}\bar{V}_i^- &= \sum_{j=1}^{Np}\bar{V}_{ij}^- = \sum_{j=1}^{Np}S_{ij}\bar{V}_j^+ = \sum_{j=1}^{Np}e^{-t_{ij}s}\left(D_{ij}+\sum_{r=1}^{Nr}\frac{R_{r,ij}}{s-p_{r,ij}}+\sum_{c=1}^{Nc}\left(\frac{R_{c,ij}}{s-p_{c,ij}}+\frac{R_{c,ij}^*}{s-p_{c,ij}^*}\right)\right)\bar{V}_j^+ \\ &= \bar{V}_i^- = \sum_{j=1}^{Np}\left\{\sum_{m=1}^{Nt}S_{ijm}\bar{V}_j^+\right\} = \sum_{j=1}^{Np}\left\{\sum_{m=1}^{Nt}e^{-t_{ij}s}\tilde{S}_{ijm}\bar{V}_j^+\right\} = \sum_{j=1}^{Np}\left\{\sum_{m=1}^{Nt}\bar{V}_{ijm}^-\right\},\end{aligned} \tag{7.27}$$

where $Nt = 1+Nr+Nc$. In the above, the rational function in (7.23) is rewritten to show separately the terms with real poles and residues, $p_{r,ij}$, $R_{r,ij}$, $r$=1,2,...,$N_r$, and the terms with complex-conjugate poles and residues, $p_{c,ij}$, $R_{c,ij}$, $c$=1,2,...,$N_c$. $S_{ijm}$, $m$=1,2,...,$N_t$, is the partial term in $S_{ij}$, and $\tilde{S}_{ijm}$ is the rational function part of $S_{ijm}$. In this manner, $\tilde{S}_{ijm}$ is presented as the simple rational function, which means the real coefficient rational function with the smallest order. The form in (7.27) facilitates the synthesis of an equivalent circuit for the calculation of the reflected wave at its port, through the separate consideration of each "partial" reflection term $S_{ijm}$. $S_{ijm}$ is represented by the delay and the admittance of the load, $G_{ijm}$. If $S_{ij}$ is directly put into (3.13), $G_{ij}$ becomes too complicated to benefit from the rational function fit, which can be readily converted into a SPICE compatible circuit.

The whole circuit is synthesized in two steps. First, a load is synthesized to reflect the incident wave $\bar{V}_j^+$ to the amount of $\bar{V}_{ijm}^-$ at port $i$ with the ratio of $S_{ijm}$. Then the

voltage source is connected to the load to assign $\bar{V}_j^+$. The reflected waves of $\bar{V}_{ijm}^-$ are summed for all *j* and *m* indices to make the whole supposed reflected wave at port *i* for $S_{ij}$ using directional couplers, which were described in the previous section. In this chapter, one of those possible circuit configurations for $S_{ijm}$ is suggested in Figure 7.6. The delay term in $S_{ijm}$ is realized using a lossless transmission line, and a load is synthesized to match the rational function part, $\tilde{S}_{ijm}$. The length of the lossless transmission line $l_{ij}$ is

$$l_{ij} = t_{ij} \cdot v_p / 2 \tag{7.28}$$

with characteristic admittance $G_{i0}$. For simplicity and without loss of generality $G_{i0}$ will be replaced by $G_0$, which means that all the characteristic admittances at ports are same. The load is represented by $G_{ijm}$ from

$$\tilde{S}_{ijm} = \frac{G_0 - G_{ijm}}{G_0 + G_{ijm}}. \tag{7.29}$$

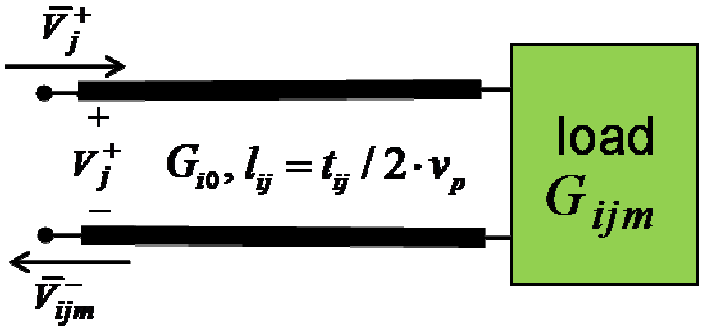



**Figure 7.6** Circuit representation to generate $\bar{V}_{ijm}^-$ for $S_{ijm}$.

For a constant term in $\tilde{S}_{ijm}$, $G_{ijm}$ can be derived as

$$\tilde{S}_{ijm} = D_{ij} = \frac{G_0 - G_{ijm}}{G_0 + G_{ijm}}, \text{ when } m = 1 \tag{7.30}$$

$$G_{ijm} = \frac{-D_{ij} + 1}{D_{ij} + 1} G_0 = const, \text{ when } m = 1, \tag{7.31}$$

and represented in the HSPICE netlist as transconductance,

$$G_{xxx} \quad i+ \quad i- \quad \text{LAPLACE} \quad j+ \quad j- \quad \text{const}, \tag{7.32}$$

where *i*+ and *i*- are the positive and the negative nodes on which the load of $G_{ijm}$ is placed. For the real pole term in $\tilde{S}_{ijm}$,

$$G_{ijm} = \frac{s - R_{r,ij} - p_{r,ij}}{s + R_{r,ij} - p_{r,ij}} G_0 \tag{7.33}$$

and its netlist is

$$G_{xxx} \quad i+ \quad i- \quad \text{LAPLACE} \quad j+ \quad j- \quad (-R_{r,ij}G_0 - p_{r,ij}G_0),\ Y_0 \ /\ (R_{r,ij} - p_{r,ij}),\ 1. \tag{7.34}$$

Finally, for a complex pole pair, $G_{ijm}$ is derived as

$$G_{ijm} = \frac{k_0 + k_1 s + s^2}{d_0 + d_1 s + s^2} G_0 \tag{7.35}$$

where

$p_{c,ij} = -\sigma_{c,ij} + j\omega_{c,ij}$, $R_{c,ij} = \alpha_{c,ij} + j\beta_{c,ij}$, $k_0 = \omega_{c,ij}^2 + \sigma_{c,ij}^2 - 2(\alpha_{c,ij}\sigma_{c,ij} - \beta_{c,ij}\omega_{c,ij})$,

$k_1 = 2(\sigma_{c,ij} - \alpha_{c,ij})$, $d_0 = \omega_{c,ij}^2 + \sigma_{c,ij}^2 - 2(\alpha_{c,ij}\sigma_{c,ij} - \beta_{c,ij}\omega_{c,ij})$, and $d_1 = 2(\sigma_{c,ij} + \alpha_{c,ij})$.

Hence the netlist is

$$G_{xxx} \quad i+ \quad i- \quad \text{LAPLACE} \quad j+ \quad j- \quad k_0G_0, k_1G_0, G_0 \ /\ d_0,\ d_1,\ 1. \tag{7.36}$$

Figure 7.7 depicts how the voltage at port *i* is obtained as the sum of the incident voltage and all the partial reflected waves. $\bar{V}_j^+$ is extracted using a directional coupler, doubled, and assigned to a voltage source with a source resistor $Z_0$, which is the characteristic impedance at port *i*. $\bar{V}_{ijm}^-$ is obtained using the directional coupler. Then $\bar{V}_{ijm}^-$ is summed for all *j* and *m* indices to give $\bar{V}_i^-$, which is attached to port *i* with the incident wave $\bar{V}_j^+$ shown in Figure 7.5. $\bar{V}_j^+$ is doubled at a source for each load so that its value can be safely assigned to the load with the matched source impedance.

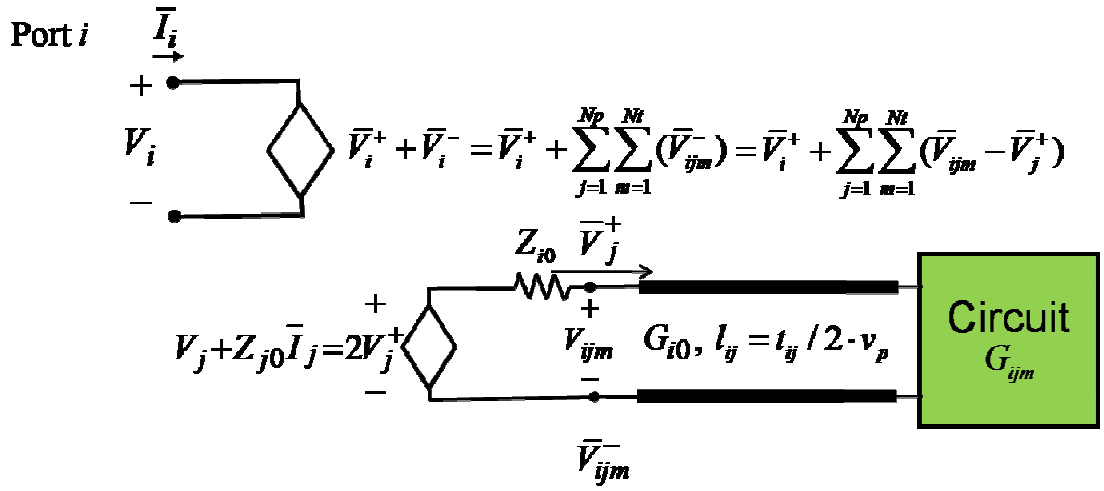



**Figure 7.7** Equivalent circuit representation for the calculation of the voltage at port *i*.

## 7.4 Validation Studies

In this section, two examples are considered to demonstrate the validity and accuracy of the proposed method

### 7.4.1 Four-conductor stripline

First, a four-conductor stripline characterized by S-parameter data over the frequency range from 10 MHz to 10 GHz was modeled. The cross-sectional geometry and the relevant dimensions of the stripline are shown in Figure 7.8; the unit of dimension is the micron. The length of the stripline is 20 cm. PEC (perfect electric conductor) is used for returning paths, and four conductors of copper are placed in a 100 μm layer of dielectric, which has a relative permittivity of 3.9 and a loss tangent of zero.

For evaluating frequency-domain data from the stripline, UIUC2D [68] was used to generate the SPICE-compatible per-unit-length equivalent circuit. UIUC2D, the extractor used, has the capability of synthesizing a SPICE-compatible equivalent

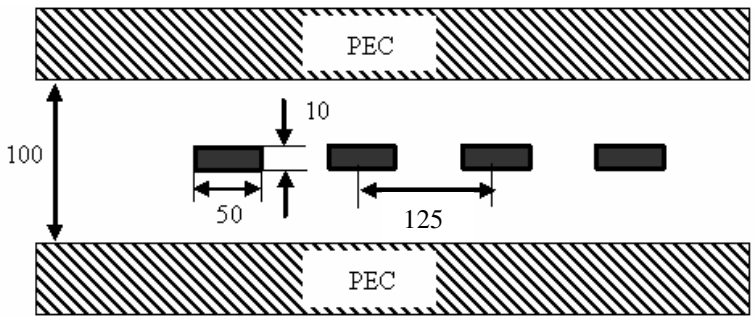
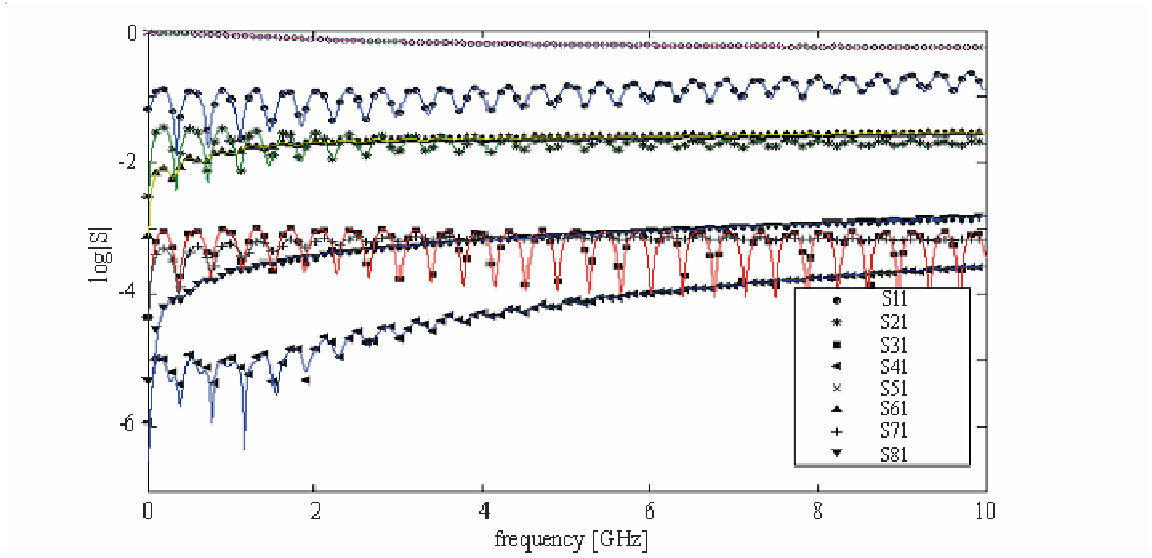



**Figure 7.8** Circuit configurations. (a) Cross-sectional geometry and the dimensions of a four-conductor stripline. All dimensions are in microns. The PEC grounds are placed up and down. The length is 20 cm.

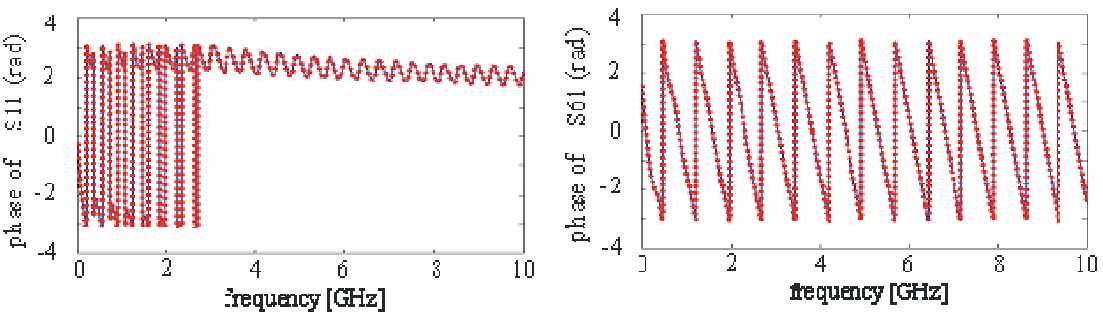
circuit representation of the multiconductor interconnect system, which accurately captures frequency-dependent p.u.l. parameters over a prescribed frequency bandwidth.

The scattering parameter values were obtained using the AC analysis of HSPICE. The number of frequency data which were linearly collected over the frequency range was 201. To obtain the transport delay, a Gaussian pulse with a 20 dB bandwidth at 10 GHz was assigned to one port, and all the ports were terminated with the characteristic impedance of 50 Ω. Peak-to-peak delays were measured at other ports from the transient simulation of HSPICE. The delays between near-end (port 1,3,5,7) and far-end (port 2,4,6,8) ports were computed as 1.265 ns. Both the frequency data and the delays were put into the delayed rational function approximation, which fitted the S parameter element by element to the rational function using VF after delay extraction. The order $N$ of VF can be set differently for each element of the S parameter, but 60 was assigned for all the elements at this time.

From the generated delayed rational function approximation, the SPICE-compatible equivalent circuit via the proposed method was synthesized and simulated in HSPICE. The scattering parameters of the equivalent circuit obtained from the proposed method are plotted in Figure 7.9 and compared with the reference values which were obtained from UIUC2D and depicted as solid lines. In Figure 7.9(a), the magnitudes of the first column of the scattering matrix are plotted and they show very good agreement. The phases of $S_{11}$ and $S_{16}$ are only presented in Figure 7.9(b) for simplicity, and they show very good agreement also.




(a)




(b)

**Figure 7.9** Comparison between reference values and data from the equivalent circuit generated via the proposed method. (a) Magnitudes of the S parameters from $S_{11}$ to $S_{61}$ in dB, (b) phases of the S parameters $S_{11}$ and $S_{61}$. Solid line: reference values; dotted line: values form the equivalent circuit synthesized via the proposed method.

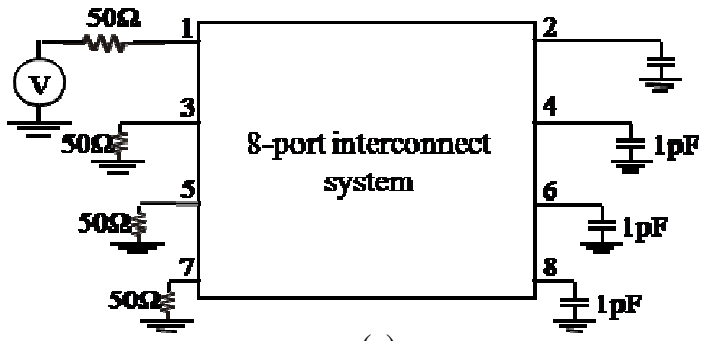
The generated equivalent circuit was terminated with resistors at the near ends and capacitors at the far ends as shown in Fig. 7.10(a). Unit pulse responses were obtained, when the rise time of the unit pulse that was assigned at port 1 was 0.1 ns. Voltages at ports 1 and 6 are plotted as dotted lines and compared with reference values in Figure 7.10 (b) and (c), respectively. The reference values were also obtained from the equivalent circuit of UIUC2D and are depicted as solid lines. Once again, very good agreement is observed between the two sets of results. The two sets of results are almost indistinguishable.

### 7.4.2 Coupled transmission lines

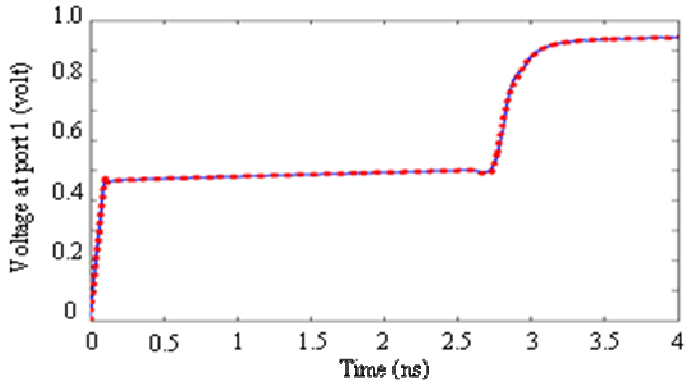
An equivalent circuit for the delayed rational function fit of the coupled transmission line presented in Chapter 5 was generated by means of the proposed method.

A frequency sweep (AC analysis) in SPICE was then used to calculate the S parameter of the generated equivalent circuit. For reference values, the frequency data used for the delayed rational function fitting were used for demonstrating the accuracy of the proposed method. The magnitude and phase of S parameter data are plotted in dotted lines in Figure 7.11(a) and (b), respectively, and compared with reference values. Very good agreements are observed.

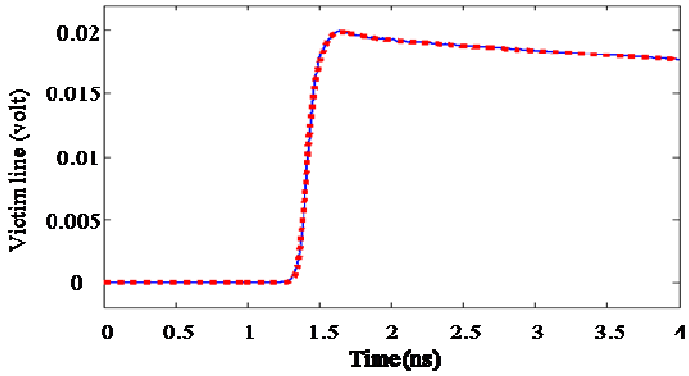
The transient analysis was executed using an input signal switching from 0 to 1 V in 0.1 ns when the circuit is terminated with resistors at the near-end ports and capacitors at the far-end ports as shown in Figure 7.12(a). For reference values, we




(a)

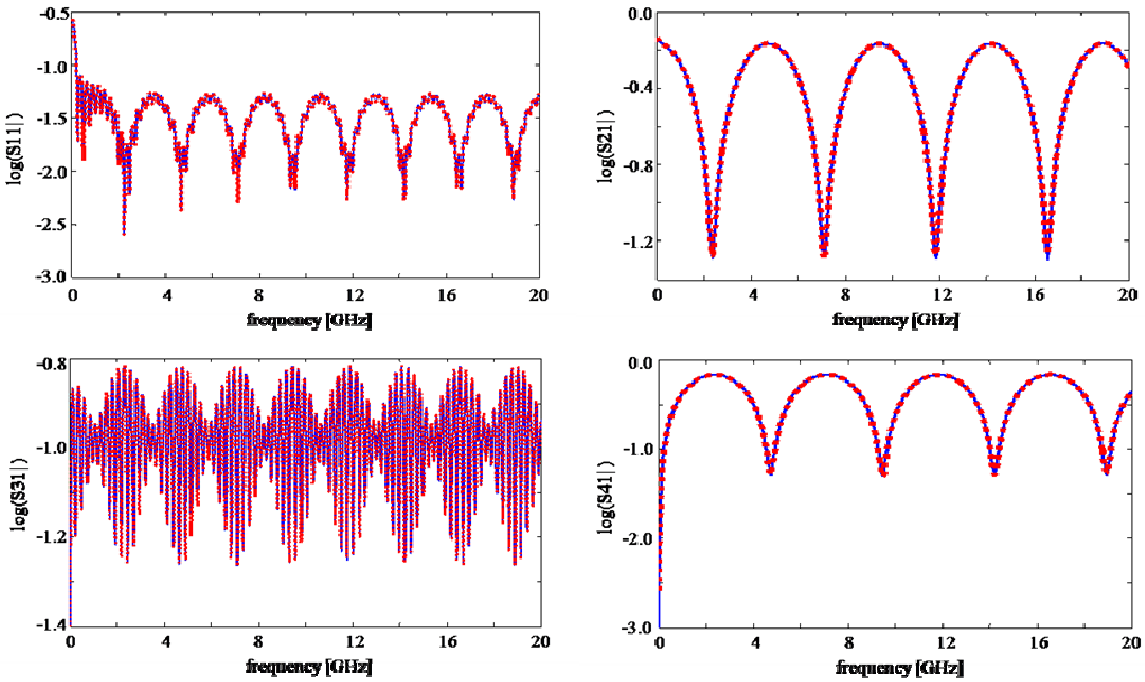



(b)



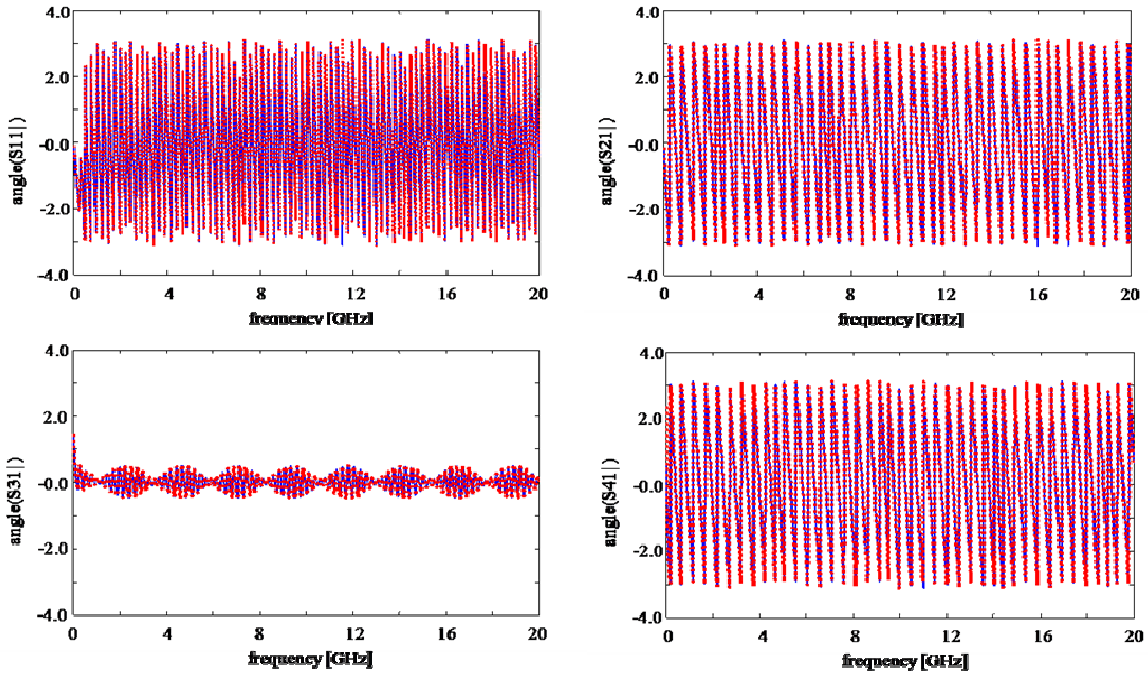

(c)

**Figure 7.10** (a) A circuit configuration for step response, and the comparison between step response from the equivalent circuit and the reference values (b) at port 1 and (c) at port 6. Solid line: reference values; dotted line: values from the equivalent circuit synthesized via the proposed method.



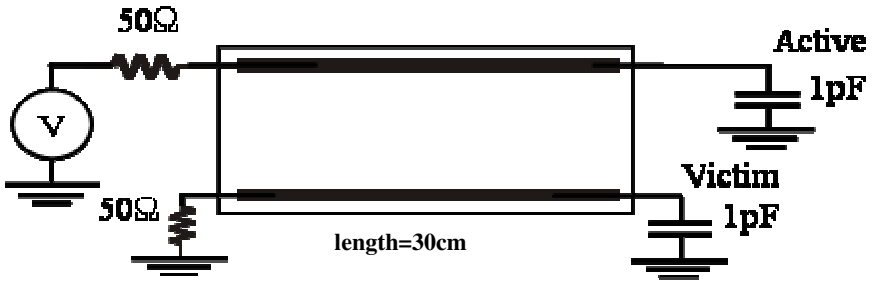

(a)

**Figure 7.11** Comparison between reference values and data from the equivalent circuit. (a) Magnitudes (in log) and (b) phases (in radians) of the S parameters from $S_{11}$ to $S_{41}$. Solid line: reference values; dotted line: values from the equivalent circuit synthesized via the proposed method.

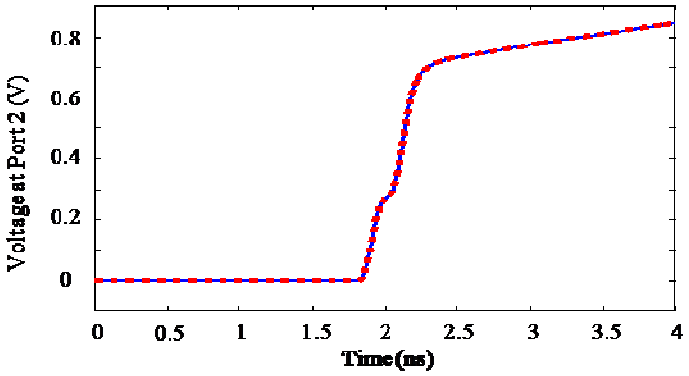



(b)

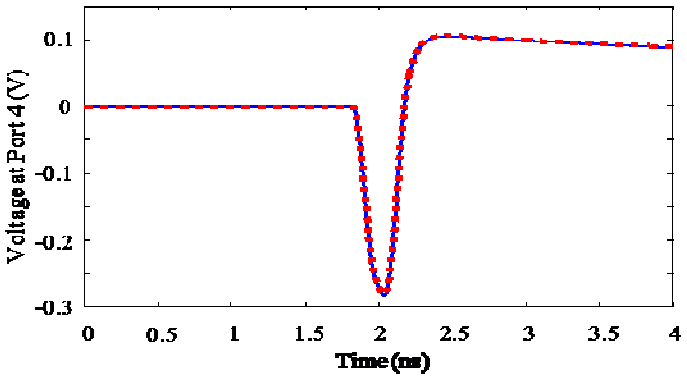
**Figure 7.11** Continued.




(a)




(b)




(c)

**Figure 7.12** (a) A circuit configuration for step response and comparison between step response from the equivalent circuit and the reference values (b) at port 2 and (c) at port 4. Solid line: reference values; dotted line: values from the equivalent circuit synthesized via the proposed method.

utilized the *W* element in SPICE using per-unit-parameters presented in Section 5.6.1. The step responses at port 2 and port 4 from the generated equivalent circuit are plotted and compared with the reference values in Figure 7.12(b) and (c), respectively. Very good agreements are observed also.

## 7.5 Summary

In this chapter, a SPICE-compatible equivalent circuit synthesis method of delayed rational function approximation of S parameters of passive multiports was presented. The presented circuit synthesis method was demonstrated through its application to the equivalent circuit synthesis for multiconductor transmission line networks.

# CHAPTER 8
# SUMMARY AND FUTURE WORK

## 8.1 Summary

The outcome of this research is a set of methodologies and their computer implementation for the computationally efficient generation of accurate rational function approximations of broadband electromagnetic responses of linear, passive, high-speed interconnect systems, and the subsequent interpretation of these rational functions in terms of SPICE-compatible equivalent circuits.

One of the new methods concerns the generation of a rational function approximation utilizing both time-domain and frequency-domain data. This is accomplished by combining the frequency-domain vector fitting (VF) process and its time-domain counterpart, namely, the time-domain vector fitting (TDVF) process. The resulting, hybrid rational fitting process is named CRAFT (Combined Rational Approximation from Frequency-Domain and Time-Domain Data). One of the special attributes of CRAFT is that it provides for the complementary use of frequency-domain data and time-domain response data, obtained either through measurement or through numerical simulation, to generate a rational function interpolation of the response of the interconnect system that amounts to both extrapolation of the early-time, transient data used for the fitting to later-time response and extrapolation of the frequency-domain data used for the fitting to higher frequencies.

As part of the development of CRAFT we also proposed and demonstrated a guideline for estimating the order for the rational function fit from using time-domain

data only via TDVF. While a variety of guidelines had been proposed in the literature for selecting the order for the rational function fit using frequency-domain data, this was not the case in the context of TDVF. Our contribution helped rectify this situation. Furthermore, we took advantage of this guideline to recommend a way to estimate the order of a rational function fit generated using CRAFT.

We also proposed and demonstrated a scattering-parameter based rational function fitting scheme for causal electromagnetic responses that utilizes the extraction of the electromagnetic delay to reduce the order of the rational function fit and improve the accuracy of the generated delayed rational function interpolation. The delayed rational fit is generated from the measured or numerically obtained frequency data approximating the frequency data via VF after delay extraction. An important element of this contribution is our investigation of the importance of properly extracting the electromagnetic delay prior to the application of the rational function fitting, and the assessment of the reduction in the order of rational fit achieved through delay extraction. A methodology for the direct synthesis of a SPICE-compatible circuit representation of the fitted scattering parameters with delay extraction was also presented and validated.

In this dissertation, emphasis was placed on the implementation of a rational fitting process where the elements of the multiport network matrix representing the high-speed interconnect system are fitted one at a time. Despite the use of different sets of poles, one set per element, for such a fitting, this approach offers the advantage of improved numerical robustness of the rational fitting process and enhanced accuracy

in the generated rational fits for multiport systems that include both strongly coupled and weakly coupled ports. In order to provide for passivity enforcement, we modified the passivity enforcement method via quadratic programming in order to apply it to this element-by-element network matrix rational function fitting process.

## 8.2 Future Work

In Chapter 5, we demonstrated the benefits resulting from extracting the delay from the electromagnetic transfer function prior to rational function fitting. However, if there are persistent multiple reflections in the response, the benefits from such delay extraction become questionable. Use of scattering parameters was motivated by the desire to make sure that the magnitude of multiple reflections is sufficiently low for the methodology to be applicable with acceptable accuracy. However, if this is not the case, the proposed methodology needs to be modified to explore ways in which multiple reflections can be accommodated in the context of rational function fitting.

Also, for the extraction of interconnect delay, we relied on the calculation of the inverse Fourier transform. Such an approach provides only a rough estimate of the delay, and that required the careful restriction of the delay to a value less than the actual delay to avoid deterioration of accuracy in the generation of the rational function fit. Therefore, a more accurate delay estimation method needs to be developed.

Also, in the context of rational function fitting of scattering parameters with delay extraction, no method has been developed for passivity enforcement of the generated

delayed rational function. Development of such an approach is recommended for future work.

Finally, we observe that the accuracy and robustness of any rational function fitting process is strongly dependent on the quality of the input data. More specifically, the causality and passivity of the data used are important in generating causal and passive rational fits. Future work should pursue ways to check both the causality and the passivity of the input data, as well as methodologies for noncausal and/or nonpassive data to be rendered causal and passive through data preprocessing.

# REFERENCES


[1] R. Achar and M. Nakhla, "Simulation of high-speed interconnects," *Proc. IEEE*, vol. 89, pp. 693-728, May 2001.

[2] A. E. Ruehli and A. C. Cangellaris, "Progress in the methodologies for the electrical modeling of interconnects and electronic packages," *Proc. IEEE*, vol. 89, pp. 740-771, May 2001.

[3] P. D. Smith, "Instabilities in time marching methods for scattering: Cause and rectification," *Electromagn.*, vol. 10, pp. 439-451, 1990.

[4] C. Paul, *Analysis of Multiconductor Transmission Line Structures*. New York, NY: Wiley, 1993.

[5] F. H. Branin, "Transient analysis of lossless transmission lines," *Proc. IEEE*, vol. 55, pp. 2012-2013, Nov. 1967.

[6] F. Y. Chang, "The generalized method of characteristics for waveform relaxation analysis of lossy coupled transmission lines," *IEEE Trans. Microw. Theory Tech.*, vol. 37, pp. 2028-2038, Dec. 1989.

[7] S. Grivet-Talocia and F. Canavero, "TOPLine: A delay-pole-residue method for the simulation of lossy and dispersive interconnects," in *Proc. IEEE 11th Topical Meeting on EPEP*, Oct. 2002, pp. 359-362.

[8] N. Nakhla, A. Dounavis, R. Achar, and M. Nakhla, "DEPACT: Delay extraction-based passive compact transmission line macromodeling algorithm," *IEEE Trans. Adv. Packag.*, vol. 28, pp. 13-23, Feb. 2005.

[9] K. Coperich, A. Ruehli, and A. Cangellaris, "Enhanced skin effect for partial-element equivalent circuit (PEEC) models," *IEEE Trans. Microw. Theory Tech.*, vol. 48, pp. 1435-1442, Sept. 2000.

[10] L. T. Pillage and R. A. Rohrer, "Asymptotic waveform evaluation for timing analysis," *IEEE Trans. Computer-Aided Design Integr. Circuits Syst.*, vol. 9, pp. 352-366, April 1990.

[11] P. Feldmann and R. W. Freund, "Efficient linear circuit analysis by Padé approximation via the Lanczos process," *IEEE Trans. Computer-Aided Design Integr. Circuits Syst.*, vol. 14, pp. 639-649, May 1995.

[12] A. E. Ruehli and H. Heeb, "Circuit models for three-dimensional geometries including dielectrics," *IEEE Trans. Microw. Theory Tech.*, vol. 40, pp. 1507-1516, July 1992.

[13] A. Odabasioglu, M. Celik, and L. T. Pileggi, "PRIMA: Passive reduced-order interconnect macromodeling algorithm," *IEEE Trans. Computer-Aided Design Integr. Circuits Syst.*, vol. 17, pp. 645-653, Aug. 1998.

[14] A. C. Cangellaris, M. Celik, S. Pasha, and L. Zhao, "Electromagnetic model order reduction for system level modeling," *IEEE Trans. Microw. Theory Tech.*, vol. 47, pp. 840-850, June 1999.

[15] A. C. Cangellaris and L. Zhao, "Model order reduction techniques for electromagnetic macromodeling based on finite methods," *Int. J. Numer. Model. Electron. Netw. Devices Fields*, vol. 13, pp. 181-197, March 2000.

[16] M. J. Choi and A. C. Cangellaris, "A quasi-three-dimensional distributed electromagnetic model for complex power distribution networks," *IEEE Trans. Adv. Packag.*, vol. 25, pp. 28-34, Feb. 2002.

[17] R. A. Ruehli, H. Heeb, E. Bracken, and R. Rohrer, "Three dimensional circuit oriented electromagnetic modeling for VLSI interconnects," in *Proc. Packaging, Interconnects, Optoelectronics for the Design of Parallel Computers Workshop*, March 1992, pp. 218-221.

[18] L. M. Silveira, M. Kamon, and J. White, "Direct computations of reduced-order models for circuit simulation of 3D interconnect structures," in *Proc. IEEE 3rd Topical Meeting EPEP*, Nov. 1994, pp. 245-248.

[19] R. W. Freund and P. Feldmann, "Efficient small-signal circuit analysis and sensitivity computations with the PVL algorithm," in *Proc. IEEE Int. Conf. Computer-Aided Design*, Nov. 1994, pp. 404-411.

[20] K. Gallivan, E. Grimme, and P. Van Dooren, "A rational Lanczos algorithm for model reduction," *Numer. Algorithms*, vol. 12, pp. 33-63, April 1996.

[21] J. Cullum, A. Ruehli, and T. Zhang, "Model reduction for PEEC models including retardation," in *Proc. IEEE 7th Topical Meeting EPEP*, Oct. 1998, pp. 287-290.

[22] B. Gustavsen and A. Semlyen, "Rational approximation of frequency domain responses by vector fitting," *IEEE Trans. Power Del.*, vol. 14, pp. 1052-1061, July 1999.

[23] B. Gustavsen, "Computer code for rational approximation of frequency dependent admittance matrices," *IEEE Trans. Power Del.*, vol. 17, pp. 1093-1098, Oct. 2002.

[24] S. Grivet-Talocia, F. G. Canavero, I. S. Stievano, and I. A. Maio, "Circuit extraction via time-domain vector fitting," in *IEEE Int. Symp. on EMC,* Aug. 2004, pp. 1005-1010.

[25] C. Sanathanan and J. Koerner, "Transfer function synthesis as a ratio of two complex polynomials," *IEEE Trans. Autom. Control*, vol. AC-8, pp. 56-58, Jan. 1963.

[26] W. T. Beyene and J. E. Schutt-Ainé, "Efficient transient simulation of high-speed interconnects characterized by sampled data," *IEEE Trans. Compon., Packag., Manuf. Technol. B,* vol. 21, pp. 105-113, Feb. 1998.

[27] J. Morsey and A. C. Cangellaris, "Prime: Passive realization of interconnect models from measured data," in *Proc. IEEE 10th Topical Meeting EPEP*, Oct. 2001, pp. 230-232.

[28] R. Mandrekar and M. Swaminathan, "Causality enforcement in transient simulation of passive networks through delay extraction," in *Proc. IEEE Workshop on Signal Propag. on Interconnects*, May 2005, pp. 25-28.

[29] T. Hu, B. Zhong, S. L. Dvorak, and J. L. Prince, "Application of recursive convolution to transient simulation of interconnects using a hybrid phase-pole macromodel," *IEEE Trans. Adv. Packag.*, vol. 27, pp. 603-610, Nov. 2004.

[30] S. Moon and A. C. Cangellaris, "Rational function fitting of electromagnetic transfer functions from frequency-domain and time-domain data," in *IEEE MTT-S Int. Microwave Symp. Dig.*, June 2006, pp. 1609-1612.

[31] S. Moon and A. C. Cangellaris, "Rational function fitting of electromagnetic transfer functions of interconnect structures via extrapolation in time and interpolation in frequency," in *Proc. Electron. Comp. Technol. Conf.*, May 2006, pp. 1251-1255.

[32] M. Yuan, T. K. Sarkar, B. H. Jung, Z. Ji, and M. Salazar-Palma, "Use of discrete Laguerre sequences to extrapolate wide-band response from early-time and low-frequency data," *IEEE Trans. Microw. Theory Tech.*, vol. 52, pp. 1740-1750, July 2004.

[33] S. Moon and A. C. Cangellaris, "SPICE-compatible representations of S-parameter matrices of passive networks with transport delay," in *Proc. Elec. Performance of Elect. Packag.*, Oct. 2007, pp. 59-62.

[34] P. Triverio, S. Grivet-Talocia, M. S. Nakhla, F. G. Canavero, and R. Achar, "Stability, causality, and passivity in electrical interconnect models," *IEEE Trans. Adv. Packag*., vol. 30, pp. 795-808, Nov. 2007.

[35] M. J. Choi and A. C. Cangellaris, "A quasi three-dimensional distributed electromagnetic model for complex power distribution networks," in *Proc. 51st Electron. Comp. and Technol. Conf.*, May 2001, pp. 1111-1116.

[36] D. Saraswat, R. Achar, and M. Nakhla, "Global passivity enforcement algorithm for macromodels of interconnect subnetworks characterized by tabulated data," *IEEE Trans. Very Large Scale Integr.* (*VLSI*) *Syst.*, vol. 13, pp. 819-832, July 2005.

[37] A. V. Oppenheim, R. W. Schafer, and J. R. Buck, *Discrete-Time Signal Processing,* 2nd ed. Upper Saddle River, NJ: Prentice Hall, 1999.

[38] A. Woo, "Passive rational fitting of a passive network transfer function from its real part," Ph.D. dissertation, University of Illinois at Urbana-Champaign, 2008.

[39] W. Hendrickx and T. Dhaene, "A discussion of 'Rational approximation of frequency domain responses by vector fitting'," *IEEE Trans. Power Syst.*, vol. 21, pp. 441-443, Feb. 2006.

[40] B. Gustavsen and A. Semlyen, "Enforcing passivity for admittance matrices approximated by rational functions," *IEEE Trans. Power Syst*., vol. 16, pp. 97-104, Feb. 2001.

[41] M. R. Whohlers, *Lumped and Distributed Passive Networks*. New York, NY: Academic Press, 1969.

[42] A. V. Oppenheim and A. S. Willsky, *Signals and Systems*. Englewood Cliffs, NJ: Prentice-Hall, 1983.

[43] E. A. Guillemin, *Synthesis of Passive Networks*. New York, NY: Wiley, 1957.

[44] D. Youla, L. Castriota, and H. Carlin, "Bounded real scattering matrices and the foundations of linear passive network theory," *IRE Trans. Circuit Theory*, vol. 6, pp. 102-124, March 1959.

[45] A. Semlyen and A. Dabuleanu, "Fast and accurate switching transient calculations on transmission lines with ground return using recursive convolutions," *IEEE Trans. Power App. Syst.*, vol. 94, pp. 561-571, March 1975.

[46] "Least squares methods in physics and engineering," lecture notes given in the academic training program of CERN, 1980-1981.

[47] Vector Fitting, March 2009. [Online]. Available: http://www.energy.sintef.no/produkt/VECTFIT/index.asp.

[48] M. T. Heath, *Scientific Computing: An Introductory Survey*, 2nd ed. New York, NY: McGraw-Hill, 2002.

[49] B. Gustavsen and A. Semlyen, "Application of vector fitting to state equation representation of transformers for simulation of electromagnetic transients," *IEEE Trans. Power Del.*, vol. 13, pp. 834-842, July 1998.

[50] D. Saraswat, R. Achar, and M. Nakhla, "A fast algorithm and practical considerations for passive macromodeling of measured/simulated data," in *Proc. IEEE 11th Topical Meeting on EPEP*, Oct. 2002, pp. 297-300.

[51] N. Stevens, D. Deschrijver, and T. Dhaene, "Fast automatic order estimation of rational macromodels for signal integrity analysis," in *Proc. 11th IEEE Workshop on Signal Propag. on Interconnects*, May 2007, pp. 89-92.

[52] D. Slepian, "On bandwidth," *Proc. IEEE*, vol. 64, pp. 292-300, March 1976.

[53] D. Slepian, "Some comments on Fourier analysis, uncertainty and modeling," *SIAM Rev.*, vol. 25, pp. 379-393, July 1983.

[54] M. Yuan, A. De, T. Sarkar, J. Koh, and B. Jung, "Conditions for generation of stable and accurate hybrid TD-FD MoM solutions," *IEEE Trans. Microw. Theory Tech.*, vol. 54, pp. 2552-2563, June 2006.

[55] T. K. Sarkar, J. Koh, W. Lee, and M. Salazar-Palma, "Analysis of electromagnetic systems irradiated by ultra-short ultra-wideband pulse," *Meas. Sci. Tech.*, vol. 12, pp. 1757-1768, Nov. 2001.

[56] M. Celik and A. C. Cangellaris, "Simulation of dispersive multiconductor transmission lines by Padé via Lanczos process," *IEEE Trans. Microw. Theory Tech.*, vol. 44, pp. 2525-2535, Dec. 1996.

[57] R. Wang and J. Jin, "A symmetric electromagnetic-circuit simulator based on the extended time-domain finite element method," *IEEE Trans. Microw. Theory Tech.*, vol. 56, pp. 2875-2883, Dec. 2008.

[58] S. Moon and A. C. Cangellaris, "Passivity enforcement via quadratic programming for element-by-element rational function approximation of passive

network matrices," in *Proc. IEEE 17th Topical Meeting on EPEP*, Oct. 2008, pp. 203-206.

[59] D. Saraswat, R. Achar and M. Nakhla, "Restoration of passivity in S-parameter data of microwave measurements," in *IEEE MTT-S Int. Microw. Symp. Dig.*, June 2005, pp. 1131-1134.

[60] S. Grivet-Talocia, "Passivity enforcement via perturbation of Hamiltonian matrices," *IEEE Trans. Circuits Syst. I, Fundam. Theory Appl.*, vol. 51, pp. 1755-1769, Sep. 2004.

[61] D. Saraswat, R. Achar, and M. Nakhla, "On passivity check and compensation of macromodels from tabulated data," in *Proc. 7th IEEE Workshop Signal Propag. Interconnects*, May 2003, pp. 25-28.

[62] R. Gao, "Black box modeling of passive systems by rational function approximation," Ph.D. dissertation, University of Illinois at Urbana-Champaign, 2005.

[63] M. E. Van Valkenburg, *Introduction to Modern Network Synthesis*. New York, NY: Wiley, 1960.

[64] M. Celik, L. Pileggi, and A. Odabasioglu, *IC Interconnect Analysis*. Boston MA: Kluwer Academic Publishers, 2002.

[65] Y. Liu, L. T. Pileggi, and A. J. Strowas, "ftd: Frequency to time domain conversion for reduced-order interconnect simulation," *IEEE Trans. Circuits Syst. I, Fundam. Theory Appl.*, vol. 48, pp. 500-506, April 2001.

[66] M. J. Choi, "Efficient broadband electromagnetic modeling of the power distribution network in high-speed, mixed-signal integrated circuits," Ph.D. dissertation, University of Illinois at Urbana-Champaign, 2003.

[67] R. Neumayer, A. Stelzer, F. Haslinger, and R. Weigel, "On the synthesis of equivalent-circuit models for multiports characterized by frequency-dependent parameters," *IEEE Trans. Microw. Theory Tech.*, vol. 50, pp. 2789-2796, Dec. 2002.

[68] K. M. Coperich, J. Morsey, V. I. Okhmatovski, A. C. Cangellaris, and A. E. Ruehli, "Systematic development of transmission-line models for interconnects with frequency-dependent losses," *IEEE Trans. Microw. Theory Tech.*, vol. 49, pp. 1677-1685, Oct. 2001.

# APPENDIX A
# INVERSE FAST FOURIER TRANSFORM

The procedure of IFFT to ensure that the time-domain responses will be real is presented as follows.

1. The frequency data are given. The number of samples is $M_f$, start frequency is $f_{start}$, and stop frequency is $f_{stop}$.
2. If the frequency step $\Delta f$ is not constant, the sampling is made uniform using interpolation and extrapolation.
3. When the frequency-domain data are arranged as

| | | | |
|---|---|---|---|
| $F_1(f=f_1)$ | $F_2(f=f_2)$ | $F_3(f=f_3)$ | $F_4(f=f_4)$ |

where $\Delta f = f_1$ and $f_{stop} = f_4$, we need to pad the data set after the given frequency data array in its complex conjugate mirror image to ensure the time-domain response to be real. There are two ways of padding, depending on whether the number of the input data for IFFT is odd or even. Here is the operation of FFT in MATLAB:

```
>> a=fft([1 2 3 4 8 9]')
a =
 27.0000
 -3.0000 +10.3923i
 -6.0000 + 1.7321i
 -3.0000
 -6.0000 - 1.7321i
 -3.0000 -10.3923i .
```

When the number of the input *N* is even, the first value and the middle value of the fft output are real, as shown below:

```
>> a=fft([1 2 3 4 8]')
a =
 18.0000
 -1.5729 + 6.2941i
 -4.9271 + 2.5757i
 -4.9271 - 2.5757i
 -1.5729 - 6.2941i.
```

Unlike the case when N is even, only the first value of the output is real when *N* is odd. Hence, the frequency data should be carefully arranged for the input of IFFT as

| | | | | | | | |
|---|---|---|---|---|---|---|---|
| $F_0(f=f_0)$ | $F_1$ | $F_2$ | $F_3$ | $Re(F_4)$ | $F_3^*$ | $F_2^*$ | $F_1^*$ |

or

| | | | | | | | | |
|---|---|---|---|---|---|---|---|---|
| $F_0(f=f_0)$ | $F_1$ | $F_2$ | $F_3$ | $F_4$ | $F_4^*$ | $F_3^*$ | $F_2^*$ | $F_1^*$ |

In both cases, $F_0$ should be real.

4. The modified frequency data array is put into the IFFT process, and the impulse function is generated as an output.

Then a Gaussian pulse whose sampling rate is $1/(2\ f_{stop})$ is convoluted with the impulse function, and the impulse response is generated. Then the transport delay is measured between input peak and output peak.

# AUTHOR'S BIOGRAPHY

Se-Jung Moon was born in Seoul, Korea. She received her B.S. degree in electrical engineering and her M.S. in physics from Seoul National University in 1999 and 2001, respectively. In 2003, she joined the Center for Computational Electromagnetics at the University of Illinois at Urbana-Champaign in pursuit of her Ph.D. degree under the supervision of Professor Andreas Cangellaris. She is a member of GRC (Global Research Collaboration). Her research interests include development of efficient and accurate modeling methods for high-speed interconnects and analysis of EM effects involved in signal integrity.